Design and Enhancement of Fiber Optic Evanescent Wave LSPR-Based Biosensor Fabricated via Self-Assembled Silver Nanoparticles for Salivary Cortisol Detection

by

Omar A. H. Awad

A thesis
presented to the University of Waterloo
in fulfillment of the
thesis requirement for the degree of
Doctor of Philosophy
in
Mechanical and Mechatronics Engineering

Waterloo, Ontario, Canada, 2024

© Omar A. H. Awad 2024

Examining Committee Membership

The following served on the Examining Committee for this thesis. The decision of the Examining Committee is by majority vote.

External Examiner	Mohammad E. Khosroshahi Professor
Supervisor(s)	Patricia Nieva Professor
Internal Member	Sushanta Mitra Professor
Internal Member	Kevin Musselman Associate Professor
Internal-external Member	Zoya Leonenko Professor

Author's Declaration

I hereby declare that I am the sole author of this thesis. This is a true copy of the thesis, including any required final revisions, as accepted by my examiners.

I understand that my thesis may be made electronically available to the public.

Abstract

There are currently no point-of-care means accessible for non-invasive, real-time monitoring of cortisol levels. All available home test kits for cortisol testing require the patients to send out their samples to laboratories after collection and wait days or weeks in some instances to receive their results. Cortisol is an important stress biomarker that is at the core of many mental and physical disorders, and early detection of abnormal cortisol levels is crucial for their prevention. This work aims to fabricate a highly accessible, inexpensive, sensitive, and non-invasive point-of-care salivary cortisol sensor, utilizing a fiber optic evanescent wave sensor (FOEW) enhanced by the effect of localized surface plasmon resonance (LSPR). The development of this sensor presents an advanced analysis on the parameters affecting the performance of FOEW LSPR sensors fabricated via self-assembly of silver spherical nanoparticles. The analysis is based on a combination of numerical and analytical models validated with experiments. A numerical model is first used to solve Mie's theory to study the absorption of light interacting with nanoparticles due to LSPR using ANSYS LUMERICAL. Nanoparticles ranging from 10 to 100 nm diameter were considered due to their LSPR properties at this range. Simulations show that silver spherical nanoparticles with 30 nm diameter exhibit the highest absorption efficiency, and that the magnitude of absorption correlates positively with the number of nanoparticles. An analytical model is then used to describe the adsorption kinetics and formation of a nanoparticle monolayer on the longitudinal surface of the fiber's core based on diffusion transport process. The analytical adsorption model suggested that smaller nanoparticles result in higher final surface density. The

performance of the FOEW LSPR sensor signal was modeled utilizing smaller nanoparticle sizes (10 nm, 20 nm, and 30 nm) using COMSOL MULTIPHYSICS. Results show that 30 nm-based FOEW LSPR have the highest absorption signal and refractive index sensitivity. The electromagnetic field decay length was modeled in ANSYS LUMERICAL as well, and the results showed that 30 nm nanoparticles have electromagnetic field decay length that engulfs the conjugated ligand and analyte, which is optimum for cortisol biosensing. The sensor response was also modeled by integrating the ligand-analyte interaction model with the FOEW LSPR sensor model. The modeling results agree with experiments performed on FOEW LSPR sensors fabricated using 30 nm diameter nanoparticles, which show enhanced LSPR signal and refractive index sensitivity compared to results obtained using 20 nm, and 10 nm diameter nanoparticles. Characterizations performed on the prepared fiber sensors using Atomic Force Microscopy (AFM) and Scanning Electron Microscopy (SEM) show significantly higher nanoparticle coverage for sensors fabricated using smaller nanoparticles, which validated the modeling results. A working cortisol biosensor was fabricated using the 30 nm based FOEW LSPR sensor by functionalizing the nanoparticles surface with Cysteamine Hydrochloride, allowing for the bioconjugation of anti-cortisol IgG antibodies. This sensor was reproducible with a sensitivity of 0.0128 nm/nM, a limit of detection of 0.1125 pM and a limit of quantification of 0.3712 pM, covering the range cortisol found in saliva. The findings reported in this Thesis therefore present a promising technology for the fabrication of highly sensitive and cost-effective point-of-care cortisol monitoring devices. Which can be widely accessible and can help with the early detection of abnormal cortisol levels, allowing for the prevention of many mental and physical disorders.

Acknowledgements

First and foremost, I wish to express my heartfelt gratitude to my supervisor, Professor Patricia Nieva, for granting me the opportunity to work on this thesis. Thank you for your support and guidance throughout this journey.

I extend my appreciation to my colleagues Abdulrahman Ghannoum, and Rishard Rameez. Their contribution, particularly in brainstorming the research idea, was crucial. Abdulrahman's assistance during the early phase of my research was invaluable. I feel privileged to have conducted my research among the members of the Sensors and Integrated Microsystems Laboratory (SIMSLAB) family.

I thank the members of my committee, Professor Sushanta Mitra, Professor Zoya Leonenko, and Professor Kyle Daun, for their feedback on my work during and after my comprehensive exam. I also deeply thank Professor Kevin Musselman for agreeing to be on my examining committee, and Professor Mohammad Khosroshahi for participating in my defense as the external examiner. Thank you for accommodating me.

My deepest thanks go to God, my parents, my sister, and my wife. To my parents, I owe everything I am, and everything I will be to you. To my sister, thank you for listening to me complain all these years, and to my beloved wife, thank you for your unlimited support, understanding, and encouragement during my PhD.

Dedication

In the name of Allah, the Most Gracious, the Most Merciful. All praise and thanks are due to Allah, who has blessed me abundantly despite my many shortcomings and guided me through every step of this journey. I vow to use the knowledge and skills I have gained for the betterment of humanity, in accordance with His will.

To my younger self, whose dream of pursuing a PhD inspired and propelled me through this challenging and transformative journey. Your determination and vision have been my guiding light. We are here now. Thank you for being persistent.

To my family, especially my parents who sacrificed everything for their children, and have always stood by my side and prayed for me. Without you, I would never be here.

To my beloved wife, whose endless support and understanding have been my anchor. Your love and patience have been my greatest source of comfort and motivation.

And to my two-year-old son, who missed me during the countless hours I spent on my research. I promise to make up for the lost time and create many cherished memories together. I hope one day you will be half as proud of me as I am of you.

Table of Contents

Examining Committee Membership ii

Author's Declaration iii

Abstract iv

Acknowledgements vi

Dedication vii

List of Figures xi

List of Tables xv

List of Abbreviations xvi

List of Symbols xvii

Chapter 1 Introduction: Motivation, Literature, and Objectives 1

1.1 Motivation for a salivary cortisol biosensor 1

1.2 Biosensors: Architecture and Technology 4

1.2.1 Biosensing Detection Approach: Labeled vs Label-free Sensors 5

1.3 Localized Surface Plasmon Resonance Sensing 7

1.4 Fiber Optic Evanescent Wave Sensing 10

1.5 FOEW LSPR Biosensor Fabrication and Sensing 12

1.5.1 Nanoparticle Immobilization Techniques 14

1.5.2 Ligand – Nanoparticle Conjugation Techniques 16

1.6 Status of FOEW LSPR/SPR based Biosensors 18

1.7 Objectives of this Thesis 21

Chapter 2 Modeling the Parameters Affecting Sensor Signal and Performance 22

2.1 Introduction 22

2.2 Modeling nanoparticle absorption and adsorption kinetics 22

2.2.1 Nanoparticle absorption – numerical model 25
2.2.2 Nanoparticle adsorption kinetics – analytical model 30
2.2.3 Optical fiber response – derived analytical model 33
2.2.4 Combined models result 36
2.3 Modeling FOEW LSPR refractive index sensor 38
2.3.1 Modeling the sensing region optical properties 39
2.3.2 Modeling the silver nanoparticle optical properties 41
2.3.3 Modeling FOEW LSPR response and sensitivity 43
2.3.4 Sensor performance results 48
2.4 Modeling the Electromagnetic Field Decay Length 55
2.5 Modeling the Analyte-Ligand Reaction Kinetics and final sensor response 60
2.5.1 Cortisol-Antibody reaction kinetics model 61
2.5.2 Sensor response model 65
Chapter 3 Model Verification: Experimental Procedures 68
3.1 Materials 68
3.2 FOEW LSPR Sensor Fabrication 68
3.2.1 Sensing region creation 69
3.2.2 Sensing region functionalization and salinization 71
3.2.3 Coating apparatus 73
3.3 The effect of nanoparticle size on adsorption kinetics and absorption signal 74
3.3.1 AFM Characterization 77
3.3.2 UV–VIS Characterization 78
3.4 The effect of nanoparticle size on FOEW LSPR refractive index sensitivity 80
3.4.1 Refractive index sensitivity testing 82

3.4.2 SEM Characterization 84
3.5 Sensor response model update based on experimental results 86
Chapter 4 LSPR FOEW Cortisol Biosensor Fabrication and Testing 87
4.1 Materials 87
4.2 Biosensor fabrication 87
4.2.1 MUA concentration optimization 89
4.3 Experimental Setup 92
4.3.1 Surface Activation and Antibody Conjugation Procedure 94
4.3.2 Cortisol Testing and Results 98
4.3.3 Potential reasons behind the unsuccessful experiment 99
4.4 Cysteamine Functionalization 101
4.4.1 Surface functionalization and Antibody Conjugation Procedure 102
4.4.2 Cortisol Testing and Results 104
4.4.3 Model update and comparison 106
Chapter 5 Contributions, Future work, and Conclusions 108
5.1 Thesis Contributions 108
5.1.1 Manuscripts generated from this work 109
5.2 Future work 110
5.3 Conclusions 112
References 115
Appendix A 128
Appendix B 130

List of Figures

Figure 1 – General Cortisol Circadian Rhythm, graph recreated with data from [6] 1

Figure 2 – Illustration showing typical architecture of Biosensors – Created with BioRender.com 5

Figure 3 – Illustration showing the difference between Label-free biosensing (a), and Label-based biosensing (b) – Created with BioRender.com 5

Figure 4 – Illustration of incoming light wave interacting with metallic nanoparticles and exciting localized surface plasmon resonance – Created with BioRender.com 8

Figure 5 – Illustration showing SPR biosensing (left) and LSPR biosensing (right) – Created with BioRender.com 8

Figure 6 – Illustration of Evanescent field in an optical fiber – Created with BioRender.com 10

Figure 7 – Illustration showing the fabrication and sensing concepts behind FOEW LSPR biosensors. a) LSPR absorption signal due to metallic nanoparticle adsorption on the sensing region. b) LSPR absorption signal wavelength shift due to ligand conjugation. c) LSPR absorption signal shift due to ligand-analyte interaction – Created with BioRender.com 13

Figure 8 – physical interactions between antibodies and nanoparticles adopted from [66] – Created with BioRender.com 17

Figure 9 – (a) The construction of the model in ANSYS LUMERICAL (left) – (b) Extinction, Scattering, and Absorption cross section for an 80 nm silver nanoparticle in a 1.34 refractive index medium (right)-(cubic spline fit used to cover all simulation points) 26

Figure 10 – (a) Maximum LSPR cross section peak for each silver nanoparticle size ranging from 10 nm to 100 nm at their respective wavelength (left) – (b) Maximum LSPR efficiency peak for silver nanoparticles with size ranging from 10 nm to 100 nm, in steps of 10nm, at their respective wavelength (right). (cubic spline fit used to cover all simulation points) 27

Figure 11 – Relation between LSPR absorption peak and number of nanoparticles 29

Figure 12 – (a) Comparison between the surface density of 30 nm and 80 nm particles after 24 hours of adsorption (left) – (b) Effect of size on surface density after 24 hours of adsorption (right) 32

Figure 13 – FOEW LSPR absorption obtained from the combined model for (a) 30 nm nanoparticles (left) – (b) 80 nm nanoparticles (right) (cubic spline fit used to cover all simulation points). 36

Figure 14 – comparison between refractive index of coreless fiber provided by the manufacturer against the results from the Sellmeier equation 40

Figure 15 – (a) Silver dielectric constant (left) – (b) Silver refractive index (right) 42

Figure 16 – FOEW LSPR Sensor model construction used in COMSOL simulations 43

Figure 17 – FOEW LSPR Sensor model construction used in COMSOL showing the mesh size 44

Figure 18 – (a) Confinement loss at 360 nm vs number of modes (left) – (b) Wavelength (right) 46

Figure 19 – (a) Fundamental mode (top) – (b) Higher order mode (bottom) – Wavelength 360 μm .. 47

Figure 20 – Modelling results for varying refractive indices – 30 Modes – 180 particles – (a) 30 nm (top) – (b) 20 nm (middle) – (c) 10 nm (bottom) 51

Figure 21 – Modelling results for varying refractive indices – 30 Modes – (a) 240 particles 20 nm (top) – (b) 360 particles 10 nm (bottom) 53

Figure 22 – a) Small electromagnetic field - b) Optimum electromagnetic field - c) large electromagnetic field – Created with BioRender.com 56

Figure 23 – ANSYS LUMERICAL model construction for water shell method 57

Figure 24 – Water shell thickness vs LSPR peak for 10 nm, 20 nm, and 30 nm silver nanoparticles . 58

Figure 25 – Dimensions of IgG antibody from literature – Created with BioRender.com 59

Figure 26 – Microchannel model construction in COMSOL – analyte-ligand interaction model 62

Figure 27 – COMSOL results for the cortisol – antibody interaction kinetics 64

Figure 28 – Final analyte-ligand model results showing: (a) antibody occupied sites (left) – (b) fraction of occupied sites (right) – vs cortisol concentration 65

Figure 29 – Final sensor response model based on COMSOL modelling results combined with de Feijter's equation 66

Figure 30 – (a) Cross sections of standard fiber (left) – (b) coreless fiber (right) – Created with BioRender.com 70

Figure 31 – Optical fiber fusion splicer upon a successful splice 70

Figure 32 – Hydroxylation process using UVO treatment on a glass substrate – Created with BioRender.com 71

Figure 33 – Salinization of a glass substrate – Created with BioRender.com 72

Figure 34 – Coating apparatus made for APTES functionalization 74

Figure 35 – Absorption signal vs: (a) wavelength (left) – (b) time (right) 75

Figure 36 – Comparison of LSPR signals between 30 nm and 80 nm nanoparticle sensors after 15 hours of adsorption 76

Figure 37 – AFM images and height distribution for fiber surface with: (a) 30 nm (top) – (b) 80 nm (bottom) – after 15 hours of incubation 77

Figure 38 – Nanoparticle colloidal solution UV-VIS LSPR signal vs fiber optic evanescent wave LSPR signal in colloidal solution: (a) 30 nm (left) – (b) 80 nm (right) 79

Figure 39 – (a) Absorption signal vs wavelength after adsorption process is complete (left) – (b) Absorption signal LSPR peak vs time for 10 nm, 20 nm, and 30 nm silver nanoparticle sensors (right) 80

Figure 40 – Refractive index sensitivity testing results – (a) LSPR vs Size (left) – (b) LSPR vs Refractive Index (right) 83

Figure 41 – SEM images and count for fiber surface with: (a) 10 nm (top) – (b) 20 nm (middle) – 30 nm (bottom) nanoparticles 85

Figure 42 – Updated sensor response model based on the experimental sensitivity of 30 nm based FOEW LSPR sensor using 125 μm coreless fiber as the sensing region 86

Figure 43 – Schematic showing the FOEW LSPR Cortisol biosensor fabrication process and testing based on MUA pre-functionalization – Created with BioRender.com 90

Figure 44 – (a) Absorption signal vs wavelength after adsorption process is complete for different MUA concentrations (left) – (b) Change of LSPR peak absorption magnitude over time for different MUA concentrations (right) – after 2 hours of incubation time 91

Figure 45 – SEM image of 30 nm based FOEW LSPR sensor: (a) without MUA pre-functionalization (left) – (b) with 0.5 mM MUA pre-functionalization for 2 hours (right) 92

Figure 46 – (a) Experimental setup schematic (left) – (b) Actual experimental setup (right) – Created with BioRender.com 93

Figure 47 – (a) Aluminum mold used to create the PDMS micro channel (left) – (b) The final sealed channel with the FOEW LSPR sensor enclosed 94

Figure 48 – LSPR peak shift due to EDC/NHS activation, antibody conjugation, and BSA blocking processes 95

Figure 49 – (a) Full spectrum showing LSPR peak wavelength shift after each process (left) – (b) Zoomed in spectrum focusing on the peaks only (right) 96

Figure 50 – (a) antibody concentration vs LSPR peak wavelength shift bar graph (left) – (b) logarithmic graph (right) 97

Figure 51 – Simple representation of the chemical structure of IgG antibodies – Created with BioRender.com 100

Figure 52 – Schematic showing the FOEW LSPR Cortisol biosensor fabrication process and testing based on Cysteamine functionalization – Created with BioRender.com 101

Figure 53 – (a) LSPR absorption peak during the Cysteamine functionalization process (left) – (b) LSPR wavelength during the Cysteamine functionalization process (right) 103

Figure 54 – LSPR peak shift due to pre-activated antibody conjugation, and BSA blocking processes 104

Figure 55 – (a) Sensor response due to different concentrations of cortisol (left) – (b) Average response of 5 sensors due to different cortisol concentrations (right) 105

Figure 56 – Experimental results compared to updated sensor response model based on experimental refractive index sensitivity 107

List of Tables

Table 1 – Current literature on FOEW LSPR/SPR sensors 18

Table 2 – Sellmeier equation variables for pure silica [111] 40

Table 3 – Values of the silver nanoparticle variables used in the Drude-Lorentz model [113] 41

Table 4 – Summary of FOEW LSPR model results 54

Table 5 – Non-linear least squares regression results 59

Table 6 – Parameters used in the cortisol-antibody reaction kinetics model 63

Table 7 – de Feijter's equation parameters 66

Table 8 – Refractive index values of a dilution series of glycerol and DI water 82

Table 9 – Comparison between theoretical and experimental surface densities 84

Table 10 – List of MUA concentrations and incubation times used in SPR/LSPR sensors 89

Table 11 – COMSOL MULTIPHYSICS FOEW LSPR modeling parameters 128

Table 12 – COMSOL MULTIPHYSICS FOEW LSPR modeling variables 129

List of Abbreviations

AFM	Atomic Force Microscopy
APDMS	AminoPropylDiethoxyMethylSilane
APTES	(3-AminoPropyl)TriEthoxySilane
ATR	Attenuated Total Reflection
BSA	Bovine Serum Albumin
EDC	(1-ethyl-3-(3-dimethylaminopropyl)carbodiimide hydrochloride)
ELISA	Enzyme-Linked Immunosorbent Assays
FOEW	Fiber Optics Evanescent Wave
HPA-axis	Hypothalamic–Pituitary–Adrenal axis
LC-MS/MS	Liquid Chromatography-Tandem Mass Spectrometry
LSPR	Localized Surface Plasmon Resonance
MPTES	3-Mercaptopropyl Triethoxysilane
MUA	11-Mercaptoundecanoic acid
NHS	(N-hydroxy succinimide)
PAH	Poly(allylamine hydrochloride)
PBS	Phosphate-Buffered Saline
PEI	Polyethyleneimine
SEM	Scanning Electron Microscopy
SPR	Surface Plasmon Resonance
TIR	Total Internal Reflection
UV-VIS	Ultra Violet – Visible light Spectrum

List of Symbols

I_{f}	Final intensity of the light due to the interaction of the evanescent wave
I_0	Initial light intensity
r	ratio of the optical power available in the evanescent wave to the total power
C	Constant
L_{int}	Optical fiber interaction length or sensing region length
C_{ext}	Extinction cross section for spherical nanoparticle
N	Electron density of metallic nanospheres
r_{np}	Nanoparticle radius
ε_m	Dielectric constant of medium
λ	Wavelength of light
ε_i	Imaginary part of nanoparticle's material dielectric constant
ε_r	Real part of nanoparticle's material dielectric constant
χ	Shape factor (depends on the shape of the nanoparticle)
P	Polarizability
ε_0	Permittivity of free space
ε_{np}	Nanoparticle's material dielectric constant
ω_p	Plasma frequency
ω	Angular frequency of the electromagnetic radiation
γ	The damping frequency
ω_{LSPR}	LSPR frequency
$\mathrm{N_s}$	Nanoparticle surface density

D	Diffusion coefficient
t	Immersion time
c_w	Nanoparticle weight concentration in PPM
C_b	Nanoparticle bulk number concentration
Q_{abs}	Absorption efficiency
$P(z)$	Function for power transmitted through an uncladded fiber
P_0	Initial power transmitted through an uncladded fiber
τ	Evanescent field absorbing coefficient
z	Length of uncladded fiber
V	Normalized frequency
r_f	Fiber radius
NA	Numerical aperture
$n(\lambda)$	Refractive index of the glass as a function of transmitted wavelength
CL	Confinement loss
n_{eff}	Effective refractive index
M	Number of modes inside a fiber
S	Sensitivity of the sensor
LOD	Limit of detection
LOQ	Limit of quantification
$\Delta\lambda_{LSPR}$	LSPR wavelength shift
m_{np}	Refractive index sensitivity of a nanoparticle
n_a	Refractive index due to analyte binding

d	Thickness of analyte layer
l_d	Electromagnetic field decay length
K_d	Dissociation constant
k_{on}	Association rate
k_{off}	Dissociation rate
θ	Fraction of occupied site
R	Biosensor response based on fraction of occupied site
R_{max}	Maximum biosensor response when all available sites are occupied
n_m	Refractive index of medium
n_i	Refractive index increment of analyte
γ_{ac}	Binding sites
M_a	Molecular mass of analyte

Chapter 1
Introduction: Motivation, Literature, and Objectives

1.1 Motivation for a salivary cortisol biosensor

Cortisol is a vital hormone for the physical and mental wellbeing. It is responsible for regulating body functions like metabolism, blood pressure, and blood sugar, while also responding to stress. Challenging physical or psychological situations triggers stress, affecting cortisol levels [1]. Abnormal cortisol levels cause various mental disorders that contribute to many diseases, and have been identified as a reason for depression [2]. As stated in [3], "About 50% percent of patients with newly diagnosed depression have been observed to have excessive cortisol secretion".

Ideally, cortisol levels should be highest in the morning, gradually decreasing over the day, reaching their lowest point at night before sleep. This behavior, represented in Figure 1, is known as the cortisol circadian rhythm, which is mainly found in blood serum [4] and is controlled by the hypothalamic–pituitary–adrenal axis (HPA-axis) [5].

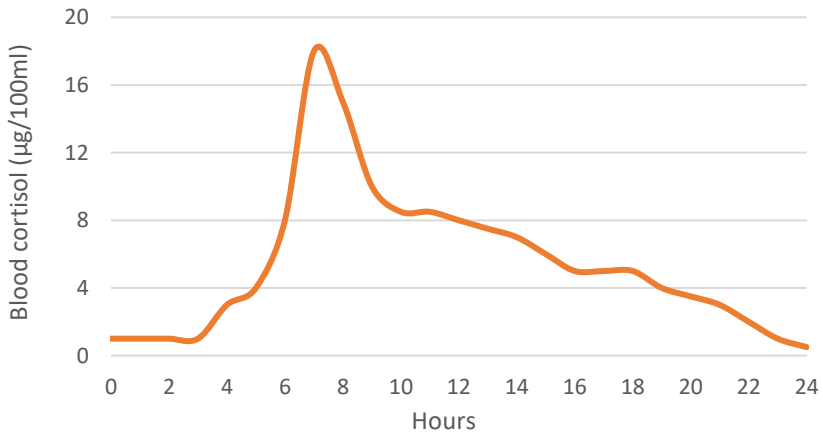


Figure 1 – General Cortisol Circadian Rhythm, graph recreated with data from [6]

Cortisol can be found in other bodily fluids such as sweat, urine, and saliva, albeit with lower concentrations [7]. Consequently, blood serum cortisol measurement is considered the most common clinical cortisol determination method [8]. Due to the circadian rhythm of cortisol in the body, patients are required to perform the test multiple times a day [9]. This test requires the draw of blood, which is invasive and unpleasant, and thus further contribute to the patient's mental or physical distress, which ultimately could affect the cortisol levels during testing [10].

Cortisol can also be measured in urine, sweat, and saliva [7]. Urinary cortisol is usually measured over a 24-hour period, and the results reflect the average total cortisol production. This is useful in detecting abnormalities, such as (Addison's Disease) or (Cushing's Syndrome), where the average cortisol production is either extremely low or extremely high [7]. Nonetheless, most people suffering from irregular cortisol levels due to stress, depression, or anxiety do not fall into that category. Moreover, the results of this test might be misleading. Since the test returns the total average production of cortisol over a 24 hour period, an average reading for an ill individual, whose circadian rhythm is opposite to that of a healthy one, will be within normal range [11]. As for salivary cortisol, research show it mimics the circadian rhythm found in blood serum [4,12]. Additionally, cortisol in saliva is deemed a more reliable alternative to blood serum cortisol in testing, as it reflects the free unbound cortisol, which is a better indicator for diagnosing health issues [13]. Many studies proved that salivary cortisol tests can provide more than 90% accurate results in diagnosing certain diseases [14].

Currently, "Liquid Chromatography-Tandem Mass Spectrometry (LC-MS/MS) is the method of choice for measuring salivary cortisol in laboratories. However, its use is limited by

the lack of a single, validated reference range and poorly developed assays" [7]. Additionally, LC-MS/MS is an expensive machine to build and operate. Other available clinical cortisol detection techniques include enzyme-linked immunosorbent assays (ELISA) [15], flow immunoassays [16], electrochemical immunosensors [17], chemiresistors [18], radioimmunoassay [19], and Raman spectroscopy [20], which measure cortisol levels within the physiological range, but are limited by their low sensitivity and specificity, complexity, cost, and long detection time [21]. It should be noted the weak Raman signal can be enhanced significantly using Surface Enhanced Raman Spectroscopy (SERS) [22].

Furthermore, there are currently no point-of-care monitoring options for cortisol. The current home test kits for cortisol testing require patients to collect the sample and send it to laboratories for testing. The overall process takes days, and in some instances weeks, before the patients can have their results. This defeats the purpose of monitoring the cortisol levels for stress, depression, and anxiety related cases, as the results should be instantaneous due to the circadian rhythm nature of cortisol.

As mentioned in a recent study [23], "There is a great demand for a continuous real-time cortisol sensor that is yet to be developed". The author also states that "A cortisol monitoring device will be essential for personified pharmacological correction of the HPA-axis toward normal cortisol levels through a 24-h cycle" [23]. Therefore, it is crucial to develop a widely accessible, highly sensitive and specific cortisol monitoring device that can provide real-time detection of cortisol. Considering that saliva sample collection is a non-invasive and convenient process that can be done at the patients' will multiple times a day, it is considered

the most preferred way for monitoring cortisol levels. Saliva samples are also easily handled and stored [24].

For these reasons, this thesis aims to develop a point-of-care cortisol monitoring device that is highly sensitive, by fabricating a salivary cortisol sensor based on fiber optics evanescent wave (FOEW), combined with the effect of localized surface plasmon resonance (LSPR) of silver nanoparticles. The coming sections will explain why this type of sensor and sensing mechanism were chosen for this work. Modeling of the sensor concept is followed by experiments to verify, validate, and characterize the final sensor. This thesis will highlight the parameters that affect the sensor's final sensitivity, during the fabrication stage and the testing stage, as well as including the optimization of the fabrication process for a fast and low-cost fabrication.

1.2 Biosensors: Architecture and Technology

Biosensors are devices designed to detect or quantify the presence of a specific biomarker in a sample. According to the National Cancer Institute (NCI), a biomarker is defined as "A biological molecule found in blood, other body fluids, or tissues that is a sign of a normal or abnormal process, or of a condition or disease. A biomarker may be used to see how well the body responds to a treatment for a disease or condition." [25]. Figure 2 illustrates the typical architecture of biosensors.

As shown in the figure, biosensors generally comprise of three rudimentary components: the sensing element, which consists of the receptor that recognizes and interacts with the biomarker under study, and the bio-interface which responds to this interaction; the

signal transducer, which converts the bio-recognition interaction response into electrical, mechanical, or optical signals that can be detected; and the output system, which processes the signals generated by the transducer and provides the final results for analysis or interpretation [26]. The performance of a biosensor is influenced by all three components [26,27].

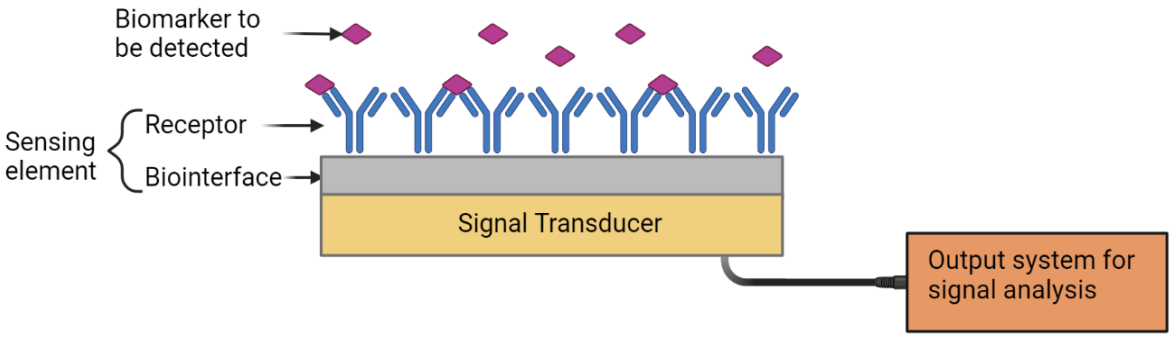


Figure 2 – Illustration showing typical architecture of Biosensors – Created with BioRender.com

1.2.1 Biosensing Detection Approach: Labeled vs Label-free Sensors

The detection approaches in biosensors can be classified into two prominent methods: label-based and label-free biosensing, shown in Figure 3, each offering distinct advantages and considerations [26,27].

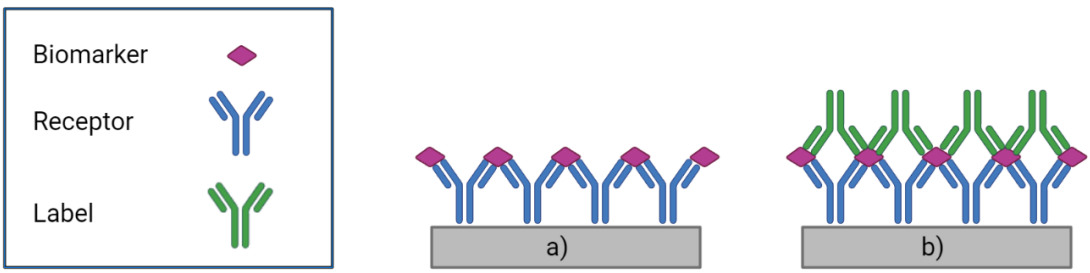


Figure 3 – Illustration showing the difference between Label-free biosensing (a), and Label-based biosensing (b) – Created with BioRender.com

In label-based biosensing, labels such as fluorescent markers or radioactive molecules like biotin, are attached to the biomarker to facilitate detection. Due to the inherent challenges

in detecting some organic biomarkers solely based on their fundamental physical characteristics, the incorporation of labels becomes necessary. Upon interaction between the biomarkers and the receptors, the transducer measures the amount of labels, which is a simple way of providing a quantitative measure of the bound target molecules [27]. The sensitivity of the sensor can also be significantly enhanced by designing a transducer mechanism that is very sensitive to the label molecule. As a results, label-based biosensing methods, such as ELISA and western blot, are used in most standard biological sensing applications and are considered the most common biosensing detection techniques [26,28].

Nonetheless, labeled techniques in biosensing present several notable limitations that should be considered. These drawbacks encompass challenges related to the stability, safety, and cost of label molecules, as well as the complexity imposed by labeling that require multiple processing steps, reagents, and equipment. Additionally, the modification of the analyte during the labeling process, and the variability in labeling reaction yields further contribute to the limitations of labeled techniques [29]. In the context of fluorescent techniques for instance, photobleaching degrades the excitation efficiency of the fluorophores over repeated exposure to light, which limits the ability of the technique to provide quantitative measurements and requires the assay to be read after the binding occurs and only once, causing all information about the kinetics of the interaction to be lost [30].

Due to the above limitations, it is evident that label-free approaches, such as LSPR and SPR biosensing, provide a promising alternative by addressing the limitations associated with labeled techniques, while enabling a more comprehensive and dynamic analysis of biomolecular interactions. Label-free biosensing detects the target molecules without the need

for specific labels. These techniques rely on the detection of changes in physical, electrical, optical, or chemical properties that occur when the target molecule binds to the biosensor surface, providing information on the binding kinetics, and allowing for real-time and fast monitoring of biomarker levels in the sample [27,29,30].

Although label-based biosensors can be more sensitive, label-free biosensors cost less to fabricate, require fewer steps with less complexity, and fewer reagents. Combined with the ability to provide real-time information, label-free biosensors are best suited for portable devices designed for point-of-care applications [28]. For these reasons, the work presented in this thesis focuses on the development of a label-free cortisol biosensor. The difference between LSPR and SPR biosensing, along with the reasoning behind choosing LSPR specifically as a sensing mechanism for this work, will be explained in detail in the next section.

1.3 Localized Surface Plasmon Resonance Sensing

Localized Surface Plasmon Resonance is an optical phenomenon that occurs when light interacts with the conduction band of a noble metal nanoparticle that has a cross section smaller than the wavelength of light [31]. As shown in Figure 4, this causes the valance electrons to oscillate at resonance, resulting in an absorption within the ultraviolet-visible (UV-Vis) spectrum. The plasmon resonance frequency is a function of the nanoparticle material, size, shape, as well as the dielectric constant of the medium surrounding the nanoparticle [32] and its calculation will be explained in detail in Chapter 2. Surface Plasmon Resonance (SPR) is

the same phenomenon but occurs when the metal is deposited as a continuous thin film along a dielectric substrate [31].

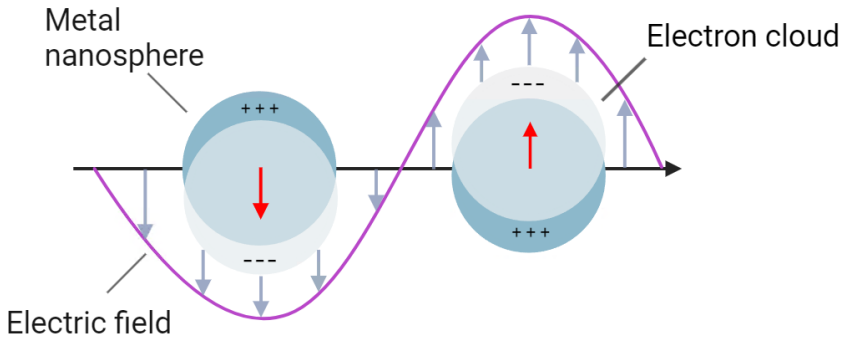


Figure 4 – Illustration of incoming light wave interacting with metallic nanoparticles and exciting localized surface plasmon resonance – Created with BioRender.com

In biosensing applications, the ligand is conjugated on the nanoparticle, as shown in Figure 5, and the interaction between the ligand and analyte in the solution surrounding the nanoparticle affects local refractive index around the nanoparticle, thus causing a change in LSPR/SPR frequency.

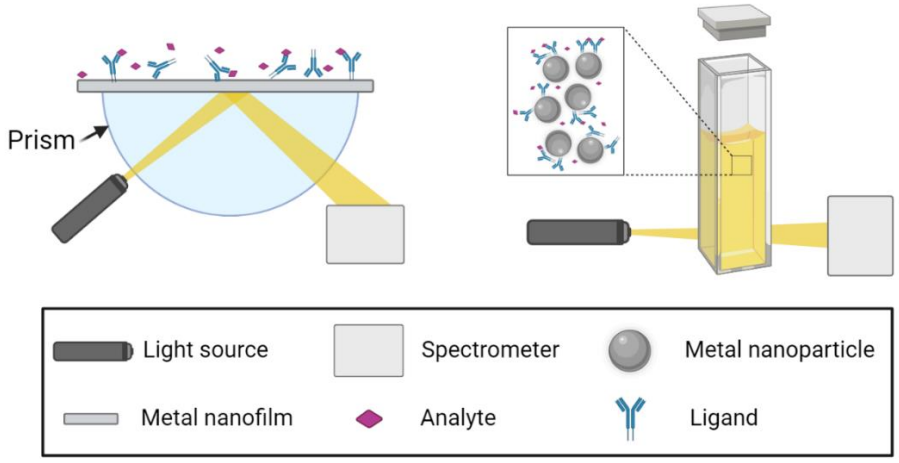


Figure 5 – Illustration showing SPR biosensing (left) and LSPR biosensing (right) – Created with BioRender.com

This is the basis of the sensing mechanism in LSPR/SPR Biosensors [31,33]. Unlike in SPR, where the induced plasmons oscillate along the metal-dielectric interface with electromagnetic field decay length in the order of 200 nm [34], LSPR occurs locally on the nanoparticle as shown in Figure 4 and the electromagnetic field decay length is in the order of 6 nm (it should be noted that in both cases, the field is decaying exponentially) [35]. The shorter electromagnetic field decay length in LSPR localizes the sensitivity to the refractive index change close to the nanoparticle's surface, thus reduces the interference from the refractive index of the bulk solution and enhances the sensors performance [31,33,36]. Additionally, SPR requires complex equipment and precise experimental setups to induce. In many cases, a prism is required to couple the light and increase the photons' momentum [37–39], whereas LSPR will occur only by the interaction of light with a nanoparticle with a smaller cross section than the wavelength of light as mentioned earlier [32]. For these reasons, along with the simpler fabrication requirements of FOEW LSPR biosensors, which will be discussed in the next section, LSPR was chosen as the sensing mechanism for this Thesis.

Silver nanoparticles are used in this work as they exhibit the highest sensitivity to changes in the local refractive index amongst plasmonic materials [40,41]. However, their toxicity to biological molecules should be thoroughly investigated before the commercialization of the sensor. Silver nanoparticles were reported to have cytotoxic and genotoxic effects [42]. This could potentially affect the integrity of the salivary sample, leading to altered biomarker readings and compromised sensor accuracy. The toxicity of silver nanoparticles to the user will be discussed in section 5.2

1.4 Fiber Optic Evanescent Wave Sensing

Fiber optic evanescent wave sensors have been a subject of interest for biological, environmental, and chemical applications [43–45]. The concept of FOEW sensors is to utilize the phenomenon of total internal reflection (TIR), which fiber optics are designed to retain by employing Snell's law [46]. In an optical fiber, the refractive index of the material surrounding the core, known as the cladding, is lower than the refractive index of the core. This allows TIR to occur for the electromagnetic rays coupled inside the fiber. However, the electric field associated with these electromagnetic rays extends into the material surrounding the core. This electric field is called the evanescent wave, and its magnitude decays exponentially with the radial distance from the core's interface. The evanescent wave penetration depth is a measure of how far this field extends into the medium. The penetration depth is a function of the incident angle of light, wavelength, and refractive indices of both the core and the medium around it [47]. As shown in Figure 6, removing the cladding will expose the evanescent field and allow it to interact with the medium, fundamentally creating a sensor.

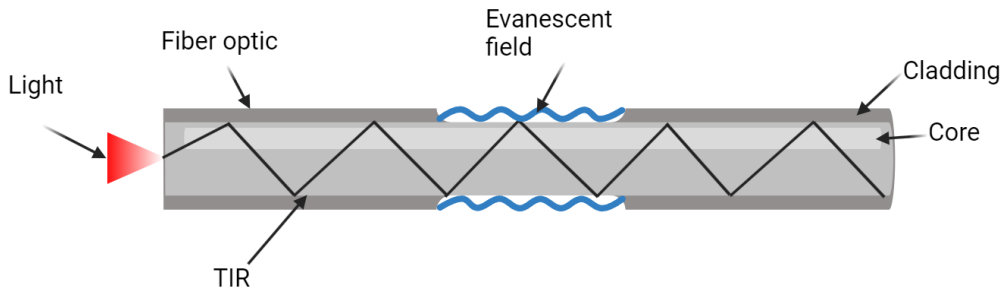


Figure 6 – Illustration of Evanescent field in an optical fiber – Created with BioRender.com

This is the concept of FOEW sensors. TIR will persist (even for an un-cladded fiber) as long as the refractive index surrounding the un-cladded portion is lower than the refractive

index of the core. If the refractive index of the medium is higher than that of the core, the coupled light will escape the fiber through the un-cladded portion into the medium. The signal will be lost, and the sensor will not operate effectively. In an absorbing medium, molecules close to the surface of the core and within the evanescent field penetration depth will interact with the evanescent wave, and absorb energy from it [48]. This causes an Attenuated Total Reflection (ATR) causing a loss in the light rays coupled inside the fiber at a specific wavelength. Detecting and analyzing the ATR provides accurate information about the properties of the absorbing medium. As stated in [49], an evanescent wave is not a propagating wave, despite being observed as if it propagates along the interface. The reason this is important to note is to highlight the nature of the evanescent wave. A propagating electromagnetic field can scatter when propagating in a scattering medium. Yet, research show that the TIR of an un-cladded fiber in a purely scattering medium would always remain total and will not be attenuated [49]. Hence, a FOEW sensor would only function in a medium that can absorb the evanescent wave. The output intensity of the light due to the interaction of the evanescent wave with the medium can be written as [48]:

$$I_f = I_0 e^{(-rCL_{int})} \tag{1.1}$$

Where r is the ratio of the optical power available in the evanescent wave to the total guided power, said ratio depends on the penetration depth of the evanescent wave, C is a constant, and L_{int} represents the interaction length, or the length of the sensing region. According to [48] " the sensitivity is proportional to the product rL_{int} … this improved performance can be achieved while still employing a thin sensing layer, meaning that sensor response time is not adversely affected".

Consequently, the longer the sensing region is, the higher the sensitivity will be. In addition to being highly sensitive [43], [50], FOEW sensors are also very versatile as their performance can be further improved by modifying the sensing region. Studies done to enhance the sensitivity of FOEW sensors show how physical alterations to the fiber can improve the sensor's performance. Tapering [51], bending [52,53], etching [54], grinding [55], coating [56], grating [57] and many other techniques have been successfully used in the literature. All these techniques have shown improved sensitives as they simply amplify the evanescent wave intensity and/or penetration depth, which in turn results in a significantly increased interaction with the medium, thus improving the sensors' performance. Due to the unique advantages FOEW sensors hold, such as high sensitivity, low cost, compact size [58], safe detection, versatility, and real-time fast monitoring [44], this type of sensors has been used in this thesis to monitor salivary cortisol levels.

1.5 FOEW LSPR Biosensor Fabrication and Sensing

FOEW LSPR biosensors generally combine the concepts presented in sections 1.2, 1.3, and 1.4 as the foundation of the fabrication and sensing mechanism. A schematic showing the main fabrication steps of the FOEW LSPR biosensor and the signal corresponding to each step is shown in Figure 7. Firstly, a fiber optic is un-cladded to expose the core which allows for the evanescent field to penetrate to the medium around the core, metallic nanoparticles are then adsorbed on the fiber optic's core that interact with evanescent field, allowing for an LSPR absorption signal to be detected as shown in Figure 7 (a). The ligand for the analyte under study is conjugated on the nanoparticles' surface, causing a change in the local refractive index

around the nanoparticles and a shift in the LSPR's absorption signal wavelength, creating a reference signal for the biosensor as shown in Figure 7 (b) [59].

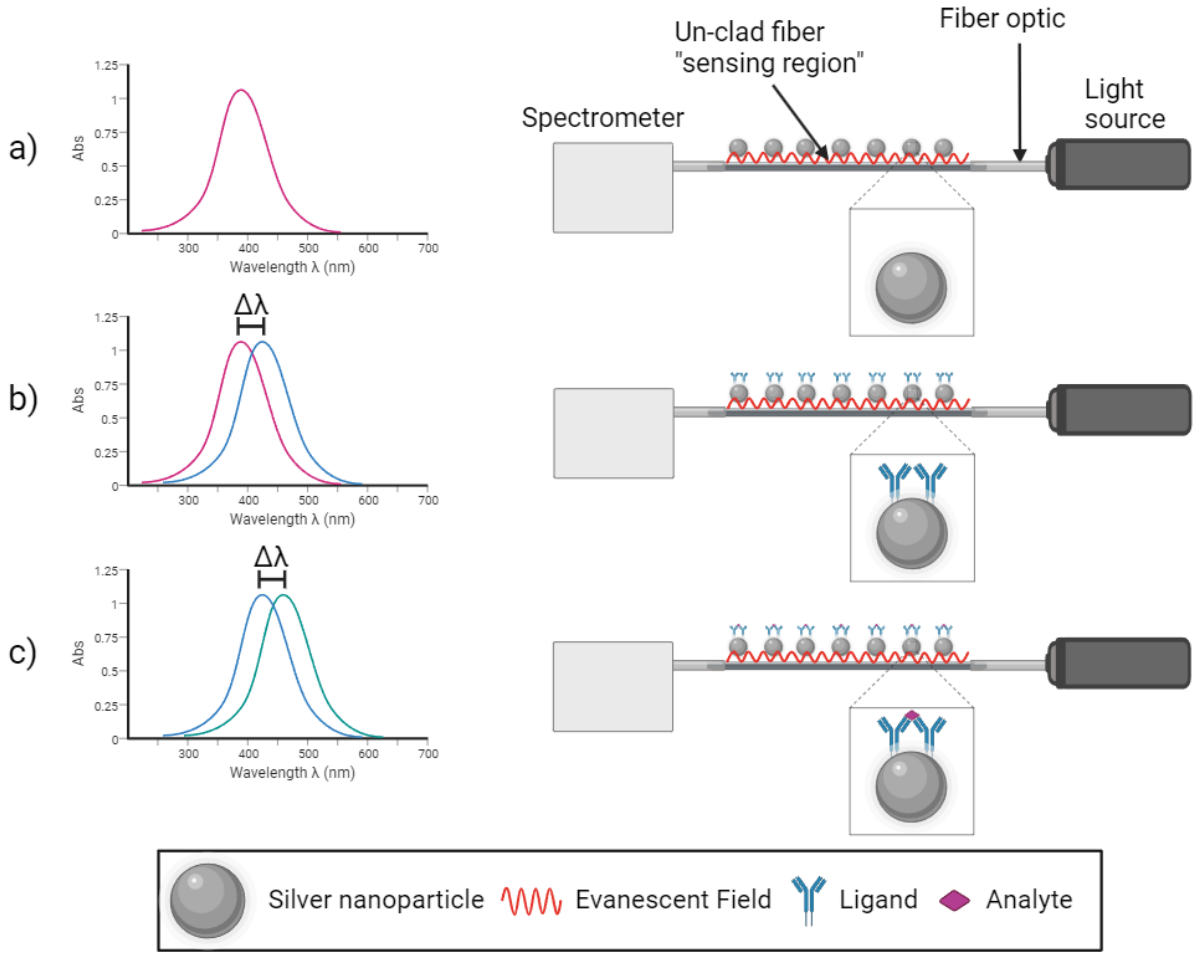


Figure 7 – Illustration showing the fabrication and sensing concepts behind FOEW LSPR biosensors. a) LSPR absorption signal due to metallic nanoparticle adsorption on the sensing region. b) LSPR absorption signal wavelength shift due to ligand conjugation. c) LSPR absorption signal shift due to ligand-analyte interaction – Created with BioRender.com

Finally, a sample containing a known concentration of the analyte is allowed to flow over the sensing region during testing. The interaction between the analyte and the ligand further changes the local refractive index around the nanoparticles, causing another shift in the LSPR's absorption signal wavelength, which is represented in Figure 7 (c). This shift is

correlated to the known concentration of the analyte. Different concentrations are used and correlated to the amount of LSPR absorption signal shift to determine the characteristics of the sensor. Although the sensing concept is simple, great challenges lay in the fabrication process including but not limited to the preparation of the sensing region, the functionalization of the sensing region for nanoparticle deposition, the functionalization of the nanoparticles for the ligand conjugation, the reagents and concentrations used, and results interpretation and analysis.

1.5.1 Nanoparticle Immobilization Techniques

The proper immobilization of metallic nanoparticles on the optical fiber is a crucial step in the fabrication of the LSPR sensor. There are many nanoparticle immobilization techniques reported in the literature [60]. However, this work will consider the nanoparticle self-assembly method. The process of nanoparticles immobilization on a substrate using self-assembly is simple and well-studied [61]. Chemical functional groups are first created on the substrate surface through polymerization or salinization procedures, this process is called "Surface functionalization." The substrate is then immersed in a nanoparticle colloidal solution for a specific period. The final characteristics of the nanoparticles layer immobilized on the substrate's surface depend on many factors, including but not limited to, the interaction potential between the nanoparticles and the functional groups, nanoparticles and adsorbate characteristics, the immersion time and the direction [62], the rate at which the substrate is removed from the colloidal solution, pH and temperature of the solution, and other experimental factors [63]. The nanoparticles immobilized using self-assembly form, in many

cases, self-assembled monolayers (SAMs) or multilayers with nanoparticles being clustered on the surface.

Electrostatic immobilization is based on the attraction potential between the natural charge of the nanoparticles or the charge of the stabilizing agent, and the opposite charge of the substrate surface. Nanoparticles can be synthesized in solutions containing the desired stabilizing agent to obtain the required charge, while the substrate is functionalized with molecules that provide the opposite charge. For silver, common stabilizing agents used include plants extract, PVP, and citrate. It should be noted that different capping agents affect size, morphology, and stability of the silver nanoparticles [64]. Covalent immobilization allows charged or uncharged nanoparticles to bond to the surface. Like electrostatic immobilization, the surface of the substrate must be functionalized, only to generate the necessary functional groups that form bonds with the nanoparticle. Polymerization or salinization of the glass can be achieved using either polyelectrolytes such as Polyethyleneimine (PEI), or Poly(allylamine hydrochloride) (PAH), or thiols and amino silanes such as (3-aminopropyl)triethoxysilane (APTES), aminopropyldiethoxymethylsilane (APDMS), or 3-Mercaptopropyl Triethoxysilane (MPTES). Thiols, in particular, have strong affinity towards silver nanoparticles, making them excellent for functionalization [65], but amino silanes can also be used as effectively. This form of immobilization is more robust and is preferred over electrostatic immobilization. A widely employed approach to functionalize the substrate surface for nanoparticle immobilization involves the attachment of functional silanes, given their strong affinity for most metals, leading to the formation of stable bonds [66]. In this thesis, the commonly used APTES will be utilized. APTES facilitates surface modification by attaching functions that enhance the

adsorption and allow for electrostatic bonds with metallic nanoparticles. The reaction of silane surface modifiers can be controlled yet considered very intricate. The growth kinetics of APTES SAMs and their final morphology were reported to be influenced by factors such as reaction duration, solution concentration, and temperature [67]. Some of these factors will be investigated in Chapter 3.

1.5.2 Ligand – Nanoparticle Conjugation Techniques

Since the aim is to use silver nanoparticles in the biosensor, where accuracy and reliability are crucial, it is imperative to correctly choose the targeting ligand and the best strategy to conjugate it to the nanoparticles' surface [68]. Many physical and chemical methods have been used in the literature to conjugate functional groups (of antibodies, aptamers, etc.…) with nanoparticles [69]. Conjugation based on electrostatic interactions, for instance, is considered the easiest conjugation concept as it allows antibodies to simply adsorb on the nanoparticles surfaces due to electrostatic attraction forces. Although simple, this method has major shortcomings. For instance, a high concentration of the functional groups is required to prepare the conjugates. Additionally, the functional groups can adsorb at random orientations, which could interrupt the interaction with the ligand. Finally, when using complex samples, there is a high possibility of the functional groups to be replaced by other molecules as they are noncovalently attached to the NPs. [70–72]. In [73], the antibodies were adsorbed on the nanoparticles surfaces through both hydrophobic and ionic interactions which were then used as electrochemical label. Physical interactions between gold NPs and antibodies are based on three main principles, which are shown in Figure 8.

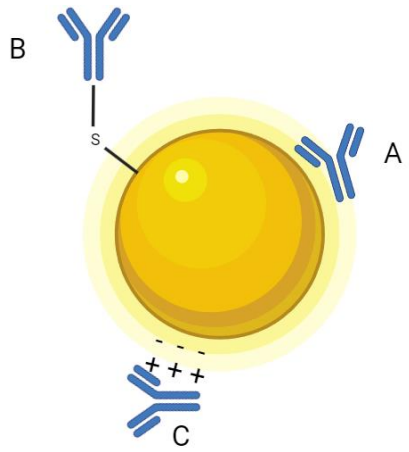


Figure 8 – physical interactions between antibodies and nanoparticles adopted from [69] *– Created with BioRender.com*

The first is represented by the letter (A), this is the hydrophobic attraction between the antibodies and the NPs' surface. The second, represented by the letter (B) is dative binding, which occurs between the conducting electrons on the NPs and the atoms of the amino acid of the antibodies creating a covalent bond. Finally, the third (C) is the ionic attraction, this is due to the fact the NPs are negatively charged while the functional groups on the antibodies are positively charged. As for chemical interactions, they could be achieved through Adapter molecules like streptavidin and biotin, bifunctional linkers, or chemisorption via thiol derivatives [69]. The conjugation method that will be used in this work is based on covalent binding between the nanoparticles and the antibodies. The most extensively used reagents for this method are 11-Mercaptoundecanoic acid (MUA) or Cysteamine Hydrochloride, 1-ethyl-3-(3-dimethylaminopropyl)carbodiimide hydrochloride (EDC), and N-hydroxysuccinimide (NHS) [74–76]. 11-MUA or Cysteamine Hydrochloride are used to functionalize the nanoparticles' surface. Amide bonds can then be formed with the antibodies by using EDC/NHS chemistry which will be explained in detail in Chapter 4.

1.6 Status of FOEW LSPR/SPR based Biosensors

Table 1 below summarizes some of the FOEW LSPR/SPR biosensors found in the literature and provides helpful insights on the design of the FOEW, the fabrication and functionalization processes, and the characteristics of this type of sensors.

Table 1 – Current literature on FOEW LSPR/SPR sensors

No.	Optical Fiber	Fabrication	Functionalization	Method	Output Signal	Biomarker Detected	Sensitivity	LOD	Range	Ref
1	POF-MM-600-0.37-5	20 nm AU NP - spheres	Aqueous CD and GOx	EPM	ABS	Glucose	150 µl	NA	0-250 mg/dl	[77]
2	SOF-MM-600-NA-2	60 nm AU NP - spheres	11 - MUA modified with EDC /NHS, human IgG	EPM	Δλ	Anti-human IgG	914 nm/RIU	1.6 nM	NA	[78]
3	SOF-MM-600-NA-2	AU NP – rods 4.1 (AR)	11 - MUA modified with EDC/NHS, human IgG	EPM	Δλ	Anti-human IgG	601 nm/RIU	1.6 nM	NA	[78]
4	HCF-SM-5-NA-0.2	11 nm AU NP - spheres	MUA modified with EDC/NHS, ChOx	EPM	REF	Cholesterol	16.149 nm/µM	25.5 nM	50 nM - 1µM	[79]
5	SOF-MM-600-0.22-2	48 nm AU NP - spheres	NA	EPM	ABS	Antibody assays	13.09 AU/RIU	NA	NA	[80]
6	SOF-MM-600-0.22-2	23 nm AU NP - spheres	NA	EPM	ABS	Antibody assays	5.85 AU/RIU	NA	NA	[80]
7	SOF-SM-4-NA-1	10.5 nm AU NP - spheres	MUA modified with EDC/NHS, ChOx	EPM	REF	Cholesterol	125.47 nm/µM	53.1 nM	10 nM - 1µM	[81]

No.	Optical Fiber	Fabrication	Functionalization	Method	Output Signal	Biomarker Detected	Sensitivity	LOD	Range	Ref
8	POF-MM-600-0.37-5	15-20 nm AU NP - spheres	Aqueous CD and TDx	CFM	ABS	Taurine	0.019 AU/mM	53 μM	0 – 1 mM	[82]
9	POF-MM-600-0.37-1	15-20 nm AU NP - spheres	Aqueous CD and L-GDH/NAD^+	CFM	ABS	Glutamate	0.0048 AU/mM	0.36 mM	0 – 10 mM	[83]
10	POF-MM-1000-0.5-1	L-Tyrosine capped Ag NPs	NA	EPM	INT	Dopamine	NA	0.16 μM	0 – 50 mM	[84]
11	POF-MM-600-0.39-3	Green-synthesized Ag NPs	NA	CFM	ABS	Dopamine	3 nm/ μM	2×10^{-7} M	0 - 80 μM	[85]
12	POF-MM-600-0.37-0.5	50 nm thick AU layer	PDA layer, anti CRP	EPM	Δλ	C-reactive protein	1.17 nm/(μg/mL)	NA	0.01-20 μg/ml	[86]
13	POF-MM-600-0.37-1.5	48 nm thick AU layer	NA	CFM	Δλ	Urine specific gravity	856.09 nm/SG	NA	1.0144 - 1.0352	[87]
14	POF-MM-600-0.37-1	50 nm thick AU layer	Aqueous CD and GOx	CFM	Δλ	Glucose	0.0366 nm/(mg/dl)	NA	0-250 mg/dl	[88]
15	POF-MM-600-0.39-1	<10 nm Diosmin capped Ag NPs	NA	CFM	ABS	Cysteine	NR	0.0077 μM	0-100 μM	[89]
16	SOF-SM-4.3-NA-4	40 nm AU NP – nanodisk array	Phosphate buffer solution with EDC/NHS, mAbs	EPM	Δλ	free prostate specific antigen	226 nm/RIU	100 fg/mL	NA	[90]
17	SOF-MM-105-NA-NA	47 nm AU NP - spheres	borate buffer solution with IFN-γ	EPM	INT	antibody-antigen	10.494/RIU	NA	0.01 to 100 ng/ml	[91]
18	SOF-SM-9-NA-NA	10 nm AU NP - spheres	MUA modified with EDC/NHS, GOx	EPM	Δλ	Glucose	1.06 nm/mM	2.26 mM	0-11 mM	[92]

Notes:

- Optical fiber code (Construction) – (Multi/Single mode) – Diameter (in μm) – Numerical Aperture – Sensing Length (in cm)
- ABS = Absorbance
- CD = cysteamine dihydrochloride
- CFM = Continuous Flow Monitoring
- ChOx = cholesterol oxidase
- EDC = 1-Ethyl-3-(3-dimethylaminopropyl) carbodiimide
- EPM = End Point Monitoring
- GOx = Glucose Oxidase
- HCF = Hollow Core Fiber
- IFN-γ = interferon-gamma
- INT = Intensity
- L-GDH = L-glutamate dehydrogenase
- mAbs = Antibodies
- MM = Multi-Mode
- MUA = Mercaptoundecanoic acid
- NAD^+ = nicotinamide adenine dinucleotide
- NHS = N-hydroxysuccinimide
- NR = Not reported.
- PDA = polydopamine
- POF = Plastic Optical Fiber
- REF = Reflection Signal
- RIU = Refractive Index Unit
- SM = Single-Mode
- SOF = Silica Optical Fiber
- TDx = taurine dioxygenase

1.7 Objectives of this Thesis

The circadian rhythm nature of cortisol imposes a great challenge for traditional sensing methods, which require a significant amount of time to return the test results. As highlighted in section 1.1, to gain a deeper understanding of Cortisol's role in mental disease progression, there is a great demand to investigate the real-time expression of this biological marker [23] . Therefore, there is an imperative need for the advancement of label-free biosensors that not only enable continuous and non-invasive testing and monitoring of cortisol, but also have attributes such as high sensitivity, accessibility, portability, cost effectiveness, and ultimately user friendly [93]. A FOEW LSPR biosensor possesses these attributes and has the potential to transform the cortisol testing for point-of-care applications.

The information found in the literature for biosensors of similar construction to the one presented in this work focus on the fabrication process and the results, with few attempts made for cortisol detection. To the best of our knowledge, there is no comprehensive study that includes the modeling of the parameters for a FOEW LSPR cortisol biosensor that affect the sensor response, the optimization of these parameters to maximize the sensitivity, and the validation of the results via experiments. The aim of this work is to provide this comprehensive study through modeling, validate the results experimentally, and produce a working biosensor sensitive enough for salivary cortisol detection using a coreless fiber as the sensing region and silver nanoparticles which have the highest sensitivity amongst plasmonic materials. This combination significantly improves the sensor's characteristics [94], simplifies the fabrication and testing processes [95], enhancing the repeatability and reliability.

Chapter 2
Modeling the Parameters Affecting Sensor Signal and Performance

2.1 Introduction

The current chapter investigates the significance of various parameters affecting the performance of Fiber-Optic Evanescent Wave (FOEW) Localized Surface Plasmon Resonance (LSPR) biosensors through numerical and analytical modeling techniques. It highlights the importance of this investigation in optimizing sensor sensitivity and fabrication process, contributing to a deeper understanding of this type of biosensors.

2.2 Modeling nanoparticle absorption and adsorption kinetics

A comprehensive combined numerical and analytical model that examines the effect of spherical nanoparticles size on the sensor's signal and the kinetics of nanoparticle adsorption on the optical fiber is presented in this section. First, a numerical model using ANSYS LUMERICAL that identifies the nanoparticle size which yields the highest absorption signal is presented. An analytical model that explains the nanoparticle adsorption kinetics based on nanoparticle size follows. Finally, an analytical model that connects the optical fiber response based on the nanoparticle size and adsorption kinetics is derived.

Silver spherical nanoparticles that exhibit LSPR absorption and are commercially available range in size between 10 – 100 nm. LSPR of these sizes can be captured using generalized Mie theory, which is essentially a solution to Maxwell's equations that explains the extinction (absorption + elastic scattering) of light interacting with nanoparticles [96]. For different nanoparticle shapes, there is no analytical solution; Maxwell's equations with the

proper boundary conditions must be solved numerically. The extinction spectrum of a spherical nanoparticle using Mie theory is described as [97]:

$$C_{ext} = \frac{24\,\pi^2\,N\,r_{np}^3\,\varepsilon_m^{3/2}}{\lambda \ln(10)}\left[\frac{\varepsilon_i(\lambda)}{(\varepsilon_1(\lambda)+\chi\,\varepsilon_m)^2+\,\varepsilon_2(\lambda)^2}\right] \quad (2.1)$$

where N is the electron density of metallic nanospheres, r_{np} is the nanoparticle radius, $\varepsilon_m$is the medium's dielectric constant, λ is the wavelength of the incident light, and ε_1 and ε_2 are the real and imaginary parts of the materials dielectric function. χ is the shape factor which changes based on the geometry of the nanoparticle. For spherical nanoparticles, this shape factor is 2. The electric field on a spherical nanoparticle's surface is given by [98]:

$$E(x,y,z) = E_0\hat{k} + \left[\frac{\varepsilon_{np}-\,\varepsilon_m}{\varepsilon_{np}+\,2\varepsilon_m}\right] r^3 E_0\left[\frac{1}{r^3}\hat{k} - \frac{3z}{r^5}\left(x\hat{\imath}+y\hat{\jmath}+z\hat{k}\right)\right] \quad (2.2)$$

Based on these equations, when the real part of the metals' dielectric function is equal to $-2\varepsilon_m$, the denominator of both equation reaches its lowest value possible, causing a peak in the extinction spectrum, and a very high electric field on the nanoparticle's surface. This indicates resonance conditions are met, and LSPR can be detected. The LSPR conditions are also reflected in the polarizability. For spherical nanoparticles, the polarizability can be given by [32]:

$$P = 4\varepsilon_0\pi r_{np}^3\,\frac{\varepsilon_{np}-\varepsilon_m}{\varepsilon_{np}+2\varepsilon_m} \quad (2.3)$$

where ε_0 represents the permittivity of free space. When resonance conditions are met, the polarizability reaches its maximum value. This phenomenon can only occur in metals, as other materials always have positive real dielectric constants. The dielectric function for metals can be approximated by the Drude model below [99]:

$$\varepsilon_1 = 1 - \frac{\omega_p^2}{\omega^2 + \gamma^2} \tag{2.4}$$

where ω_p is the plasma frequency, ω is the angular frequency of the electromagnetic radiation, and γ is the damping frequency. γ is the reciprocal of τ, which is the mean free time between collisions for the electrons in the bulk metal. In the visible region γ is orders of magnitude less than ω_p [32] ;consequently, the above equation becomes:

$$\varepsilon_1 = 1 - \frac{\omega_p^2}{\omega^2} \tag{2.5}$$

Rearranging at resonance conditions, the LSPR frequency can be determined by:

$$\omega_{LSPR} = \frac{\omega_p}{\sqrt{2\varepsilon_m + 1}} \tag{2.6}$$

It is evident that the LSPR frequency is a function of the plasma frequency and the medium dielectric constant. However, it should be noted that the size, shape, material, and aggregation of the nanoparticles directly affect the plasma frequency, which evidently impacts the LSPR frequency. While these effects are not captured in equation (2.6), they are well understood in the literature. Bigger nanoparticle sizes and aggregation of the nanoparticles

slow down the plasma frequency, which results in a redshift in the LSPR wavelength. Nanoparticles with asymmetrical shapes can produce LSPR at multiple wavelengths, while different materials (i.e. gold, copper, aluminum, etc.) inherently have different plasma frequencies [32].

2.2.1 Nanoparticle absorption – numerical model

ANSYS LUMERICAL Discontinuous Galerkin Time-Domain (DGTD) module was used to model the interaction of light with silver nanoparticles and study the effect of increasing the number of nanoparticles on the extinction of light. DGTD solves Mie's theory numerically and provides the extinction of the nanoparticle under study as absorption + scattering. Almost infallibly, simulations on silver nanoparticles interaction with light use silver optical data from Johnson's and Christy's (J&C) 1972 tabulation, or Palik's 1985 handbook [100]. For this work, the simulation was done once using J&C tabulation data [101] and once using Palik's data [102] and the results were averaged out.

The model consisted of a single spherical silver nanoparticle placed in a medium with refractive index equals 1.34 (water) and is significantly larger than the nanoparticle. The boundary around the medium is defined as the absorbing layer and the surface of this layer is set to be the source of the electromagnetic wave. A frequency monitor is used to calculate the extinction of light due to the interaction with the nanoparticle, which is placed on the surface of the absorbing layer as well. This allows the software to separate the extinct light, and the light injected by the source. The electromagnetic wave is set as a plane wave with an amplitude of 1 V/m and a wavelength ranging from 350 nm to 750 nm. The model construction is shown

in Figure 9 (a). The scattering cross section C_{scat}, and the absorption cross section C_{abs}, in units of $[A.u\ m^2]$ were calculated, where $A.u$ stands for Arbitrary units, and it is a unitless measurement for the optical density. The extinction cross section C_{ext} was computed by adding C_{scat} and C_{abs}. A plot of C_{ext}, C_{scat}, and C_{abs} generated for a nanoparticle with 80 nm diameter is shown in Figure 9 (b). Simulations show how both scattering and absorption contribute to LSPR with different magnitudes, which is expected [99].

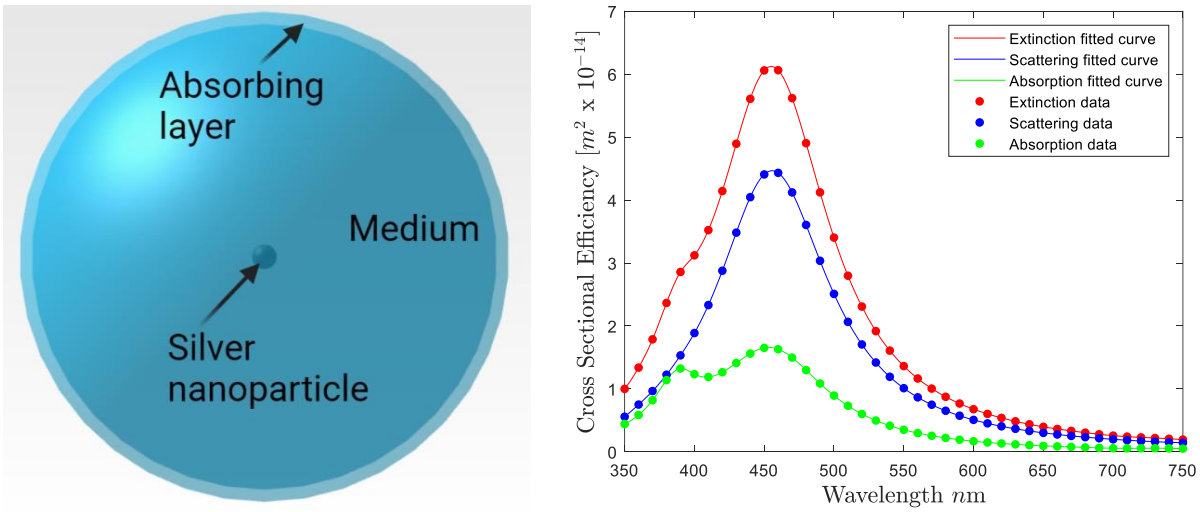


Figure 9 – (a) The construction of the model in ANSYS LUMERICAL (left) – (b) Extinction, Scattering, and Absorption cross section for an 80 nm silver nanoparticle in a 1.34 refractive index medium (right)-(cubic spline fit used to cover all simulation points)

Scattering and absorption cross-sections were also simulated for single silver nanoparticles of varying diameters ranging from 10 to 100 nm, in steps of 10 nm. The maximum LSPR peak was recorded for each studied size and plotted in Figure 10 (a). The LSPR peak occurred at varying wavelengths. However, the results show that for all these three phenomena, larger nanoparticles have a higher extinction, scattering, and absorption cross section.

Although true for the cross-section, this is not found to be true for the efficiency. The dimensionless extinction, scattering, and absorption efficiencies Q_{ext}, Q_{scat}, and Q_{abs} are obtained by dividing the cross-section results by the cross-sectional area of the nanoparticle. This was done for the same range of silver nanoparticle sizes used to generate Figure 10 (a), and the results are shown in Figure 10 (b).

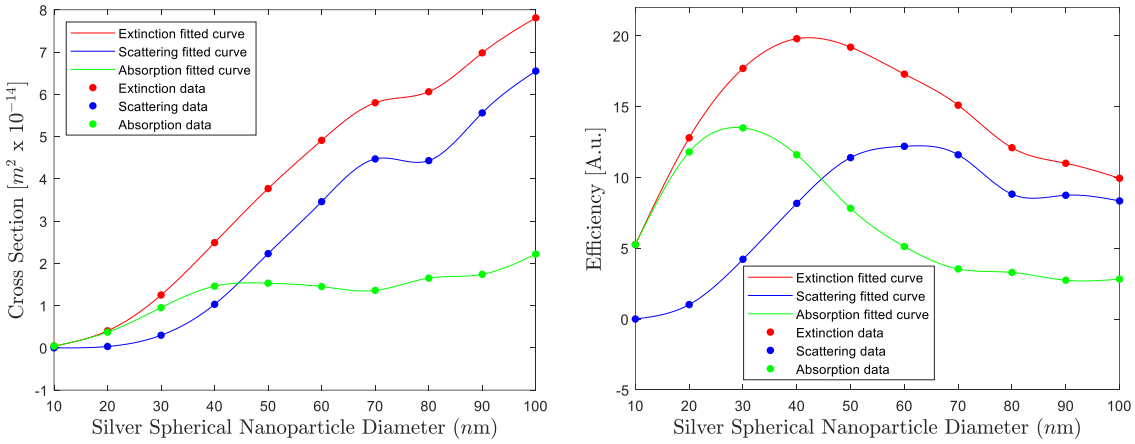


Figure 10 – (a) Maximum LSPR cross section peak for each silver nanoparticle size ranging from 10 nm to 100 nm at their respective wavelength (left) – (b) Maximum LSPR efficiency peak for silver nanoparticles with size ranging from 10 nm to 100 nm, in steps of 10nm, at their respective wavelength (right). (cubic spline fit used to cover all simulation points)

These results show how efficiency changes with size with no perceivable relation. Comparing the results in Figure 10 (a) and (b), and specifically looking at the sizes 10, 20, 30, and 80 nm, the following is noticed. Figure 10 (a) shows that silver nanoparticles with diameter equal to 80 nm absorb light more efficiently during LSPR compared to nanoparticles with diameter equal to 10, 20, and 30 nm. However, Figure 10 (b) shows the opposite. Considering that the parameter under study in Figure 10 (a) is the cross-section, while in Figure 10 (b) it is the efficiency, sizes 10, 20, 30, and 80 nm nanoparticles were studied in this work, to determine which parameter is more important when considering a FOEW based sensor.

To further investigate why the 30 nm size has the highest absorption efficiency, the formula for the absorption of a spherical particle was considered, which is given by [99]:

$$Q_{abs} = \frac{8\pi R}{\lambda}\, Im\left\{\frac{\varepsilon_{np} - \varepsilon_m}{\varepsilon_{np} + 2\varepsilon_m}\right\} \tag{2.7}$$

Where R is the radius of the nanoparticle, λ is the wavelength of light, Im refers to the imaginary part of the expression between brackets, ε_{np} is the dielectric constant of the particle, and ε_m is the dielectric constant of the surrounding medium. The dielectric constant of the particle is a function of the frequency of light interacting with it, which will be discussed in detail in the Drude-Lorentz model in section 2.3.2.

LSPR occurs at the frequency where $\varepsilon_m \cong -2\varepsilon_{np}$, causing the denominator to approach 0 and the absorption to spike. The frequency at which this occurs is known as Fröhlich frequency, which is a function of the particle size, material, shape, and medium surrounding the particle [99]. Based on Figure 10 (b), it appears that for silver nanoparticles of size ≅ 30 nm, the value of the Fröhlich frequency would result in the highest imaginary value in eq (2.7), which explains why this specific size would have the highest absorption efficiency when compared to other silver nanoparticle sizes.

Further modeling was performed to examine the relation between Q_{abs} and the number of nanoparticles using silver nanoparticle with diameter equal to 80 nm. The number of nanoparticles was increased arbitrarily to 9, 25, 58, and 89 particles, and the results of the total Q_{abs} at each size was plotted in Figure 11. The results show how the absorption efficiency

increases linearly as the number of particles increases. This was repeated for different sizes of nanoparticles and the findings were consistent. These results were expected as the simulations were performed on nanoparticles separated with distances greater than the diameter of one particle from each side, this ensures that the electric field from the LSPR of one nanoparticle does not interfere with its neighboring nanoparticles and influence the results. As discussed earlier, aggregation affects the plasma frequency and impacts the LSPR frequency. Although this is not the case during the self-assembly process, which will be shown in the experimental results, for the purpose of simplifying the model, these effects were not included.

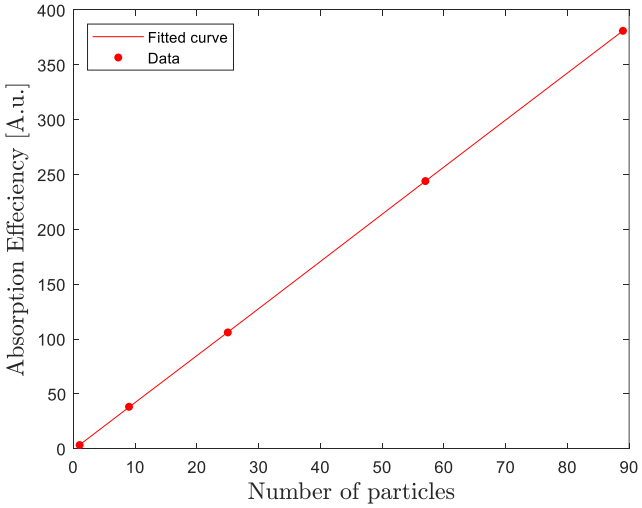


Figure 11 – Relation between LSPR absorption peak and number of nanoparticles

From these findings, the model suggests that different nanoparticles sizes (which includes shapes and materials) have unique scattering and absorption efficiencies with no distinct trend that can be followed, which is not the case compared to scattering and absorption cross section. Additionally, the model also showed a positive correlation between the number of nanoparticles and the absorption efficiency. These results highlight that the performance of

a FOEW LSPR sensor can be maximized by optimizing nanoparticles for high absorption efficiency and high final nanoparticle surface density adsorbed on the sensing region.

2.2.2 Nanoparticle adsorption kinetics – analytical model

Monolayers of silver nanoparticles adsorbed on a substrate treated with cationic polyelectrolyte have been previously studied in the literature [63,103–105]. When a substrate treated with a cationic polyelectrolyte is immersed in a nanoparticle colloidal solution, the nanoparticles adsorb on the surface, and the kinetics are governed by the diffusion transport process [63,103]. In this case, the surface density is proportional to the immersion time at shorter immersion periods, while at longer periods, the interarticular repulsion forces come to play, preventing the particles' build-up, resulting in a saturated monolayer surface coverage. Excluding the effect of the monolayer, the surface density N_s can be described using [103]:

$$N_s = 2\sqrt{Dt/\pi}\ C_b \tag{2.8}$$

Where D, t, and C_b are the diffusion coefficient ($\mu m^2/s$), immersion time (s), and the bulk number concentration, respectively. The surface density is proportional to $\sqrt{t}$. The diffusion coefficient can be calculated using the Stokes-Einstein equation [103]:

$$D = \frac{kT}{3\pi\eta d_H} \tag{2.9}$$

where d_H is the hydrodynamic diameter of the particle, k is the Boltzman constant, η is the viscosity of the solvent of the colloidal solution, and T is the absolute temperature. The bulk number concentration C_b is related to the weight concentration c_w through [77]:

$$C_b = \frac{6 \times 10^{-6}}{\pi \, d_{np}^3 \rho_{np}} \, c_w \tag{2.10}$$

where d_{np} is the average diameter of the particle, ρ_{np} is the density of the particle (i.e., silver), and c_w is the weight concentration expressed in ppm. Higher concentrations of nanoparticles in a colloidal solution will result in higher surface density; however, higher surface densities can also be achieved with longer adsorption times.

The bulk number concentrations for the particles used were calculated using equation (2.10). The diffusion coefficients were calculated using equation (2.9) . The procured 30 nm particles had a hydrodynamic diameter of 37 nm, while the 80 nm particles had a hydrodynamic diameter of 91 nm. Both had a concentration, c_b, of 20 ppm. The diffusion coefficient for each particle was then used to calculate the surface density using equation (2.8) and the results are shown in Figure 12 (a). After 24 hours of adsorption, the 30 nm particles result in a surface density of 81 particles (μm^{-2}). That is more than 23 times the expected surface density of the 80 nm nanoparticles for the same bulk number concentration and over the same adsorption period, which was only 3.5 particles (μm^{-2}).

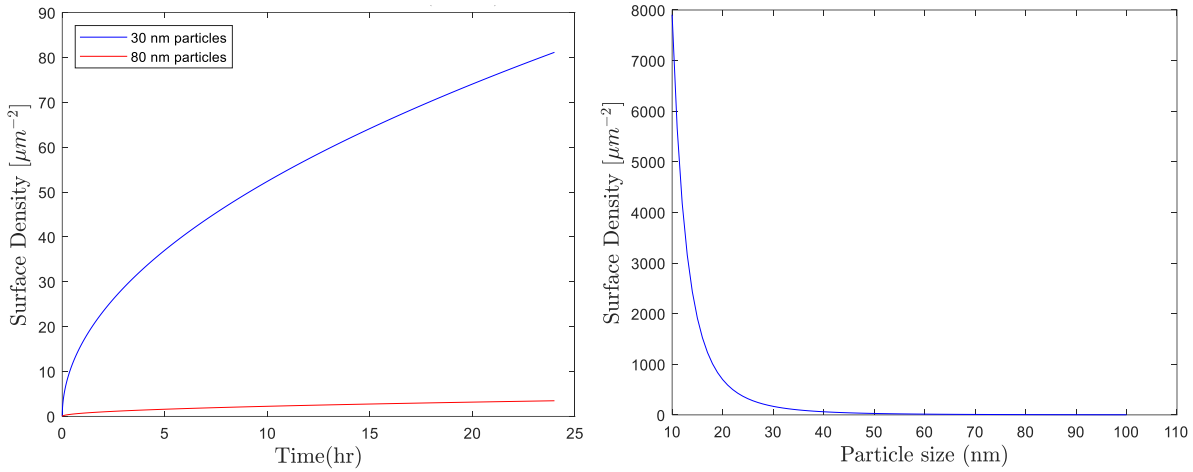


Figure 12 – (a) Comparison between the surface density of 30 nm and 80 nm particles after 24 hours of adsorption (left) – (b) Effect of size on surface density after 24 hours of adsorption (right)

Figure 12 (b) shows the effect of size on the surface density after 24 hours of adsorption. It can be concluded that fabricating the sensor using smaller nanoparticles will always result in a higher surface density for the same weight concentration and adsorption time.

Referring to both Figure 11 and Figure 12 (b), the argument can be made that utilizing 10 nm or 20 nm sizes during the fabrication process will result in a higher final absorption signal due to the higher final surface density compared to 30 nm, despite these sizes having a slightly lower absorption efficiency as shown in Figure 10 (b). However, as previously mentioned, this model doesn't include the effect of the monolayer formation which will stop the adsorption process once formed, reducing the dramatic variations in final surface densities reflected in Figure 12 (b). Nonetheless, this argument will be further investigated through modeling in section 2.3.4 and experimentally in Chapter 3 by studying the characteristics of FOEW LSPR sensors fabricated with these three sizes.

Considering the results from the numerical model in section 2.2.1, it is expected that using 30 nm nanoparticles in the fabrication of the sensor is significantly better than using 80 nm nanoparticles. The 30 nm nanoparticles proved to have higher absorption efficiency, and result in a higher surface density of the nanoparticles. This translates into an enhanced signal as more particles are contributing to the absorption of light at a higher absorption efficiency.

2.2.3 Optical fiber response – derived analytical model

The absorption of electromagnetic waves experiencing TIR in an optical fiber is affected by the resulting evanescent field at the material boundary. Light transmitted through an uncladded fiber immersed in an absorbing medium will result in an attenuated total internal reflection (ATR), which can be utilized for sensing based on the following expression derived for multimode fibers [106]:

$$P(z) = P_0\, e^{(-\tau z)} \tag{2.11}$$

where, P_0 is the initial power transmitted through the fiber, τ is the evanescent field absorbing coefficient, and z is the length of the uncladded fiber immersed in the absorbing medium in units of cm. For multimode fibers, τ can be related to the bulk absorption coefficient of a medium, α, using [106]:

$$\tau = r\alpha \tag{2.12}$$

where r is the fraction of power outside the core and can be calculated from [106]:

$$r = \frac{4\sqrt{2}}{3V} \tag{2.13}$$

where V is the normalized frequency parameter of the fiber given by [106,107]:

$$V = \left(\frac{2\pi r_f}{\lambda}\right) NA \tag{2.14}$$

Where r_f is the fiber core radius, NA is the numerical aperture in which light of wavelength λ is propagating. The normalized frequency parameter determines the fraction of the optical power in the mode confined to the core and can be used to determine whether the optical fiber is single or multi-mode. A normalized frequency parameter that is less than 2.405 indicates that the fiber can only guide one mode (i.e., single mode fiber), while higher values indicate that the fiber can guide multiple modes through its core (i.e., multi-mode fiber).

$$NA = \sqrt{n_{core}^2 - n_{clad}^2} \tag{2.15}$$

Where n is the refractive index of the material. Combining equations (2.11) to (2.14), the final absorbance of the evanescent field affecting the total power transmitted through the fiber is:

$$A = \frac{4\sqrt{2}}{3V} \frac{\alpha\, z}{2.303} \tag{2.16}$$

The bulk absorption coefficient of a medium α has units of $(A.u/cm)$. A.u stands for Absorbance units, and it is a unitless measurement for the optical density or Absorbance. To represent the absorbance of an LSPR evanescent wave optical fiber sensor with nanoparticles adsorbed on the core's surface, equation (2.16) is modified by replacing the absorption coefficient of the medium α with the absorption of the nanoparticle α_{np}. The length of the uncladded fiber z is replaced by the particle density N_s multiplied with the surface area of the uncladded fiber A_s since the total absorbance depends on the number of particles adsorbed on the surface. The final equation becomes:

$$A = \frac{4\sqrt{2}}{3V}\,(Q_{abs})(N_s)(A_s)(k) \tag{2.17}$$

where Q_{abs} is the absorption of a single nanoparticle$(A.u/particle)$, N_s is the particle density $(particle/\mu m^2)$, A_s is the surface area of the sensing region (μm^{-2}), and k is a correction factor. The reason k is necessary is to capture effects of nanoparticle spacing and nanoparticle monolayer formation on the absorption signal in a future model. These effects are highlighted in the final section of the modeling. For the purpose of this work, k will be a constant. It can be noted that since the sensor is evanescent field based, equation (2.17) is a function of the absorption of the nanoparticle only, not the total extinction of the particle as shown in [108].

2.2.4 Combined models result

From the results shown in the previous modeling sections, it can be concluded that using 30 nm nanoparticles could result in a significantly higher absorption in the LSPR signal due to their larger absorption coefficient, and higher surface density when compared to 80 nm nanoparticles. The total absorbance as a result of the LSPR effect during adsorption can be obtained by combining equations (2.8) and (2.17) into one model. Figure 13 shows the total LSPR signal absorbance as a function of wavelength using 30 nm nanoparticles for the final combined model in a medium such as water, which has a refractive index equal to 1.34.

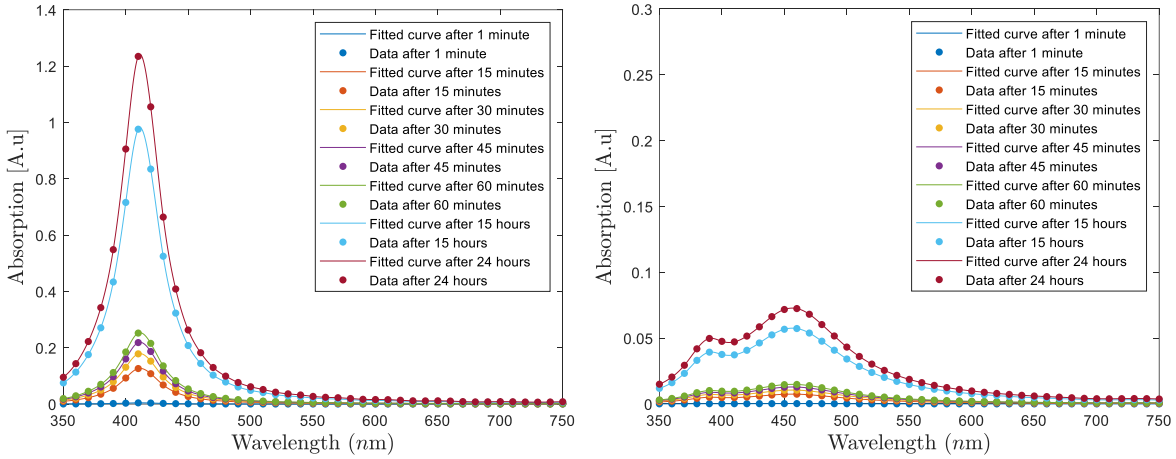


Figure 13 – FOEW LSPR absorption obtained from the combined model for (a) 30 nm nanoparticles (left) – (b) 80 nm nanoparticles (right) (cubic spline fit used to cover all simulation points).

Figure 13 concludes that the absorbance increases over time as the number of particles adsorbed on the surface increases. Additionally, the rate of change in LSPR absorbance signal suggests faster adsorption rate initially, which slows down over time. This is expected since according to the numerical absorption model of nanoparticles, the absorption increases proportionally with the number of particles, and according to the diffusion transport process

adsorption model, the number of particles adsorbed on the surface of the fiber increases at a rate proportional to $\sqrt{t}$. Thus, the final absorption signal of the combined model is also increasing at a rate proportional to $\sqrt{t}$. A very important point to mention in this model is the assumption it makes on how the nanoparticles will be deposited on the surface of the fiber. As mentioned in the absorption model section, simulation was done on particles separated with distances greater than the diameter of one particle. This is not the actual case since the adsorption process in not controlled, and particles are adsorbed randomly on the surface following Random Sequential Adsorption (RSA) [109].

The effect of particle spacing is well understood from the literature [99]. A red shift in the peak absorption wavelength in the LSPR signal is expected as nanoparticles agglomerate. Additionally, the LSPR peak width is expected to broaden spanning multiple wavelengths. The reason is attributed to the fact that the closer the particles, the slower the plasma frequency becomes, as one particle becomes affected by the dipole of its neighboring particles and the particles start resonating as one larger non-spherical particle [99]. Moreover, the magnitude of the LSPR absorbance is also affected by the spacing. A lower quantity of particles with optimized distribution may result in a higher LSPR signal compared to a sensor with a higher quantity of particles with significant aggregation.

The above-mentioned effects of RSA, along with the effect of the monolayer on the adsorption rate, are not captured in this model. These effects will be highlighted and discussed further in Chapter 3.

2.3 Modeling FOEW LSPR refractive index sensor

In this section the FOEW LSPR sensor is modelled using COMSOL MULTIPHYSICS 6.1 and the performance of the sensor is investigated. COMSOL stands out as a robust finite element analysis software, particularly well-suited for simulating FOEW LSPR sensors. Its strength lies in its ability to concurrently model multiple physical phenomena, a critical requirement for comprehensively representing the intricate interactions within LSPR sensor systems. The Electromagnetic module in COMSOL is pivotal for simulating the complex behavior of the electromagnetic fields, facilitating the study of light-material interactions in the context of LSPR sensors [110–112].

Prior to simulating the FOEW LSPR sensor response, the materials' optical properties must be well defined. Although the software has an extensive material database, it is important to be as accurate as possible during any numerical simulation, especially if it involves multiple physics domains interacting with one another. The built-in material database will be used for the media under which the FOEW LSPR will operate only, such as air, or water.

As for the glass fiber optic (sensing region) and silver nanoparticles, there were no materials found in COMSOL built-in library that accurately reflected the optical properties of these materials. Consequently, these will be modelled and verified using MATLAB, then the variables will be used as input in COMSOL. This ensures that the modelled materials have optical properties that are as close to the actual optical properties for these materials as possible.

Finally, the sensor is modelled with different nanoparticle sizes in media with different refractive indices to determine the sensor's performance characteristics. Although it was

established in section 2.2.1 that nanoparticles with 30 nm size have the highest absorption, using 10 nm and 20 nm sizes results in higher surface density as stated in section 2.2.2. Thus, it is important to investigate the performance of the sensor using these sizes as well, to determine with high certainty which size is better suited for this sensor.

2.3.1 Modeling the sensing region optical properties

The sensing region of the sensor presented in this thesis comprises of a coreless fiber, which is pure silica fiber. The construction of the coreless fiber and reason for using it as a sensing region will be discussed in detail in Chapter 3. The Sellmeier equation is an empirical equation that describes the dispersion properties of an optical fiber [113].The equation relates the wavelength of light to the refractive index of the fiber, and takes the form of:

$$n^2(\lambda) = 1 + \sum_i a_i \left(\frac{\lambda^2}{\lambda^2 - b_i^2} \right) \tag{2.18}$$

Where $n(\lambda)$ is the refractive index of the fiber at a wavelength λ, a_i are constants specific to the fiber material (i.e. pure silica), and b_i are the wavelengths at which the refractive index is equal to the square root of the real part of the material's refractive index.

The Sellmeier equation is commonly used to model the dispersion properties of silica-based optical fibers. It is a simple and useful model to predict the refractive index of an optical fiber material. Table 2 below show the Sellmeier coefficients for pure silica based on experimental data [114], which is the sensing region in this work.

Table 2 – Sellmeier equation variables for pure silica [114]

Coefficients	a1	a2	a3	b1 (μm)	b2 (μm)	b3 (μm)
Pure silica (Core)	0.6961663	0.4079426	0.8974794	0.0684043	0.1162414	9.896161

Comparison between the refractive index of pure silica from the Sellmeier equation using the coefficients above and the refractive index provided by the supplier of the coreless fiber are presented in Figure 14.

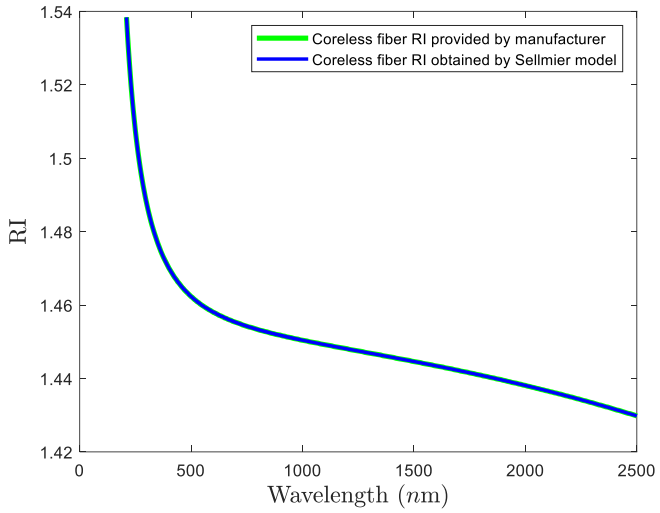


Figure 14 – comparison between refractive index of coreless fiber provided by the manufacturer against the results from the Sellmeier equation

The two graphs overlap across the wavelengths 200 nm to 2500 nm. This verifies the Sellmeier equation, and the parameters used in it. As a result, equation (2.18) and the parameters listed in Table 2 were used as an input in COMSOL to describe the dispersion properties of the sensing region as a function of the wavelength of light.

2.3.2 Modeling the silver nanoparticle optical properties

The frequency-dependent complex dielectric function of metal is described by the Drude-Lorentz model [32,99,115,116]:

$$\varepsilon(\omega) = \varepsilon_{r,\infty} + \sum_{k=0}^{K} \frac{f_k\, \omega_p^2}{\omega_k^2 - \omega^2 + j\omega\Gamma_k} \tag{2.19}$$

Where $\varepsilon_{r,\infty}$ is the real part of the dielectric constant and infinite frequencies, and ω_p is the plasma frequency. f_k, ω_k, Γ_k are the strength, the resonance frequency, and damping frequency of the kth oscillator, respectively. Table 3 below lists the values of the silver nanoparticle variables used in the Drude-Lorentz model. These values were determined by [116].

Table 3 – Values of the silver nanoparticle variables used in the Drude-Lorentz model [116]

Parameters	$\hbar\omega_p$	f_0	Γ_0	f_1	Γ_1	ω_1	f_2	Γ_2	ω_2
Value	9.01	0.845	0.048	0.065	3.886	0.816	0.124	0.452	4.481
Parameters	f_3	Γ_3	ω_3	f_4	Γ_4	ω_4	f_5	Γ_5	ω_5
Value	0.011	0.065	8.185	0.840	0.916	9.083	5.646	2.419	20.29

Where all parameters' units are in (eV) except for f which is unitless. The dielectric function is related to the refractive index of the material through Maxwell's relation [32]:

$$\tilde{n}(\omega) = \sqrt{\varepsilon(\omega)} \tag{2.20}$$

Where $\tilde{n}$ and ε are the complex refractive index and the complex dielectric constant of the material as a function of the incident light wavelength ω respectively. Since:

$$\tilde{n}(\omega) = n(\omega) + i\kappa(\omega) \tag{2.21}$$

$$\varepsilon(\omega) = \varepsilon_1(\omega) + i\varepsilon_2(\omega) \tag{2.22}$$

The results obtained from the model are plotted in Figure 15. Both dielectric constant and refractive index results obtained from the model are in agreement with the experimental values for silver particle [32,99] .

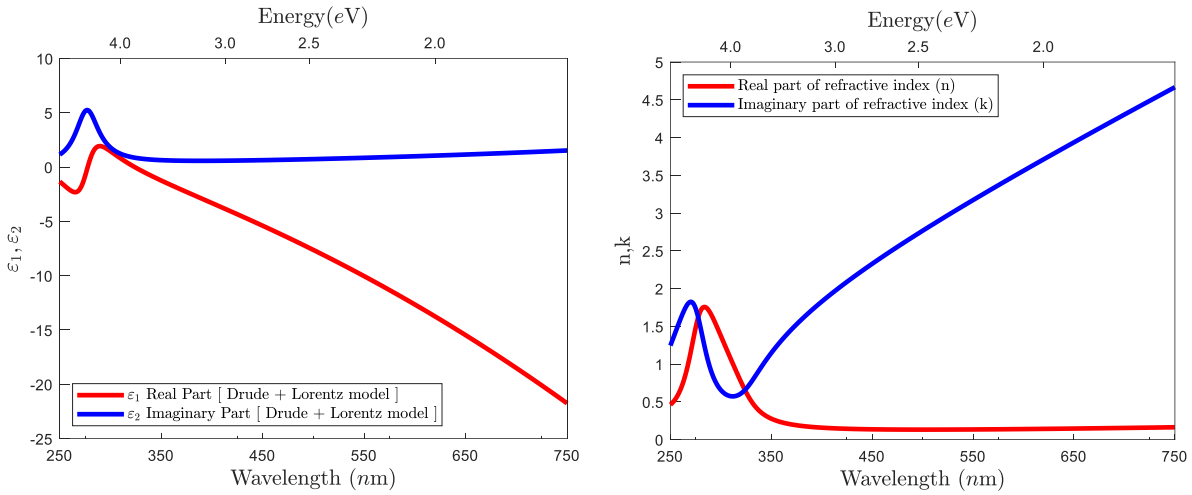


Figure 15 – (a) Silver dielectric constant (left) – (b) Silver refractive index (right)

This verifies the Drude-Lorentz model, and the parameters used in it. As a result, equations (2.19) – (2.26) and the parameters listed in Table 3 are used as an input in COMSOL to describe the optical properties of the silver nanoparticles as a function of the wavelength of light.

2.3.3 Modeling FOEW LSPR response and sensitivity

As mentioned in section 2.3, COMSOL is used to model the response of the final sensor and extract the sensor's performance characteristics. The COMSOL model consists of a 2D section of pure silica fiber with silver nanoparticles adsorbed on the outside surface of the fiber. The silver nanoparticles are covered in a region with a varying refractive index to study how the sensor performs in different media.

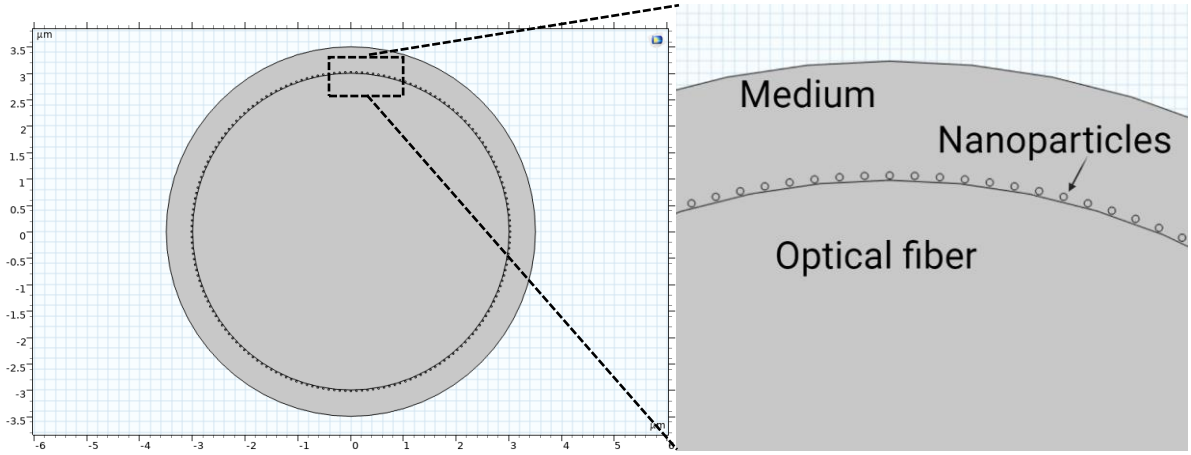


Figure 16 – FOEW LSPR Sensor model construction used in COMSOL simulations

Figure 16 shows the model constructed in COMSOL for the simulation of the FOEW LSPR sensor. The insert in this figure shows the surface of the optical fiber, covered with the simulated nanoparticles within a 250 μm thick medium, which is sufficient to accurately capture the LSPR effect. Since the LSPR response is expected to occur in the UV-VIS region, the mesh size for the model has to be a fraction of the minimum wavelength to produce reliable results [117]. Using the actual optical fiber diameter of 125 μm, which is the diameter of the fiber used in the experiments, and a maximum mesh size of 100 nm, the generated model

becomes very extensive and very time-consuming to solve. Thus, the model fiber size was minimized to reduce computational time and resources. For this study, the diameter of the optical fiber was set to 6 μm, which is one of the smallest radii that still allows for multi-modes to travel in the fiber and is calculated based on equation (2.14) for $V > 2.405$. The surface of the fiber was covered with 30 nm silver nanoparticles; however, the particles were separated with distances greater than the diameter of one particle to avoid any electromagnetic interference. With these constraints, the final number of nanoparticles covering the surface of the fiber was 180. Figure 17 shows the final mesh of the modelled sensor including all these considerations. The model was meshed automatically by COMSOL following a Physics-Controlled meshing with a maximum mesh size set to 100 nm as mentioned earlier. As it can be seen from the insert of Figure 17, the mesh was smaller than 100 nm in the interface region between the fiber and the nanoparticles, as well as the nanoparticles themselves.

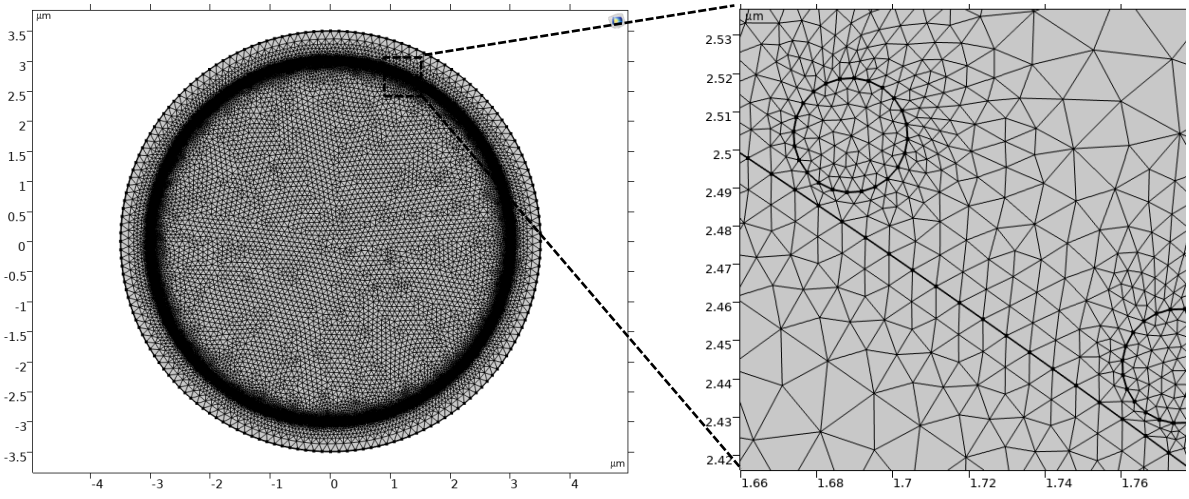


Figure 17 – FOEW LSPR Sensor model construction used in COMSOL showing the mesh size

The electromagnetic waves, frequency domain (EWFD) module was utilized, which solves the time-harmonic wave equation for the electric field. The sensor is based on LSPR phenomenon where the light modes travelling in the optical fiber core produce evanescent waves at the interface that interact with the silver nanoparticles, exciting the conduction band electrons and causing LSPR to occur absorbing the energy of the light. The material optical properties were set using the parameters and variables shown in Table 11 and Table 12 in Appendix A. Essentially, the models discussed in 2.3.1 and 2.3.2 were integrated in the final COMSOL model for the glass optical fiber and silver nanoparticles.

The imaginary part of the effective refractive index of the system is proportional to the core-mode losses which can be represented by the following equation [118]:

$$CL = \frac{40\pi}{ln(10)}\left(\frac{Im(n_{eff})}{\lambda}\right) \tag{2.23}$$

Where CL is the confinement loss and represents the loss of a core-guided mode in dB/m, which corelates directly with the absorption of the sensor, λ is the wavelength of light in m, and n_{eff} is the effective refractive index of the system. The loss of a core-guided mode occurs at the point of its phase matching with the LSPR [112]. Parametric sweep is used to change the operating wavelength from 300 nm to 500 nm in 10 nm steps, and the relation between the number of modes and the confinement loss is studied and the results are shown in Figure 18.

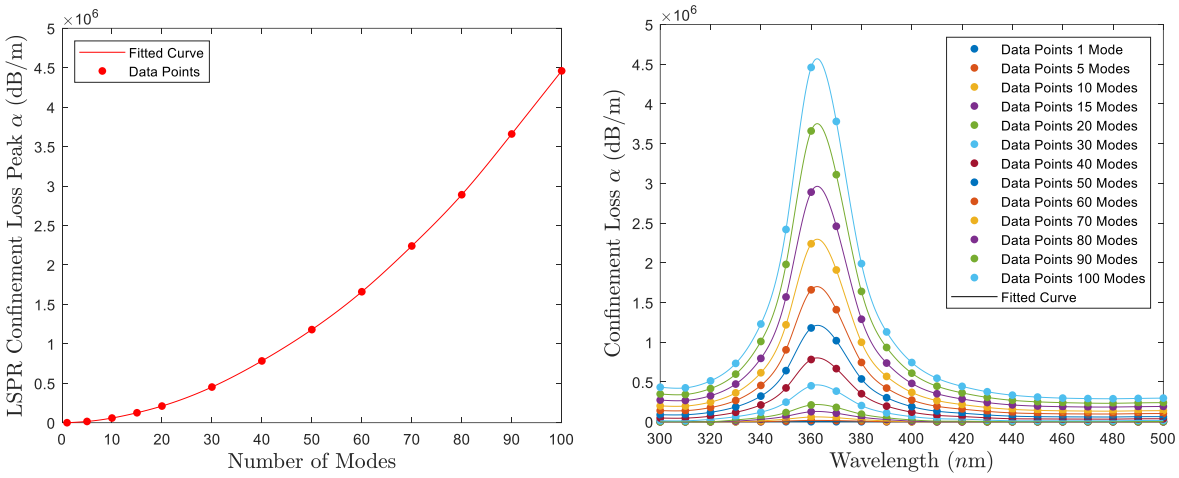


Figure 18 – (a) Confinement loss at 360 nm vs number of modes (left) – (b) Wavelength (right)

Figure 18 shows LSPR occurring at around 360 nm, which is expected for silver nanoparticles in air. The confinement loss due to LSPR increases exponentially as the total number of modes contributing to the signal increases, but the LSPR wavelength remains the same as shown in the figure. This could be due to how the lower order modes travel closer to the fiber core, and only a small fraction of their energy reaches and interacts with the nanoparticles. However, higher order modes travel closer to the surface as shown in Figure 19, and the energy of these modes reach and interact with the nanoparticles more efficiently.

Figure 19 (a) shows the fundamental mode traveling through the fiber, which has the highest electric field. The insert shows the electric field around the nanoparticles due to LSPR. Although significant in absolute value, compared to the mode electric field, it's almost $1/4^{th}$. Figure 19 (b) shows one of the higher order modes. In this mode, the magnitude of the LSPR electric field is almost 85% the magnitude of the mode's electric field. Which is due to that mode traveling closer to the surface of the fiber.

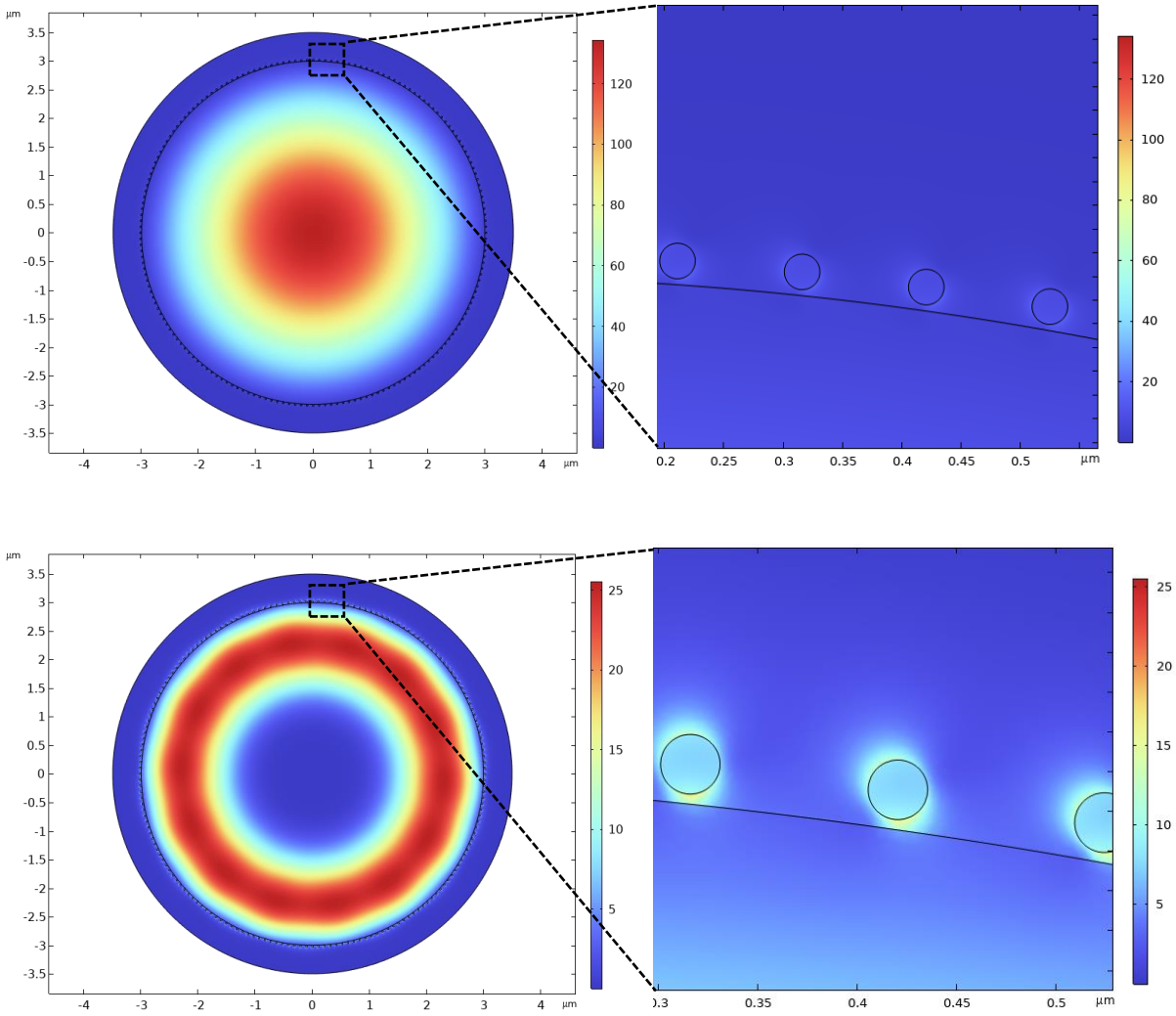


Figure 19 – (a) Fundamental mode (top) – (b) Higher order mode (bottom) – Wavelength 360 µm

Scale represents electric field norm (V/m)

As more modes are considered, a higher percentage of the total electric field of the modes traveling inside the fiber interacts with the nanoparticles, which increases the total confinement loss. Using equation (2.14) to determine the V number, the highest possible number of modes that can be guided through the model fiber occur when the medium

surrounding the fiber is air (i.e. refractive index of cladding = 1) and at light wavelength of 300 nm, which can be calculated from:

$$M \approx \frac{V^2}{2} \tag{2.24}$$

This results in approximately 4295 modes. This study will not investigate the effect of all 4295 modes as the results shown earlier from 100 modes can be considered comprehensive. However, it is important to note that the actual fiber that will be used experimentally in Chapter 3 will have approximately 938450 modes under the same conditions. Additionally, as the fiber diameter used experimentally is significantly larger, this will result in more nanoparticles being adsorbed on its surface. Nevertheless, although there is a significant difference in dimensions between the fiber used in the model and the fiber used in the experiments, the fact that both sensors have the same construction and are based on multi-mode fibers allows for the correlation of the findings regarding the modelled sensor characteristics with the experimental sensor characteristics.

2.3.4 Sensor performance results

The performance of any sensor is typically analyzed based on some essential parameters such as: sensitivity, limit of detection (LOD), sensor resolution, and signal-to-noise ratio (SNR). In LSPR based sensors, the shift in LSPR wavelength is directly related to the change in refractive index of the surrounding medium. If changing the refractive index of the medium RI_m by ΔRI_m causes a shift in the LSPR wavelength by $\Delta\lambda_{LSPR}$, then the sensitivity of the sensor can be written as [119]:

$$S = \frac{\Delta\lambda_{LSPR}}{\Delta RI_m} \tag{2.25}$$

The LOD is the limit at which the sensor can detect the lowest concentration of the analyte in a solution. It is affected by the noise of the entire system and the sensitivity of the sensor. To quantify the noise, the sensor is allowed to reach steady state multiple times when no analyte is present in the solution, and the standard deviation (σ) of the reference signal is measured. σ highly depends on the spectral resolution of the spectrometer. The minimum detectable sensor signal is then defined as 3σ . The LOD can be expressed as [119]:

$$LOD = \frac{3\sigma}{S} \tag{2.26}$$

A sensor with very high sensitivity and small standard deviation will result in a smaller LOD which is preferred. Like the LOD, there is the limit of quantification (LOQ), which is the limit at which we can correlate the signal to the analyte quantity. The LOQ uses the same equation as the LOD, but instead of 3σ its10σ divided by the sensitivity. The resolution of an LSPR sensor can be defined as the minimum change that can be detected.

Three sensors were modeled with different nanoparticle sizes. 10, 20, and 30 nm silver nanoparticles were used to study the sensor's refractive index sensitivity versus nanoparticle size and surface density. Based on conclusion drawn from sections 2.2.1 and 2.2.2, larger nanoparticle sizes have lower absorption efficiencies and result in less nanoparticles surface density when adsorbed on the sensing region. Thus, they were not considered.

Initially, the three sensors modeled with different sizes had 180 nanoparticles each, similar to the procedure explained in section 3.2 and 3.3, and only 30 modes were considered in this study to minimize computation time. This allows for the analysis of the refractive index sensitivity of the sensor based on the effect of the nanoparticle size only. The sensitivity was modelled by changing refractive index unit (RIU) of the medium and measuring the corresponding LSPR wavelength.

Since the simulated electromagnetic wave inside the fiber increases in 10 nm steps in the UV–VIS region from 350 nm to 750 nm, the (RIU) was set to 1.00 increasing in increments of 0.05 up to 1.3. This change in (RIU) is significantly higher than what is expected from an analyte-ligand interaction. However, this was done to mitigate the possibility of LSPR occurring in the same wavelength during modeling smaller changes in (RIU) due to the discreet steps in electromagnetic field wavelength. Thus, this approach allows for a better interpretation of the results provided by the model. The confinement loss versus wavelength was calculated for each sensor at each refractive index and the results are plotted in Figure 20 below.

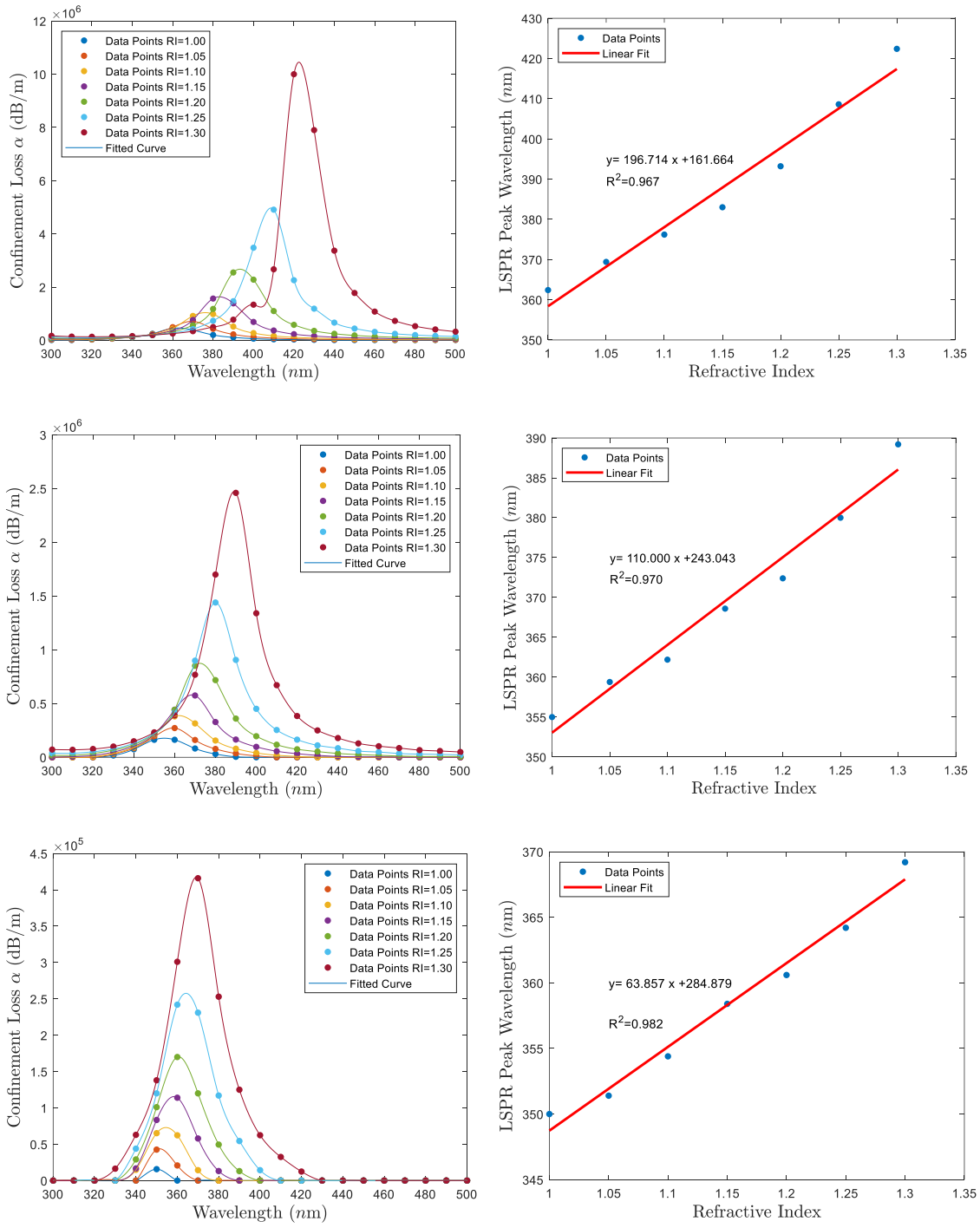


Figure 20 – Modelling results for varying refractive indices – 30 Modes – 180 particles – (a) 30 nm (top) – (b) 20 nm (middle) – (c) 10 nm (bottom)

Figure 20 demonstrates that LSPR wavelength experiences a redshift when the refractive index of the medium increases. This is due to the higher refractive index increasing the dielectric function of the medium and its polarization. This causes a higher attenuation in the LSPR, reducing the frequency which translates into a longer wavelength. Figure 20 (a) shows a sensitivity of 196.714 (nm/RIU) for sensors fabricated using 30 nm nanoparticles, versus 110.0 (nm/RIU) for sensors fabricated using 20 nm nanoparticles, and only 63.857 (nm/RIU) for sensors fabricated using 10 nm nanoparticles as shown in Figure 20 (b and c).

Additionally, the confinement loss increases with nanoparticle size. This can be attributed to the fact a 30 nm nanoparticle has a higher absorption efficiency as stated earlier in section 2.2.1. Since this specific size absorbs evanescent field more efficiently from the fiber, then any slight changes in the refractive index of the medium translates more efficiently into the signal, which results in a higher sensitivity. Another reason could be attributed to the Electromagnetic Field Decay Length, which also shows how this specific size has a higher sensitivity to changes in the medium's refractive index and has a longer electromagnetic field which interacts more efficiently with the evanescent field as well. The Electromagnetic Field Decay Length will be discussed in detail in the next section.

Despite these results, and as mentioned in section 2.2.2, one can argue that utilizing 10 or 20 nm silver nanoparticles would result in a higher surface density which could translate into a higher sensitivity. For this reason, the density of the nanoparticles was increased for those 2 sizes to 240 particles for the 20 nm size and 360 nm for the 10 nm size. These numbers were chosen to maintain a distance of $(2.5\ D)$ around each particle similar to the one found in

the 30 nm sensor configuration based on 180 particles, to avoid any interference. The results are shown in Figure 21 below.

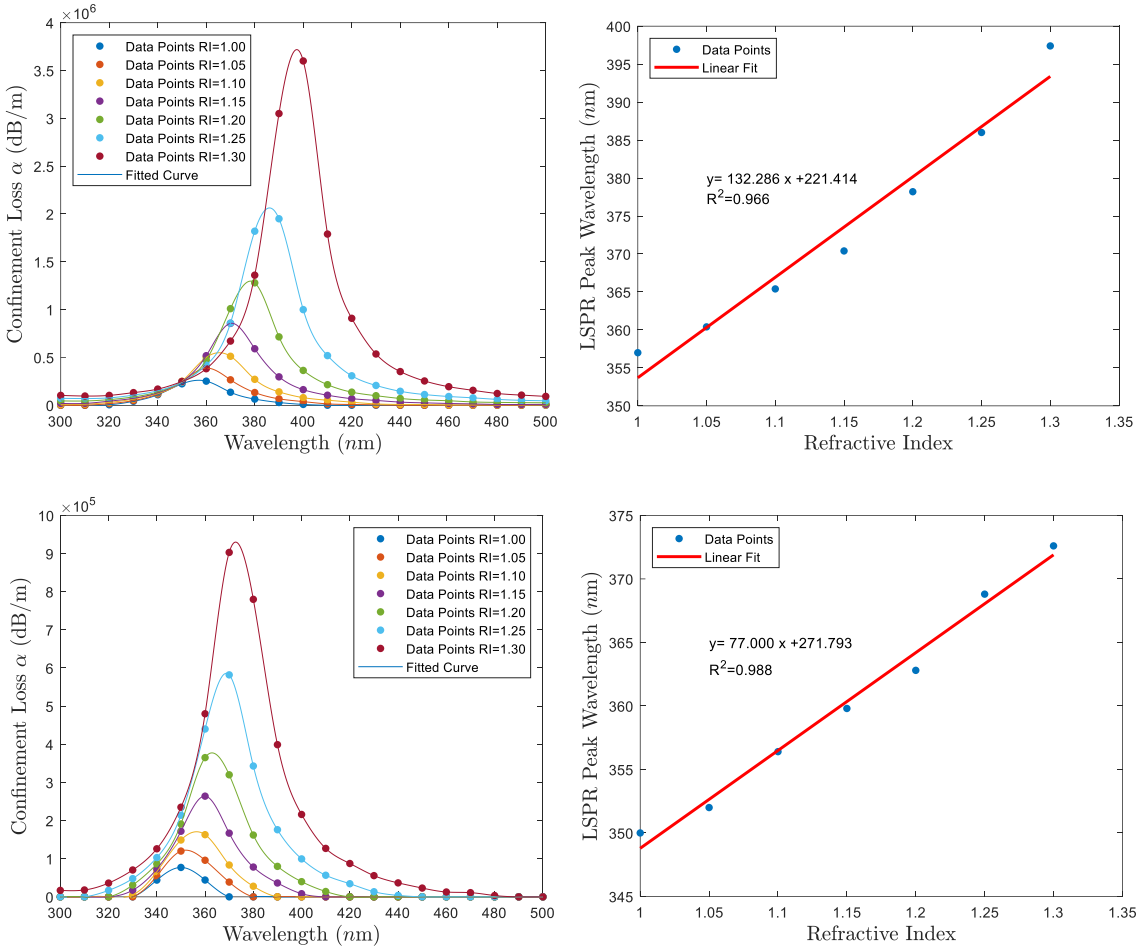


Figure 21 – Modelling results for varying refractive indices – 30 Modes – (a) 240 particles 20 nm (top) – (b) 360 particles 10 nm (bottom)

The results in Figure 21 indicate that increasing surface density on the sensing region, as shown in the 20 nm and 10 nm-based sensors, does indeed increase the sensitivity of the sensor, resulting in a higher wavelength shift in the same media compared to the same sensors with less surface densities. In the case of the 20 nm-based sensor, Figure 21 (a) shows that a 33.33% increase in number of nanoparticles resulted in a 20.26% increase in the sensitivity.

While in the case of the 10 nm-based sensor, a 100% increase in the number of nanoparticles resulted in a 20.58% increase in the sensitivity as shown in Figure 21 (b).

The increase of the sensitivity due to increase in nanoparticles density was expected based on the relation between the light absorption efficiency and number of nanoparticles presented in section 2.2.1. However, the sensor modeled with 30 nm nanoparticles was still significantly more sensitive. This suggests that when most of the sensing region is covered with nanoparticles, the effect of the nanoparticle size will contribute significantly more towards the sensor's sensitivity compared to the surface density.

There could be a point during the nanoparticle adsorption process, and before the complete coverage of the sensing region, where sensors fabricated with 10 or 20 nm would have a higher sensitivity relatively when compared with sensors fabricated with 30 nm (i.e. after 5 minutes of adsorption), however, these sensors would have a very low sensitivity. If adsorption is allowed to continue until the sensing region is fully covered, the 30 nm-based sensor would always have the highest sensitivity. Table 4 below shows a summary of the model results.

Table 4 – Summary of FOEW LSPR model results

Nanoparticle size (nm)	10		20		30
Number of particles	180	360	180	240	180
Sensitivity (nm/RIU)	63.857	77.000	110.000	132.286	196.714

2.4 Modeling the Electromagnetic Field Decay Length

The model presented in 2.3.3 illustrates the concept of the FOEW LSPR sensor that is used in this research and provides a great insight on how the sensor responds to changes in the refractive index of the medium. However, a very important parameter that plays a key role in biosensors is the electromagnetic field decay length [28]. As mentioned in section 1.3, the plasmon oscillates with an electromagnetic field that decays exponentially with distance from the nanoparticles surface. The size of this electromagnetic field is what determines the sensing area around the nanoparticle.

In the previous model, there was no requirement to account for the electromagnetic field decay length, as changing the medium's refractive index would affect the electromagnetic field around the nanoparticle, based on how the model is structured. This is not the case for biosensors. For the nanoparticle to sense any changes in the local refractive index due to the ligand conjugation and the ligand-analyte interaction, these changes must happen inside the electromagnetic field surrounding the nanoparticle. This means that the electromagnetic field length must be investigated, and if possible, optimized for the target ligand and analyte.

If the electromagnetic field around the nanoparticle is significantly smaller than the ligand, or significantly larger than the analyte, this would result in a weak signal. The optimum electromagnetic field must be comparable to the ligand-analyte complex [28]. This concept is illustrated in Figure 22.

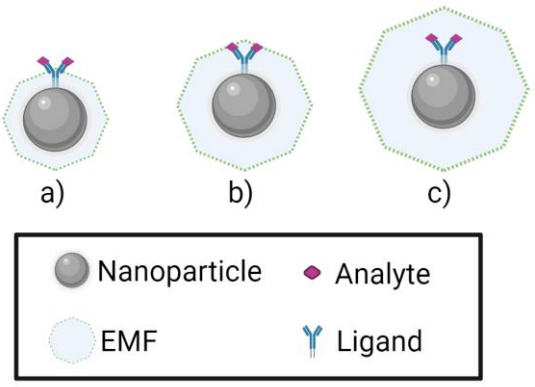


Figure 22 – a) Small electromagnetic field - b) Optimum electromagnetic field - c) large electromagnetic field – Created with BioRender.com

The electromagnetic field decay length (l_d) is directly related to the sensitivity of the nanoparticle through the following equation [31]:

$$\Delta\lambda_{LSPR} = m_{np}\,(\Delta n_a)\left[1 - \exp\left(\frac{-d_a}{l_d}\right)\right] \tag{2.27}$$

Where $\Delta\lambda_{lspr}$ is the shift of LSPR wavelength, m_{np} is the refractive index sensitivity, Δn_a is the change in refractive index of the analyte relative to the solution, d_a is the effective adsorbate layer thickness. To determine l_d for the 3 nanoparticle sizes investigated in 2.3.3, the water shell method is used, which was adopted from [28]. In this method, the nanoparticle is modeled with a shell of water around it. The thickness of this shell starts at 5 nm and increases in steps of 5 nm until a final thickness of 50 nm. The concept behind this method is simple, at small thicknesses, the electromagnetic field would be partially interacting with water (refractive index = 1.33) while the rest of it extends beyond the water shell and interacts with vacuum (refractive index = 1). As the water shell increases in thickness, the LSPR peak would shift since the portion of the electromagnetic field interacting with water would increase, and

the portion interacting with vacuum would decrease. The sensitivity and the electromagnetic decay length are found by measuring the LSPR peak shift at each water shell thickness, then using non-linear least squares regression with EXCEL to solve the following:

$$R_i = X\left[1 - exp\left(\frac{-d_i}{Y}\right)\right] \tag{2.28}$$

Where R_i is the difference between LSPR wavelength at water shell thickness d_i and LSPR wavelength in vacuum. The variables X and Y are optimized through the least squares method until the error is below the threshold. The value of X would represent the sensitivity m multiplied by Δn (which is equal to 0.34), while Y would denote the electromagnetic decay length. ANSYS LUMERICAL is used for the modeling and the model is constructed in a similar way to 2.2.1 except for the water shell. The model construction is shown in Figure 23.

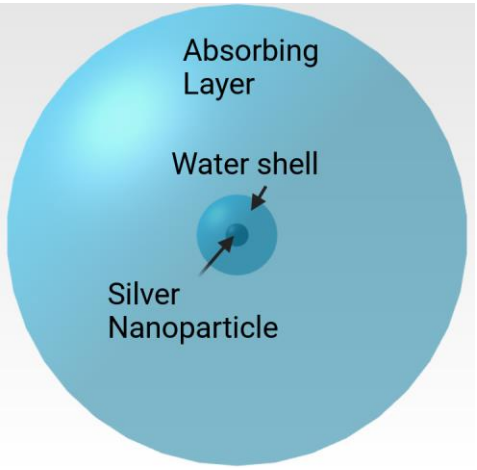


Figure 23 – ANSYS LUMERICAL model construction for water shell method

Modeling the electromagnetic field decay was performed on the three silver nanoparticle sizes (10 nm, 20 nm, and 30 nm). The results are shown in Figure 24.

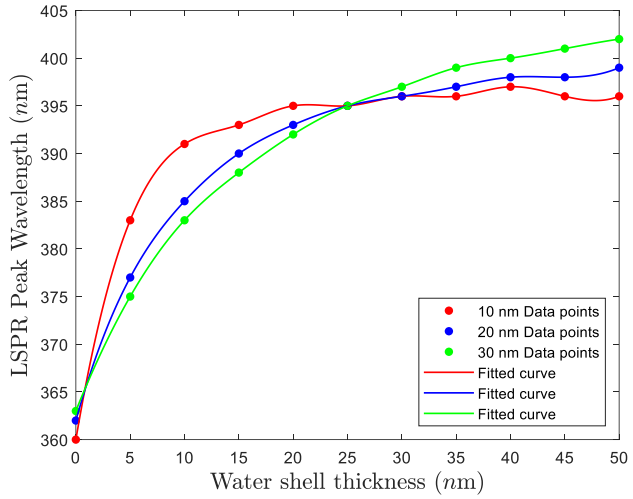


Figure 24 – Water shell thickness vs LSPR peak for 10 nm, 20 nm, and 30 nm silver nanoparticles

Figure 24 demonstrates the shift in the LSPR wavelength for each nanoparticle size as the thickness of the water shell is increasing which is a result of the electromagnetic field interacting partially with 2 media with different refractive indices as explained earlier. The initial LSPR wavelength was highest for the 30 nm nanoparticle, followed by the 20 nm nanoparticle and the 10 nm nanoparticle respectively which is expected. As the water shell thickness increases, more of the electromagnetic field is interacting with the higher refractive index medium, causing LSPR wavelength to increase for all three nanoparticle sizes. However, the rate of change of LSPR wavelength vs water shell thickness below the 25 nm thickness point is highest for 10 nm nanoparticle, followed by the 20 nm nanoparticle and the 30 nm nanoparticle, respectively. At a water shell thickness of 25 nm, all three nanoparticle sizes have the same LSPR wavelength. Beyond the 25 nm thickness, the rate of change of LSPR wavelength vs water shell thickness favors the larger nanoparticle size. The interpretation of this behavior suggests that the 10 nm nanoparticle has the smallest electromagnetic field length, while the 30 nm nanoparticle has the largest.

The non-linear least squares regression method solving equation (2.28) was performed for the three nanoparticle sizes and the results are shown in Table 5. From these results, we can conclude that the 30 nm nanoparticle has the highest sensitivity, which agrees with the conclusions of the models presented in sections 2.2.1 and 2.3.4, and is attribute to the higher absorption efficiency of this size relatively. As for the electromagnetic field length, the results show that this field expands a distance approximately equals to the radius of the nanoparticle.

Table 5 – Non-linear least squares regression results

Size	10 (nm)	20 (nm)	30(nm)
X	35.926	38.170	39.841
$Y\ (nm)$	5.072	9.424	14.973
$m\ (nm/RIU)$	108.866	115.667	120.732

The dimensions of the ligand (i.e. cortisol IgG antibody) used in this work are taken from [120–124] and shown in Figure 25.

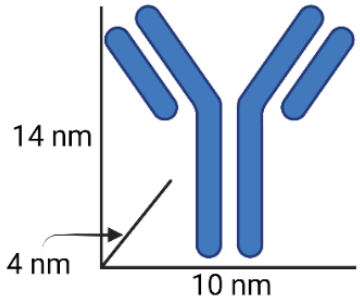


Figure 25 – Dimensions of IgG antibody from literature – Created with BioRender.com

Based on the orientation at which the antibody conjugates on the nanoparticle surface, which is random but can be controlled via the PH level of the coupling buffer [125] amongst

other factors [126], the height of the IgG antibody is 14 nm. Accordingly, the 30 nm nanoparticle has the most optimum electromagnetic field length for this type of biomolecule.

2.5 Modeling the Analyte-Ligand Reaction Kinetics and final sensor response

The Langmuir adsorption isotherm is the basis of kinetic analysis of ligand-analyte interactions in any biosensor [127]: This adsorption by chemisorption expression assumes all ligand reaction sites are covered by the analyte. A molar concentration of analyte $[A]$ interacts with a molar concentration of ligand $[L]$ forming a molar concentration of analyte-ligand complex $[AL]$ based on the following expression [128]:

$$[A] + [L] \underset{k_{off}}{\overset{k_{on}}{\rightleftharpoons}} [AL] \tag{2.29}$$

k_{on} is the association rate with units $M^{-1}s^{-1}$. It describes the rate of the forward reaction taking place between an analyte and ligand to form the complex. This rate is dependent on the concentration of analytes and ligands. On the contrary, k_{off} is the dissociation rate, and it describes the rate of the backward reaction where the complex dissociates into separate analytes and ligands. k_{off} has units of s^{-1}, and is independent of concentrations of the analytes and ligands of the system.

This is an equilibrium reversible reaction. The dissociation constant K_d represents the concentration of analyte at which half the binding cites on the ligand are occupied at equilibrium [129]. K_d can be expressed as follows:

$$K_d = \frac{k_{off}}{k_{on}} = \frac{[A][L]}{[AL]} = \frac{1}{K_a} \tag{2.30}$$

Where K_a is the association constant. The sensor response can be determined by θ, which is the fraction of ligand binding sites occupied by the analyte $[AL]$ to the total available binding sits $[L]_t$. θ can be expressed as a function of the analyte concentration and the dissociation constant of this interaction:

$$\theta = \frac{R}{R_{max}} = \frac{[AL]}{L + [AL]} = \frac{[A]}{K_d + [A]} \tag{2.31}$$

Where R is the response of the sensor. The maximum response R_{max} occurs at $\theta = 1$. R_{max} and K_d can found by generating a plot of R (at equilibrium) versus $[A]$, and fitting to an isotherm. The Langmuir adsorption isotherm is used in modeling the kinetics reaction and the sensor response in sections 2.5.1 and 2.5.2.

2.5.1 Cortisol-Antibody reaction kinetics model

COMSOL was used to construct the kinetics reaction model of cortisol to the antibodies. The model was designed to reflect a FOEW LSPR sensor placed inside a microchannel with dimensions that represent the actual microchannel that will be used during testing. The model is shown in Figure 26 .

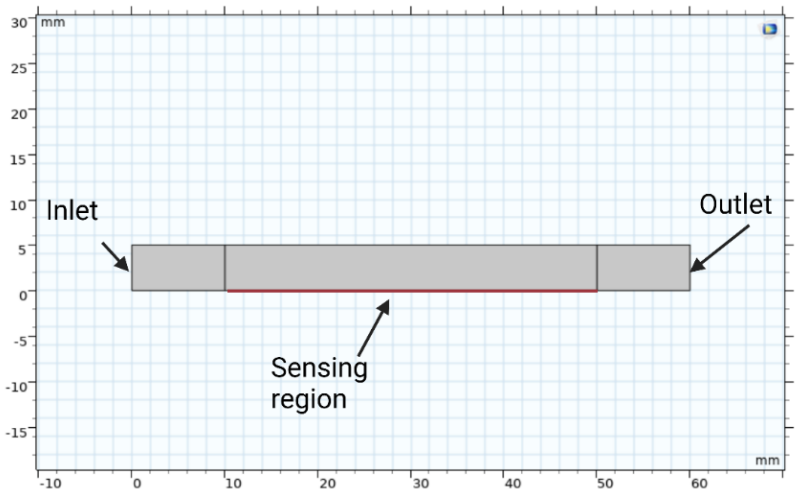


Figure 26 – Microchannel model construction in COMSOL – analyte-ligand interaction model

The height of the channel was changed to 5 mm in Figure 26 for the purpose of clearly showing the construction, however, the actual height used in the modeling and during testing is 0.5 mm. The length of the sensing region was set to 4 cm, which is the length of the sensing region used in the experiments in Chapter 4.

This model utilizes three built-in modules in COMSOL to solve for the analyte - ligand interactions. The first module is the laminar flow model, which solves for the fluid flow inside the channel based on the medium's properties and velocity using Navier-Stokes equations. The second module is the transport of diluted species, which solves for the diffusion of the analyte diluted in the flow based on the analyte concentration using the diffusion-convection equations, and finally the surface reaction module, which solves for the reaction between the diluted species and the sensing region based on predetermined interaction parameters using the surface molar flux equations. This model is similar to work reported in literature [130].

The parameters set for the medium were that of water. This is an approximation as the medium will be Phosphate Buffer Saline. The velocity of the flow was set to 1 mm/s. The antibody surface density, placed on the sensing region in the model, was set to 2.46×10^{-8} mol/m^2. This is found to be within the theoretical range of a monolayer density of antibodies conjugated through self-assembly [123]. Considering how each IgG antibody has 2 available sites for analyte binding, the value was multiplied by 2. Finally, the diffusion constant for cortisol was not found in the literature, but a common value for many analytes is $1x10^{-11}$ m^2/s [130]. The remaining cortisol-antibody kinetics parameters were extracted from literature of SPR cortisol sensors [131] . All the parameters used in the model are reflected in Table 6.

Table 6 – Parameters used in the cortisol-antibody reaction kinetics model

Variable	Description	Value	Units
D_c	Diffusion coefficient of Cortisol	1.0×10^{-11}	m^2/s
γ_{ac}	Anti-Cortisol surface density	$2 \times 2.46 \times 10^{-8}$	mol/m^2
k_{on}	Association rate	$1.3\ (\pm 0.4) \times 10^6$	$M^{-1}.s^{-1}$
k_{off}	Dissociation rate	0.7	s^{-1}
v	Fluid velocity	1×10^{-3}	m/s
L	Sensing region length	4	cm
δ	Channel height	0.5	mm

The model was run to simulate the flow passing over the sensing region for 30 minutes by using a time dependent study based on the three modules mentioned earlier. The salivary cortisol range is reported as ~ 0.25 – 25 nM [132]. Thus, the cortisol concentrations assessed were 0.001, 0.01, 0.1, 1, 5, 10, 50, 100, 200, 500, 1000, and 10000 nM. This tests the upper

and lower limits of the sensor, while including the salivary cortisol range. The modeling results are shown in Figure 27.

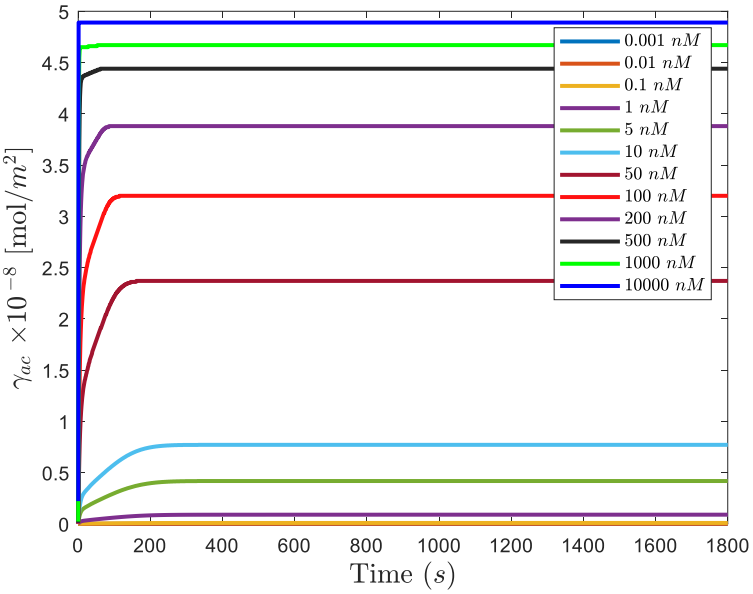


Figure 27 – COMSOL results for the cortisol – antibody interaction kinetics

The results displayed in Figure 27 suggest that the interaction occur in less than 5 minutes, which is significantly quicker compared to other biological molecules, and is logical due to the extremely small size of the cortisol molecule (362.46 g/mol) compared to the average molecule size of proteins (~50,000 g/mol).

Figure 28 presents the final anti-cortisol surface density after each cortisol concentration. The small change in the results of 1000 nM compared to 10000 nM indicates the saturation of available binding sites. Figure 28 (a) shows how the occupation of available binding sites increases with concentration, while Figure 28 (b) shows the results in terms of the percentage of ligand occupied binding sites θ, plotted on a logarithmic scale.

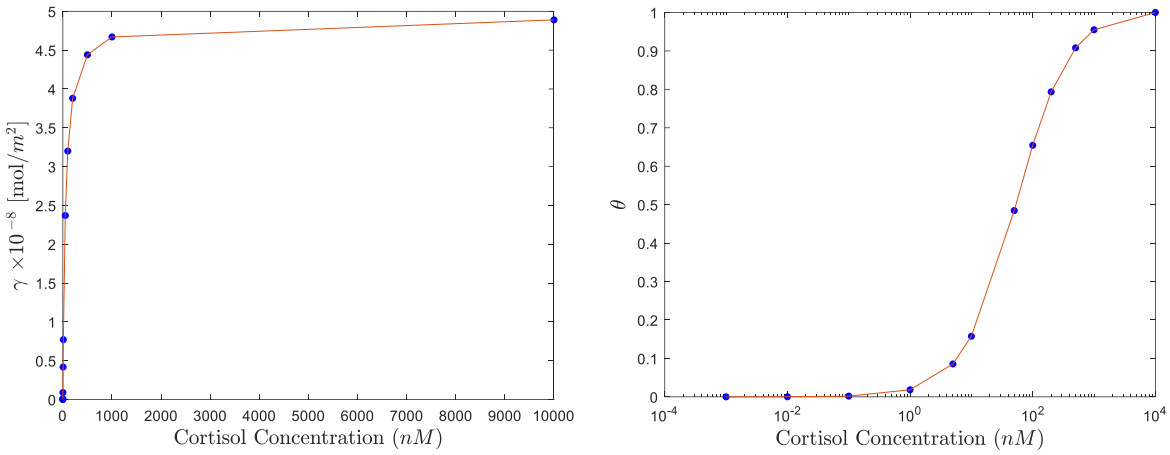


Figure 28 – Final analyte-ligand model results showing: (a) antibody occupied sites (left) – (b) fraction of occupied sites (right) – vs cortisol concentration

2.5.2 Sensor response model

The final response of the sensor was modeled based on the results obtained from the FOEW LSPR sensitivity model in section 2.3.3 and analyte-ligand interaction model in section 2.5.1. This is achieved by using the de Feijter's equation below [133]:

$$n_a = n_m + \frac{n_i \, \gamma_{ac} \, M_a}{d_a} \tag{2.32}$$

The de Feijter's equation is utilized to find the final refractive index of the analyte n_a as a function of the refractive index of the medium n_m, the refractive index increase of the analyte n_i, the density of the bound analyte γ_{ac}, the molecular mass of the analyte M_a, and the thickness of the analyte layer d_a. A refractive index of 1.34 was used for the medium n_m, which is the refractive index of water. The values of n_i and d_a used were $1.8 \times 10^{-7}\ m^3/g$ and $4 \times 10^{-9}\ m$ respectively, which are the typical values reported for many proteins in the literature [133]. The final anti-cortisol surface density results obtained from COMSOL were used for γ_{ac}, and the cortisol molecular mass is 362.46 g/mol.

Table 7 lists all the parameters used in the de Feijter's equation.

Table 7 – de Feijter's equation parameters

Variable	Description	Value	Units
RI_a	Refractive index increments of analyte	1.8×10^{-7}	m^3/g
M_a	Molecular mass of cortisol	362.46	g/mol
d_a	Thickness of the cortisol layer	4×10^{-9}	m
γ_{ac}	Anti-Cortisol surface density	$2 \times 2.46 \times 10^{-8}$	mol/m^2

Using the refractive index sensitivity for the 30 nm based FOEW LSPR sensor generated by the model, the final sensor response was modeled on MATLAB and results are presented in Figure 29.

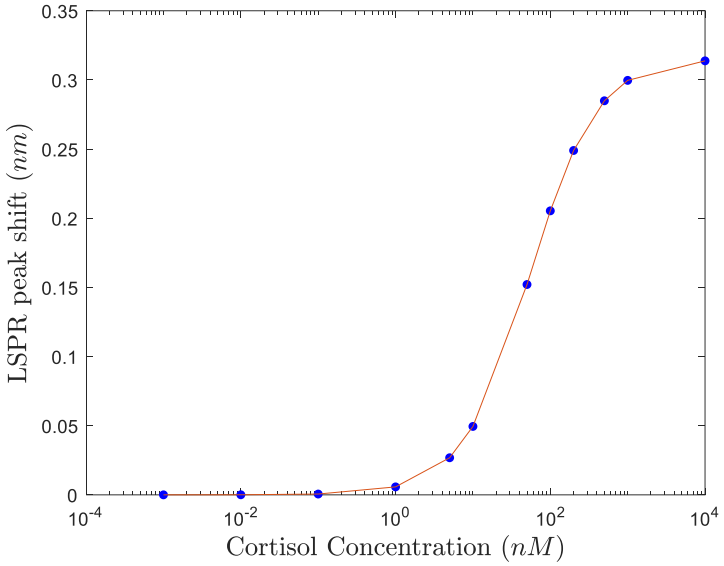


Figure 29 – Final sensor response model based on COMSOL modelling results combined with de Feijter's equation

The results of the sensor response model display a very small change in the LSPR peak shift due to the small change in final refractive index. The signal shift corresponding to cortisol

concentrations change from 1-500 nM was less than 0.3 nm, while the total shift for the highest concentration of 10000 nM was almost 0.32 nm . Although this is less than the experimental noise level, which was found to be ~0.015 nm shift in wavelength over a 30-minute period, the results suggest a poor performance of the sensor. The minor change in the refractive index due to analyte binding is expected since the cortisol molecule is extremely small in size. Evidently, the sensor will only work if the actual sensitivity is significantly higher than the sensitivity of the FOEW LSPR COMSOL model. This is investigated experimentally in the next chapter.

Based on all the results obtained from the modeling in this chapter, using 30 nm silver nanoparticles in the fabrication of the FOEW LSPR sensor will provide the best performance characteristics. 30 nm nanoparticles have the highest absorption efficiency, result in a high final surface density, have the highest refractive index sensitivity, and an optimum electromagnetic decay length for sensing ligand-analyte interactions.

Chapter 3
Model Verification: Experimental Procedures

Chapter 3 presents the experimental design and procedures performed to fabricate FOEW LSPR sensors using different silver nanoparticles sizes. Characterization equipment such as Scanning Electron Microscopy (SEM), Atomic Force Microscopy (AFM), and UV-VIS spectroscopy are used to characterize the sensing region and the absorption results. The experimental results are verified against the main findings of the models in Chapter 2.

3.1 Materials

Ocean Optics HL-2000-LL Light Source with a wavelength range from 360nm – 2.4μm, Ocean Optics USB 4000 spectrometer with response range from 200nm – 1.1μm, connected to a computer with Spectra suite software. The spectrometer has an optical resolution of 0.1 – 10nm. Standard optical fiber (FG105LCA Ø125 μm Cladding diameter with Ø105 Core Glass Clad Silica Multimode Optical Fiber, 0.22 NA) and coreless termination fiber (FG125LA - Coreless Termination Fiber, Ø125 μm Glass Rod) were purchased from THORLABS. 10 nm, 20 nm, 30 nm, and 80 nm citrate capped silver nanoparticles colloidal solutions (20 PPM) were purchased from CYTODIAGNOSTICS®. Finally, APTES (3-Aminopropyl)-tri-ethoxy-silane) was purchased from Sigma-Aldrich.

3.2 FOEW LSPR Sensor Fabrication

The modeling results in Chapter 2 demonstrated key points that are verified experimentally in this section. The first is that a 30 nm nanoparticle has the highest LSPR absorption efficiency compared to any other nanoparticle size. The second is the positive

correlation between the number of nanoparticles and the total light absorbed. The third is that smaller nanoparticles result in higher surface density on the sensing region during adsorption process. The fourth and final point is that sensors fabricated with 30 nm nanoparticles are the most sensitive to changes in refractive index compared to sensors fabricated with 10 nm and 20 nm nanoparticles, despite the increase in the smaller nanoparticles' surface density. As mentioned in section 2.2 and 2.3, 10 nm, 20 nm, 30 nm and 80 nm silver nanoparticles were procured to study the absorption efficiency, adsorption kinetics, and final sensor refractive index sensitivity. All sizes had a concentration of 20 PPM.

3.2.1 Sensing region creation

The fabrication of a fiber optic evanescent field sensor requires removing the cladding to expose the core and allow the evanescent field to interact with the medium. This could be achieved through various methods such as the ones mentioned in Chapter 1. Most of these methods are time consuming, require the use of toxic and dangerous reagents, and are extremely sensitive to external factor, such as temperature and humidity, which significantly impacts the repeatability of the fabrication process [51,54–56].

In this work, a coreless fiber is fused to a standard fiber and used as the sensing region. A coreless fiber consists of a pure silica cladding with no core as shown in Figure 30. Using a coreless fiber as the sensing region is extremely time efficient, does not require the use of any chemicals, is not affected by environmental conditions, and is 100% repeatable. To the best of our knowledge, a coreless fiber FOEW LSPR biosensor has not been used in the literature thus far.

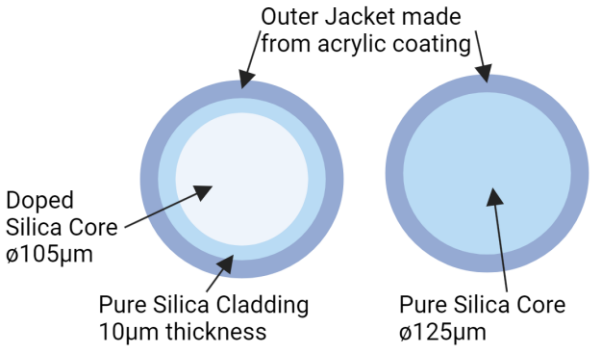


Figure 30 – (a) Cross sections of standard fiber (left) – (b) coreless fiber (right) – Created with BioRender.com

The outer jackets of the coreless fiber and the standard fiber consist of an acrylic coating that is manually stripped. Then, 4 cm of the coreless fiber is spliced from both ends to a standard optical fiber using a fusion splicer (AI-9 Fusion Splicer by Vikye) as shown in Figure 31.



Figure 31 – Optical fiber fusion splicer upon a successful splice

The length of 4 cm was found to allow nearly complete light absorption in the case of 30 nm-based sensors and is similar to FOEW LSPR sensors used in the literature and referred to in Table 1. The whole process of preparing a FOEW sensor using this method takes approximately 10 minutes.

3.2.2 Sensing region functionalization and salinization

The adsorption of nanoparticles on the sensing region is facilitated through the functionalization of the fiber's surface by a process called salinization. Salinization generates a SAM of a polyelectrolyte on the surface of the sensing region. Based on a study found in the literature, pre-treating a glass substrate in an Ultra Violet Ozone machine for 10 minutes prior to the salinization process allows for the production of high-quality SAMs with excellent tribological performances [134].

The study found that 10 minutes of pre-treatment provided the lowest surface roughness while significantly improving the hydrophilicity of the glass, which is attribute to the increase in Hydroxyl groups (OH-) [135,136]. These groups are naturally found on the surface of glass but can be further increased via the process of hydroxylation from the UVO treatment as shown in Figure 32.

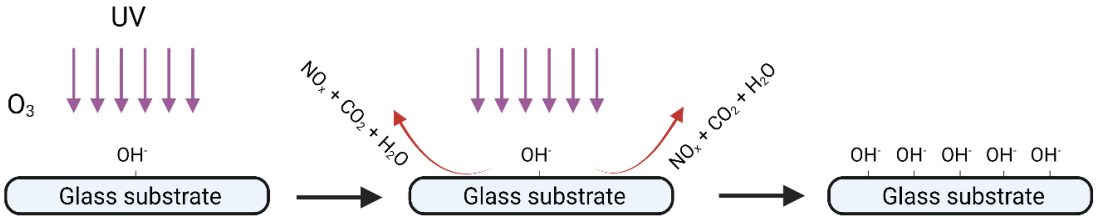


Figure 32 – Hydroxylation process using UVO treatment on a glass substrate – Created with BioRender.com

UVO has been used effectively on different materials to remove surface impurities and contaminants, and achieve a surface cleanness level that is near-atomic, in vacuum or air systems at ambient temperatures [134,137]. Compared to conventional hydroxylation methods, which use piranha solution to clean the substrates surface and increase the hydroxyl groups

[138], UVO generates no waste and little amounts of harmful gases (O_3), which are usually captured in the UVO generator.

Salinization of the sensing region is then done by preparing APTES solution in DI water and allowing it to hydrolyse. This breaks the saline groups via a process known as hydrolyzation. The sensing region is then dipped in the APTES solution for some time. The saline groups attack the hydroxyl groups on the glass surface and create a covalent bond through the salinization process and provide amine groups (NH_2) on the other end. Schematic showing the salinization process is shown in Figure 33.

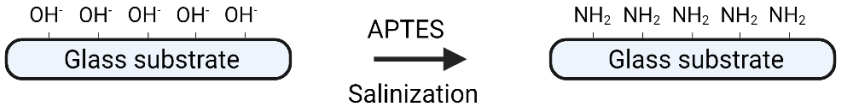


Figure 33 – Salinization of a glass substrate – Created with BioRender.com

As mentioned in section 01.5.1, different factors affect the APTES SAMs. Using high APTES concentrations (>10%) would result in poor quality SAMs with high surface roughness. However, it was reported that well-formed films with low RMS roughness, and insignificant sensitivity to temperature, can be achieved using low APTES concentrations (~1%) and with time-limited reactions (<1 hour) [66,67,139]. In this thesis, the salinization of the optical fiber with respect to the coating time was examined for 15, 30, 45, and 60 minutes. The results were very comparable and there was no conceivable difference to the nanoparticles adsorption rate or final surface density. Thus, the salinization for all the sensors in this work was done using 1% APTES solutions for a total coating time of 30 minutes.

3.2.3 Coating apparatus

The decision to use the optical fiber splicer to create the sensing region in the sensor presented in this thesis introduces some challenges to the overall fabrication of the biosensor. In the literature, the sensing region would usually be dipped in the APTES solution to perform the salinization process. However, unlike the configurations found in the literature where the sensing region used is made of plastic [77,82–89], or located towards the end of the fiber with a micromirror and a fiber coupler [90,91], our sensing region is made of silica and located towards the middle of the overall fiber. Which makes it problematic to dip the sensing region in a container with the APTES solution. Using the splicer introduces stress points where the sensing region and the standard fiber are fused. Bending the fiber to insert it in a container would frequently result in breaking it at the splice points.

This can be mitigated by making the bending radius very large, which means the container must be wide to accommodate, which also translates to more APTES solution volume. Handling the fiber then proved to be difficult, resulting in inconsistent salinization. This same issue would resurface during the nanoparticle adsorption process using the silver nanoparticle colloidal solution. For these reasons, the coating apparatus presented in Figure 34 was created. It is made of two pipette tips joined together with an opening in the middle to dispense the solution and holds a liquid volume of ~800 μl.

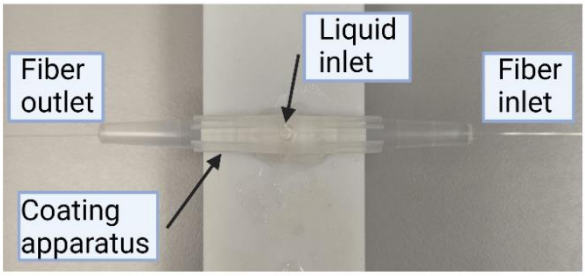


Figure 34 – Coating apparatus made for APTES functionalization

The fiber is inserted in this apparatus when its empty, and the solution is dispensed through the middle opening. After the process is complete, the fiber is slowly pulled from one end and washed. The design of this coating apparatus removes the need to bend the fiber and allows for the use of small volumes of solutions.

3.3 The effect of nanoparticle size on adsorption kinetics and absorption signal

Sizes 30 nm and 80 nm nanoparticles were chosen for this experiment and validate the findings of the modeling in 2.2. Two fibers were prepared based on the procedure presented in section 3.2. The sensing regions were then washed with DI water and dried with nitrogen stream then placed in new coating apparatuses. 30 and 80 nm silver nanoparticle colloidal solution were used to fabricate the first and second sensors respectively, by pouring in the solutions and submerging the sensing regions. The sensing regions remained in the colloidal solutions for 15 hours to study the effect of immersion time on the absorption signal. The spectrum was collected every minute with a scan average set to 5 and boxcar width set to 10. The results were imported to MATLAB for analysis. The moving average was set to 50 to reduce the noise of the signal, which was the value that would reduce the noise while retaining the signal's features. The results are plotted in Figure 35.

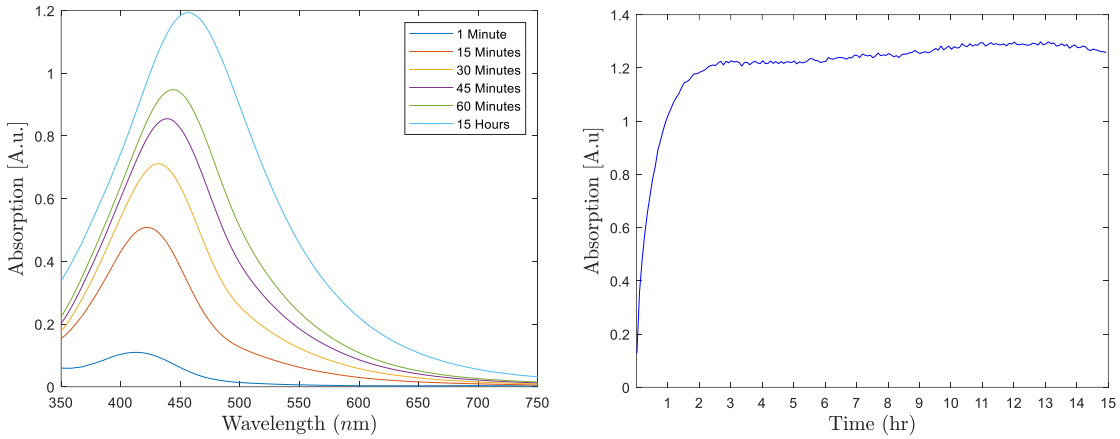


Figure 35 – Absorption signal vs: (a) wavelength (left) – (b) time (right)

Figure 35 (a) shows that LSPR was detected at 410 nm initially. However, as adsorption increased, the signal started shifting to higher wavelengths until finally it reached 450 nm. As stated in the combined model section, the effects of particle proximity that were not captured in the model are noticed in the experimental results. As more particles are adsorbing on the surface of the sensing region, more particles are agglomerating, affecting each other's electromagnetic field, and causing the LSPR frequency to reduce, which translates into a red shift and a broader absorption that is evident in the results. The recorded pattern in Figure 35 (a) resembles the results obtained from the model displayed in Figure 13, further confirming the viability of the model. The LSPR absorption measured over time for 30 nm nanoparticles is displayed in Figure 35 (b). The results obtained show how the absorption reaches its maximum after around 3 hours, suggesting that maximum surface density was reached.

The rate of adsorption was rapid between 0-2 hours, then slowed down between 2-3 hours. Since the adsorption rate is proportional to $\sqrt{t}$, the adsorption rate is expected to decrease over time. The fact that the adsorption stops completely after around 3 hours, which

was not captured in the adsorption model in Figure 12 (a), confirms the formation of the monolayer of nanoparticles, and suggests that the repulsion forces came into effect, preventing the adsorption of more particles on the sensing region. The signal of both sensors (30 nm based and 80 nm based) after 15 hours of adsorption was also recorded and plotted in Figure 36.

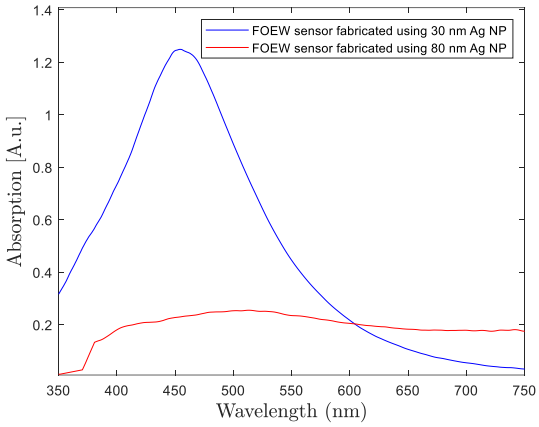


Figure 36 – Comparison of LSPR signals between 30 nm and 80 nm nanoparticle sensors after 15 hours of adsorption

Figure 36 displays that the LSPR signal from the sensor fabricated using the 30 nm silver nanoparticles is shown clearly by the peak that occurs around a wavelength of 450 nm. As for the sensor fabricated using the 80 nm nanoparticles, no peak can be easily distinguished from the spectrum. Although there is a slight peak at 510 nm, the absorbance is distributed over a wide range of wavelengths. This agrees with the simulations that show that the LSPR absorbance of 80 nm silver nanoparticles is significantly lower than the 30 nm silver nanoparticles. In addition, the adsorption of 80 nm particles on the fiber's surface results in significantly less particle density when compared to the adsorption of 30 nm nanoparticles as discussed earlier.

3.3.1 AFM Characterization

Atomic Force Microscopy (AFM) was used to characterize the sensor's surface after the fabrication process was completed. The AFM images are shown in Figure 37 for the sensors after 15 hours of incubation. Based on the adsorption model, it is expected to find a higher nanoparticle density and coverage on the surface of the sensor fabricated with 30 nm nanoparticles compared to the surface of the sensor fabricated with 80 nm nanoparticles.

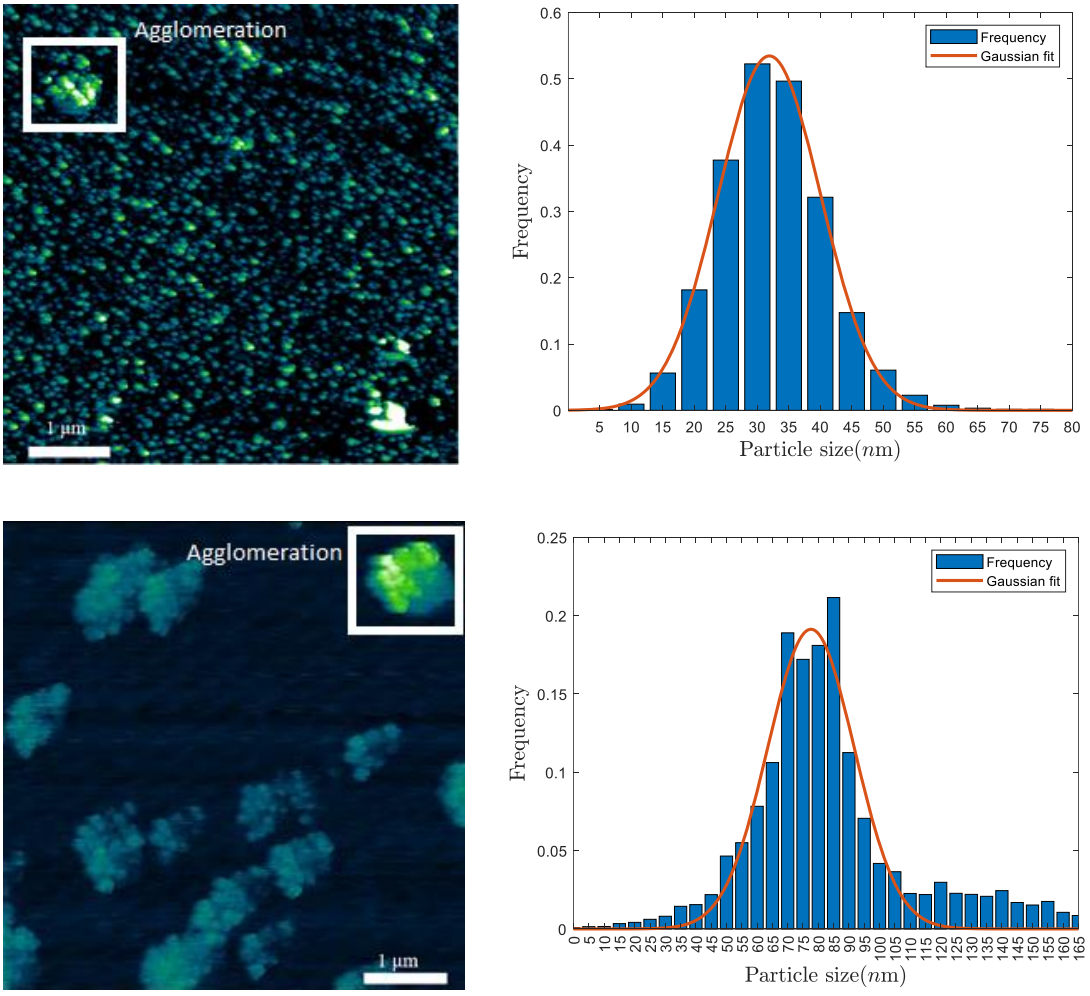


Figure 37 – AFM images and height distribution for fiber surface with: (a) 30 nm (top) – (b) 80 nm (bottom) – after 15 hours of incubation

The curvature of the fibers' surface posed a great challenge in our analysis. The images had to be corrected by leveling the surface of the fiber which introduced slight perturbations to the results. However, the conclusion is still valid. Comparing the results obtained through AFM in Figure 37, it can be observed that in the case of the 30 nm-based sensor, the nanoparticles have a high surface density, and are well dispersed in their coverage creating a distinct monolayer. Conversely, the 80 nm-based sensor shows very little nanoparticle density and coverage. Another observation worth noting is how the 30 nm-based sensor had minor agglomeration of the nanoparticles compared to the 80 nm-based sensor. This could be attributed to the larger nanoparticle size having more attraction forces due to the larger mass, while the repulsion Coulomb forces are able to stop the agglomeration in smaller nanoparticles. Additionally, during repeated testing, the findings from many AFM images for the 80 nm-based were consistent and did not show high density nanoparticles on the surface, while every AFM image for the 30 nm-based sensor reliably showed higher density and significant coverage, further agreeing with the adsorption model, and verifying it.

3.3.2 UV–VIS Characterization

UV–VIS characterization tests measure the total extinction of light based on the cross section, which includes both scattering and absorption. As mentioned earlier, FOEW sensors are only affected by an absorbing medium. To verify this statement, UV–VIS was used to characterize the 30 nm and 80 nm silver nanoparticle LSPR signals. For each size, 1 cm cuvette was analyzed containing 1 ml of 20 ppm nanoparticle colloidal solution. Another 1 cm cuvette

containing DI water was used as the reference. The results obtained from the UV-VIS tests were compared to the FOEW sensors and shown in Figure 38.

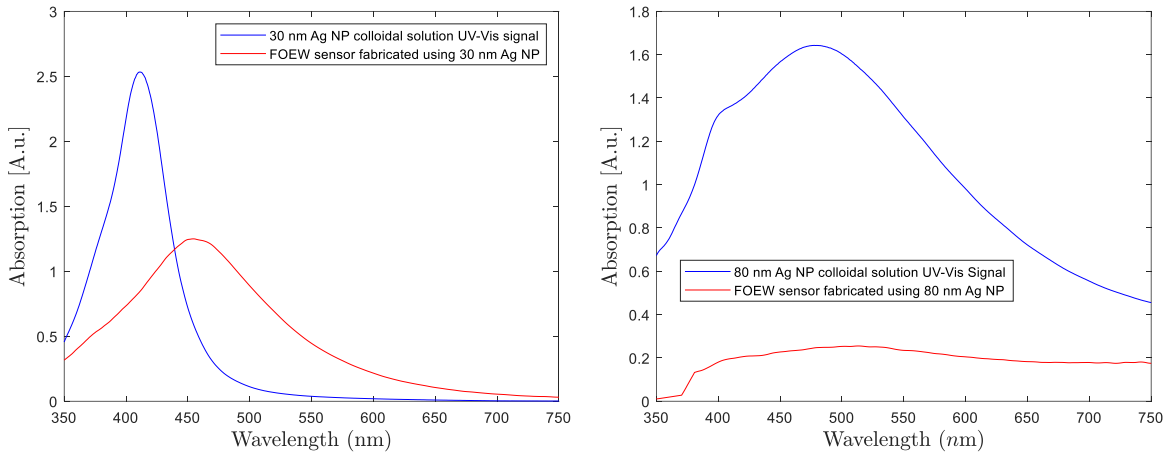


Figure 38 – Nanoparticle colloidal solution UV-VIS LSPR signal vs fiber optic evanescent wave LSPR signal in colloidal solution: (a) 30 nm (left) – (b) 80 nm (right)

From Figure 38 (a), it is noticed that the LSPR peaks are not aligned. The FOEW sensor LSPR is red-shifted and broader compared to the UV-VIS LSPR signal. This is due to the nanoparticles' agglomeration on the fiber's surface as discussed previously. This effect cannot be found in the nanoparticle solution as the nanoparticles are suspended freely due to their repulsion forces.

As for the 80 nm, it also noticed from Figure 38 (b) that the peaks are not aligned for the same reason. The peaks occur at a longer wavelength compared to the 30 nm particles due to the larger size of the nanoparticle. Additionally, the ratio of the absorption signal from FOEW compared to the UV–VIS is significantly lower for the 80 nm-based sensor compared to the 30 nm-based sensor. This is because in the FOEW sensor, the total absorption efficiency for the 80 nm particles is less than the 30 nm particles, and the final surface density is also

significantly less. However, in the UV–VIS test, the LSPR peaks observed are the result of the extinction cross section of the nanoparticles. It can be concluded that for the 80 nm particles, the LSPR signal from the UV–VIS is dominated by scattering, while for the 30 nm solution it is dominated by absorption. This verifies the results of the nanoparticle light interaction model, and that 30 nm particles are more suited for FOEW sensors. For that reason, it is crucial to always investigate the nanoparticles absorption efficiencies, not extinction efficiencies, when fabricating FOEW sensors.

3.4 The effect of nanoparticle size on FOEW LSPR refractive index sensitivity

In this section the sizes 10 nm, 20 nm, and 30 nm were chosen to verify the modeling results in section 2.3. The same procedure mentioned in section 3.3 was followed but with three fibers instead of two and for the three sizes. Each sensor was fabricated individually, and the signal was monitored in real time and plotted in Figure 39.

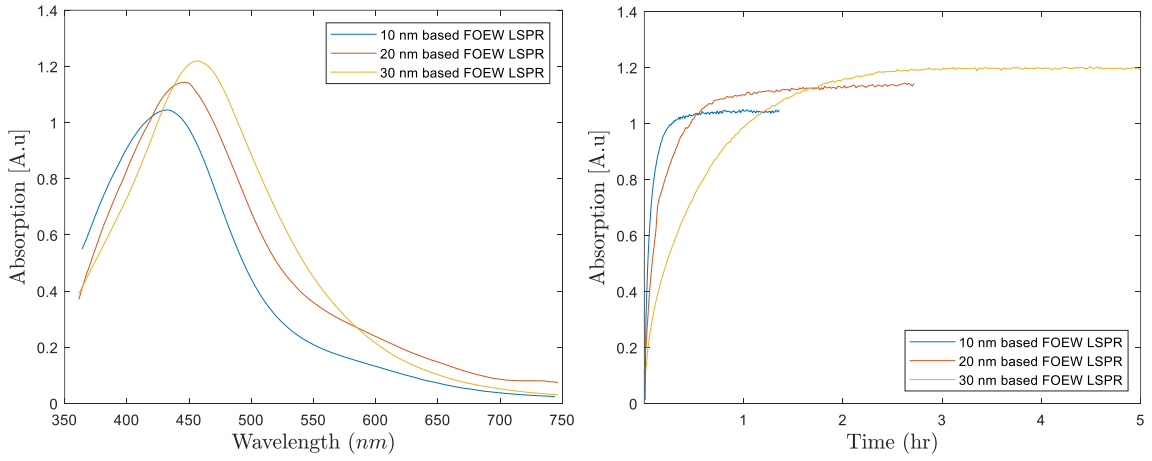


Figure 39 – (a) Absorption signal vs wavelength after adsorption process is complete (left) – (b) Absorption signal LSPR peak vs time for 10 nm, 20 nm, and 30 nm silver nanoparticle sensors (right)

Figure 39 (a) demonstrates that the final absorption of the three sensors was different despite using the same procedure and having the same sensing region lengths. The time required for the self-assembly and formation of a monolayer was also different as shown in Figure 39 (b). The reason the final absorption was highest for 30 nm and lowest for 10 nm can be attributed to the absorption efficiency of each nanoparticle size. As mentioned in the modeling results in 2.3, after the adsorption is complete and the sensing region is fully covered, the 30 nm-based sensor will have the highest absorption, while the 10 nm-based sensor will have the lowest absorption, despite the difference of surface density which is in favor of the smaller size. Figure 39 (b) also shows that the sensor fabricated using 10 nm nanoparticles had the highest adsorption rate, followed by the sensor fabricated using 20 nm nanoparticles, and finally the sensors fabricated using 30 nm nanoparticles

Another reason the absorption signal is different can be ascribed to the aggregation. Some aggregation was visible in the signal in the 30 nm-based sensor, which was less noticed in the 20 nm-based sensor and almost not present in any form in the 10 nm-based sensor. It seems that when the monolayer is formed, smaller nanoparticles (i.e., 10 nm) can repel other nanoparticles from adsorbing on the surface more efficiently compared to larger nanoparticles (i.e., 30 nm).

It is important to note how for shorter adsorption duration and before the full coverage of the sensing region, sensors fabricated using smaller nanoparticles (i.e. 10 nm and 20 nm) will have a higher absorption compared to sensors fabricated using 30 nm nanoparticles, which is also mentioned in 2.3. This can be verified by the experimental results shown above.

3.4.1 Refractive index sensitivity testing

The refractive index sensitivity of the three sensors was determined by measuring the LSPR wavelength of each sensor in solutions with different refractive indices. A dilution series of glycerol and DI water was created with $V_{glycerol}/V_{DI\ water}$ ratio of 0, 0.2, 0.4, 0.6, and 0.8. The values were obtained from [140] and are shown in Table 8.

Table 8 – Refractive index values of a dilution series of glycerol and DI water

Volume percentage glycerol/DI water	Refractive index
0%	1.34
20%	1.355
40%	1.381
60%	1.411
80%	1.440

The refractive index of each solution in the dilution series is lower than the refractive index of the sensing region to maintain TIR. Three sensors were made using each nanoparticle's size following the same fabrication method mentioned in section 3.2, and each measurement was performed three times per sensor. The LSPR peak was recorded for each sensor after fully immersing the sensing region in the solutions produced by the glycerol dilution series, the sensing region was washed with DI water to restore the baseline between measurements, and the sensitivity of the sensor was calculated based on equation (*2.25*). The sensors would be washed with DI water and immersed in another solution results are shown in Figure 40

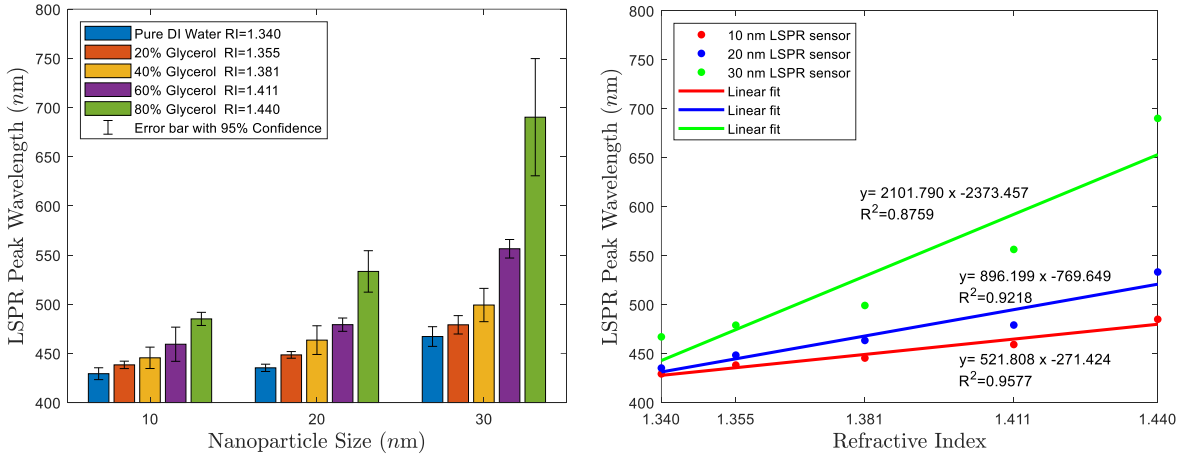


Figure 40 – Refractive index sensitivity testing results – (a) LSPR vs Size (left) – (b) LSPR vs Refractive Index (right)

Figure 40 (a) demonstrates that 30 nm-based sensors are significantly more sensitive to changes in medium refractive index compared to 20 nm-based sensors and 10 nm-based sensors. The LSPR peak would shift considerably when increasing the refractive index of the medium. Figure 40 (b) shows that the 30 nm-based sensors had a sensitivity of 2101.79 nm/RIU, compared to 896.199 nm/RIU for the 20 nm-based sensors, and 521.808 (nm/RIU) for the 10 nm-based sensors. This is attributed to the higher absorption, longer electromagnetic field decay length, and higher refractive index sensitivity of the 30 nm nanoparticle, which agrees with the modeling results found in sections 2.2, 2.3, and 2.4.

However, the 10 nm-based sensor had a better linearity at $R^2 = 0.9577$, compared to $R^2 = 0.9218$ for the 20 nm-based sensor and $R^2 = 0.8759$ for the 30 nm-based sensor which could be attributed to the more uniform monolayer and less nanoparticle aggregation when fabricating the sensor using smaller nanoparticles.

3.4.2 SEM Characterization

Scanning Electron Microscopy (SEM) was used to characterize the sensor's surface after the fabrication process was completed. SEM was chosen instead of AFM here to avoid having to correct for the surface curvature and for the higher picture quality considering the smaller nanoparticle sizes. ImageJ, which is an open-source software, was used to count the nanoparticles from the images to find the surface density. The results showing the SEM images for each nanoparticle size, along with a count distribution graph are displayed in Figure 41.

Similar to the modeling results in 2.2.2, and the AFM images in 3.3.1, the SEM images show that smaller nanoparticle sizes result in higher final surface density. The time required to achieve a monolayer for each nanoparticle size was interpolated from Figure 39 (b), and used in (2.8) to determine the theoretical final density. These results were compared to the experimental ones produced by ImageJ and displayed in Table 9. Due to the smaller size of the 10 nm nanoparticles, in many instances ImageJ was not able to differentiate two particles next to each other and would count them as one. This explains the large discrepancy found in the 10 nm results. However, the 20 nm and 30 nm results further verify the diffusion transport process model.

Table 9 – Comparison between theoretical and experimental surface densities

Particle Size (nm)	10	20	30
Theoretical density (μm^2)	~690	~125	~50
Experimental density (μm^2)	~470	~140	~43
Error	46.8%	10.7%	16.3%

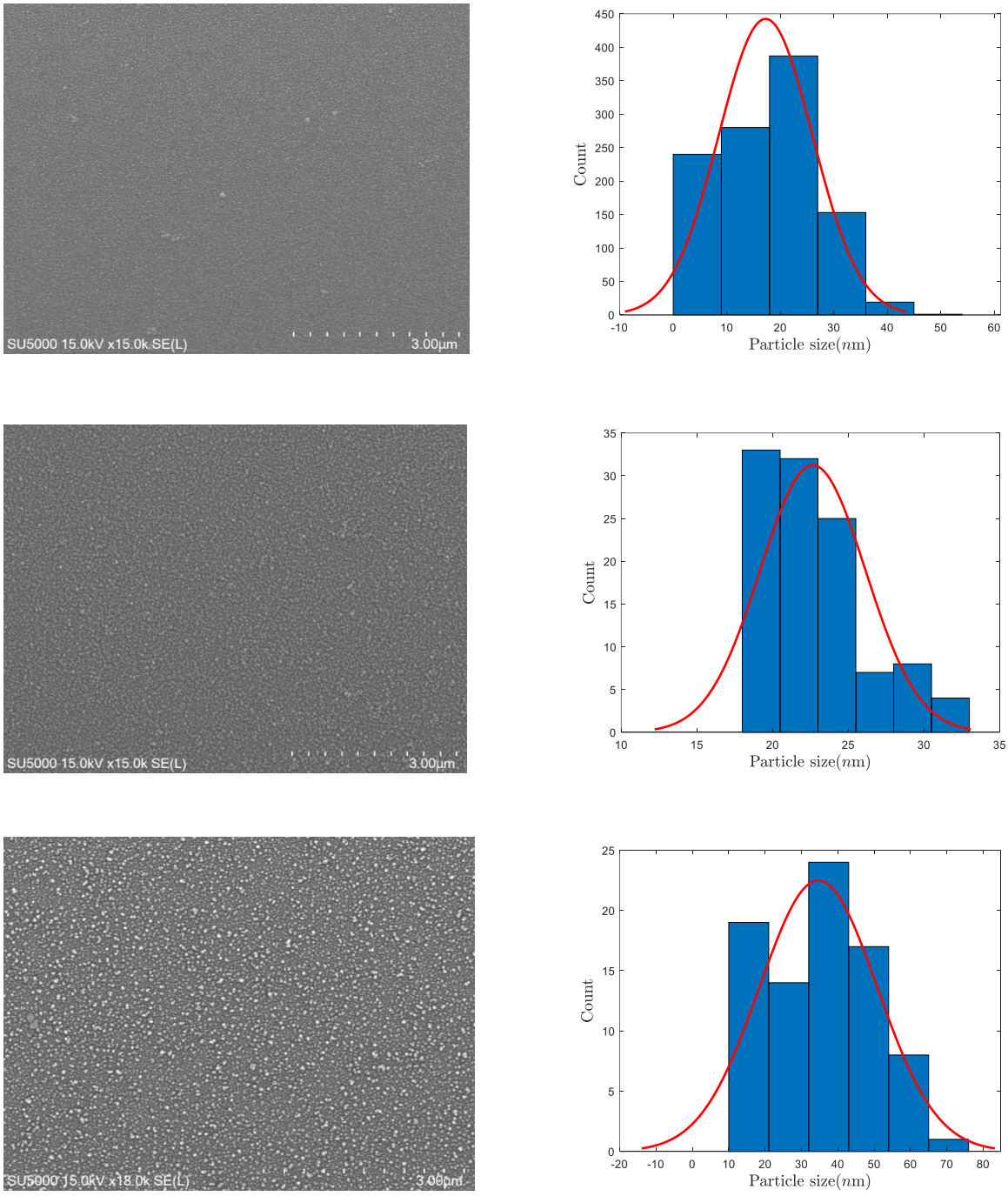


Figure 41 – SEM images and count for fiber surface with: (a) 10 nm (top) – (b) 20 nm (middle) – 30 nm (bottom) nanoparticles

3.5 Sensor response model update based on experimental results

The sensor response model based on de Feijter's equation (2.32) was updated to include the refractive index sensitivity of the 30 nm-based FOEW LSPR sensor found experimentally in section 3.4.1. The results are shown in Figure 42.

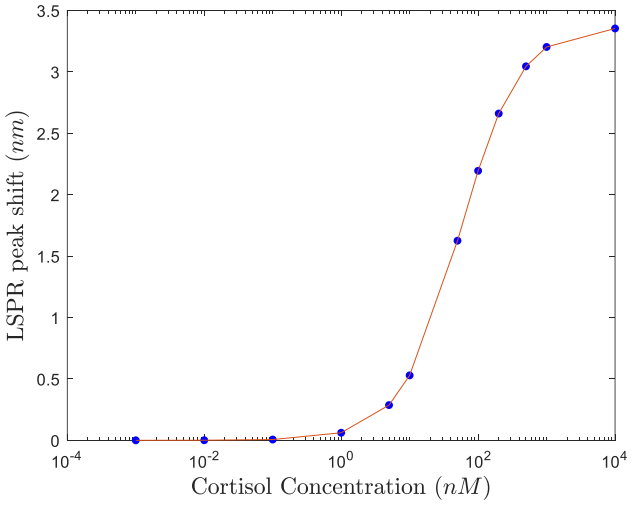


Figure 42 – Updated sensor response model based on the experimental sensitivity of 30 nm based FOEW LSPR sensor using 125 µm coreless fiber as the sensing region

Figure 42 depicts a significantly higher sensor response for the updated model which is expected since the refractive index sensitivity was significantly higher experimentally compared to the 2D COMSOL model (2101.79 nm/RIU vs 196.714 nm/RIU). The higher sensitivity of the actual sensor compared to the 2D model is due to the difference in optical fiber size (125 µm vs 3 µm), which translates into more coupled modes, nanoparticle surface density, distance between nanoparticle and surface, and structure (3D vs 2D). According to the results of this chapter, which agree with the modeling results, the 30 nm silver nanoparticles are best suited to fabricate the FOEW LSPR salivary cortisol biosensor.

Chapter 4
LSPR FOEW Cortisol Biosensor Fabrication and Testing

This chapter will demonstrate in detail the experimental procedures followed to fabricate the FOEW LSPR cortisol biosensor. The material used, fabrication approach, problems faced, troubleshooting, as well as the results will be thoroughly discussed. The results obtained from the modeling in Chapter 2 and experiments from Chapter 3 all point towards the 30 nm being the optimal size for fabricating the cortisol biosensor. Thus, the FOEW LSPR Cortisol biosensor will be fabricated and tested using 30 nm silver nanoparticles.

4.1 Materials

Gilson PIPETMAN P1000 pipette, VWR analogue mini vortex mixer, MUA (11-Mercaptoundecanoic acid), Cys (Cysteamine hydrochloride), Cortisol (Hydrocortisone solution), PBS (Phosphate buffered saline), were purchased from Sigma-Aldrich. EDC (1-ethyl-3-(3-dimethylaminopropyl) carbodiimide hydrochloride), NHS (N-hydroxysuccinimide), Blocker™ BSA were purchased from Thermofisher. Finally, Cortisol antibodies were purchased from antibodies-online. 11 Pico Plus syringe pump (Harvard Apparatus). Valco 6 port valve (Vici). PEEK tubing (1/16'' OD 0.03''ID). (Sylgard 184, Dow Corning).

4.2 Biosensor fabrication

The steps presented in Chapter 3 were followed to create the FOEW LSPR sensor. Once the sensor was fabricated, the next step would be to functionalize the nanoparticles for the ligand (Anti-cortisol IgG) conjugation.

One of the most utilized chemicals for this step is MUA (11-Mercaptoundecanoic acid). MUA has been used for successfully in many LSPR/SPR sensors [41,141–153]. MUA are molecules that have thiol groups (-SH) from one end and carboxyl ($-COO^-$) groups from the other. Thiol groups have high affinity to gold and silver, attacking the functional groups found on the metal surface and replacing them with thiol [154]. The carboxyl group on the other end can be activated using EDC (1-ethyl-3-(3-dimethylaminopropyl) carbodiimide hydrochloride) and NHS (N-hydroxysuccinimide) chemistry.

The application of EDC/NHS chemistry is nearly universal in particle and surface conjugation procedures. EDC/NHS activation chemistry is considered a "zero-length" cross linking procedure [74]. It is the most common bioconjugation reagent used today [76]. EDC/NHS activates the surface by converting the carboxyl groups into NHS-ester (succinimidyl ester). Coupling is then achieved by introducing the ligand (Anti-cortisol IgG) to the NHS-activated surface. The amine groups found on the ligand would interact with the NHS-ester in a process known as aminolysis, forming amide bonds [75]. The selectivity of the sensor depends on the ligand used. A monoclonal antibody is selective to one type of the analyte, while using aptamers can further enhance the selectivity.

The selectivity can also be affected by nonspecific binding of the analyte to the surface of the nanoparticle. To avoid this undesired outcome, the empty sites on the nanoparticles surface should be blocked. Commonly, bovine serum albumin (BSA) is used since it does not interact with the ligand or analyte [28].

4.2.1 MUA concentration optimization

The concentration of MUA used to functionalize the metal surface depends on many factors and varies for different applications [76]. Thus, this can only be determined experimentally. Table 10 below shows some of the information found in the literature about MUA for similar applications [155].

Table 10 – List of MUA concentrations and incubation times used in SPR/LSPR sensors

Concentration [mM]	Time [Hr]	Solvent	Reference
10	24	Ethanol	[146]
10	12	Ethanol	[147]
1	24	Ethanol	[148]
10	24	Ethanol	[149]
5	2	Ethanol	[150]
10	20-24	Ethanol	[151]
1	12	Ethanol	[152]
1	4	Ethanol	[153]

There are other reported cases where a higher concentration (150 mM) was used [156,157]. For the sensor presented in this thesis, an ethanolic MUA solution with a concentration of 5 mM was initially used. However, due the challenges presented in section 3.2.3, which require the need to use the inhouse coating apparatus, the MUA functionalization was not successful. Due to the low surface tension of ethanol, the solution would pour out of the fiber inlet and outlet openings in the coating apparatus before fully submerging the sensing region. In the instances where the sensing region would be submerged, the ethanol would evaporate quickly and leave a visible white residue (MUA) on the sensing region surface.

This issue was resolved by pre-functionalizing the silver nanoparticles with MUA prior to the adsorption process. After contacting CYTODIAGNOSTICS® technical team, they confirmed that this is possible by adding a small amount of ethanolic MUA solution to the nanoparticle colloidal solution and incubate it for some time. Pre-functionalizing the nanoparticles with MUA would allow for the sensor to be activated via EDC/NHS chemistry directly after the adsorption process. Then the antibodies can be conjugated on the nanoparticles surface, before BSA is used to block the remaining sites. A schematic explaining the fabrication process and testing of the biosensor is presented in Figure 43.

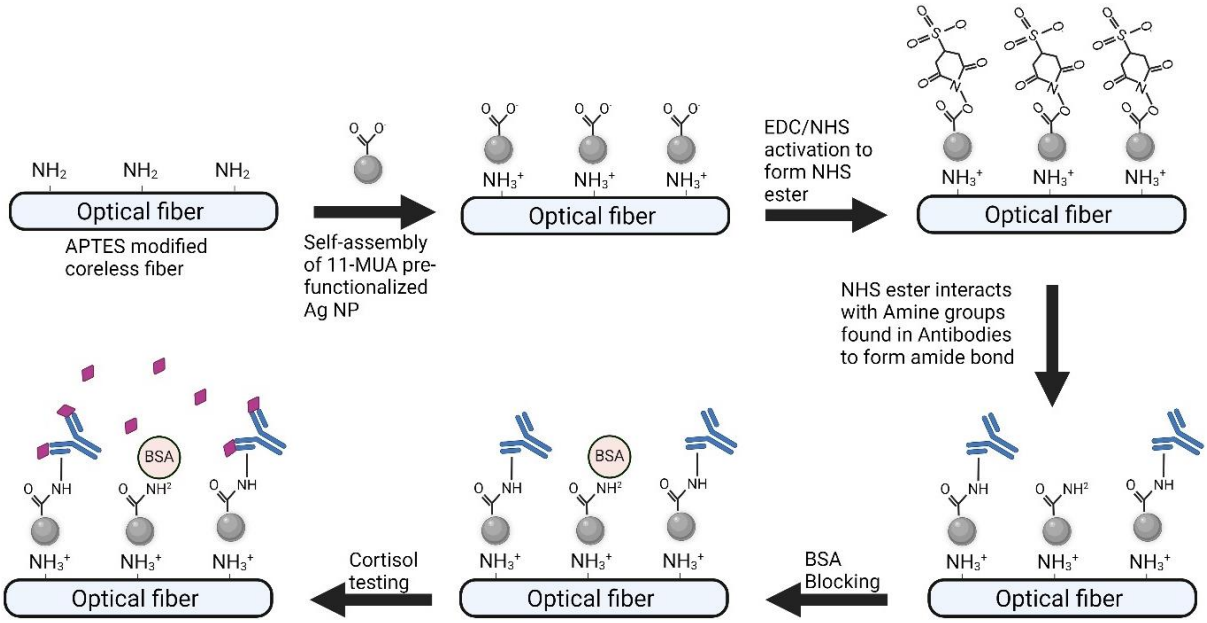


Figure 43 – Schematic showing the FOEW LSPR Cortisol biosensor fabrication process and testing based on MUA pre-functionalization – Created with BioRender.com

Four concentrations of 0.5, 1, 5, and 10 mM were considered for the purpose of testing the pre-functionalization approach. 20 μl of ethanolic MUA from each concentration were added to separate vials containing 980 μl of 30 nm colloidal solution each and incubated for

two hours. The volume of the ethanolic MUA, colloidal solution, as well as the incubation time were kept constant for the four sensors to control the variables and only the concentrations were changed. After the 2 hours, the sensors were fabricated following the procedure mentioned in Chapter 3. The results are shown in Figure 44.

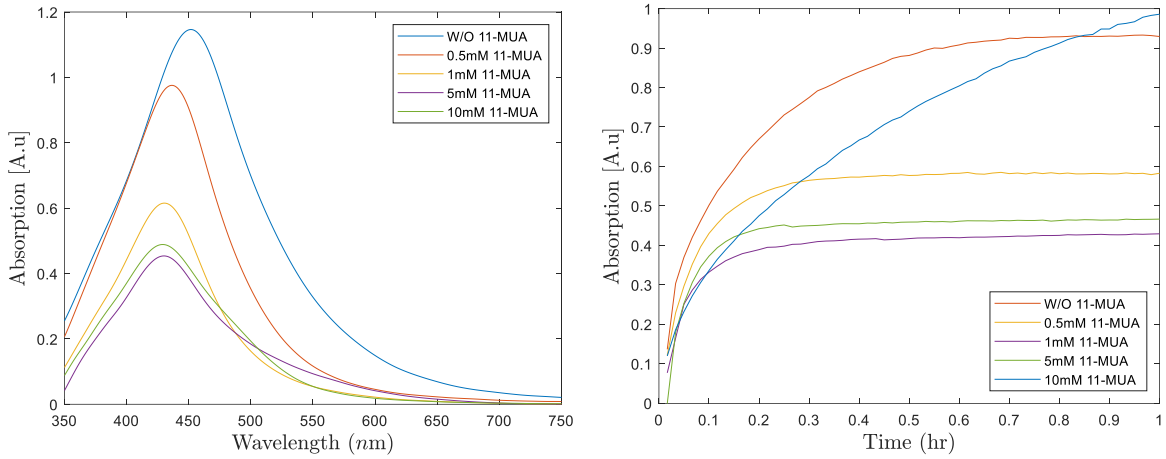


Figure 44 – (a) Absorption signal vs wavelength after adsorption process is complete for different MUA concentrations (left) – (b) Change of LSPR peak absorption magnitude over time for different MUA concentrations (right) – after 2 hours of incubation time

Figure 44 (a) shows a decrease in LSPR signal as the concentration of MUA increases. This can be attributed to the effect of MUA on the surface charge of the nanoparticle. High MUA concentrations increase the surface charge on the nanoparticles' surfaces, increasing the repulsion forces between the nanoparticles, which causes the monolayer to form quicker. This is also reflected in the quicker adsorption time as shown in Figure 44 (b). Although this proves the pre-functionalization is working, however, a lower absorption signal is the result of less particle coverage, which affects the sensitivity of the sensor as discussed in Chapter 2. To verify these claims, an SEM image is taken of the sensing region fabricated with 0.5 mM MUA pre-

functionalized nanoparticles and compared to the one fabricated without the pre-functionalization step. The results are shown in Figure 45.

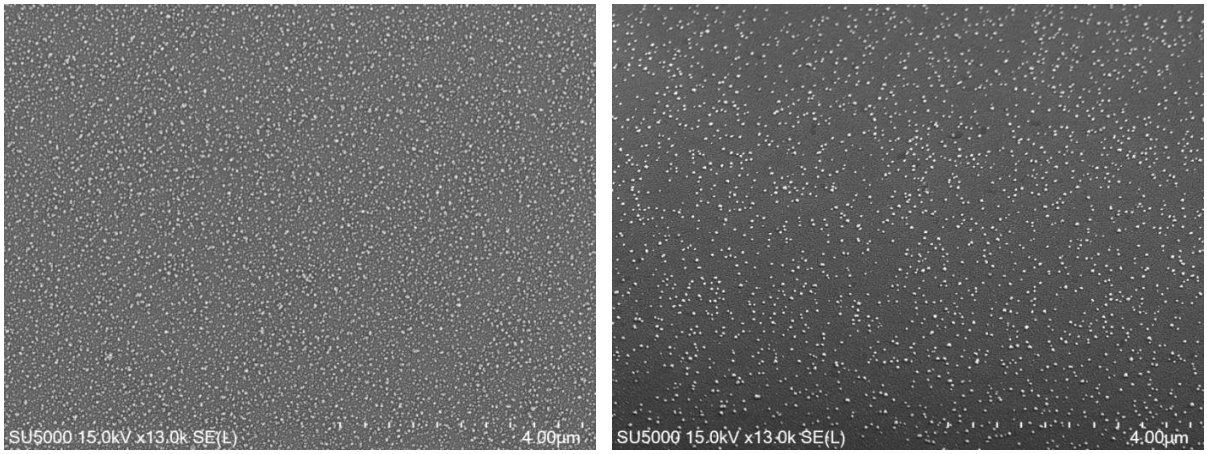


Figure 45 – SEM image of 30 nm based FOEW LSPR sensor: (a) without MUA pre-functionalization (left) – (b) with 0.5 mM MUA pre-functionalization for 2 hours (right)

It is clear from the SEM images that pre-functionalization results in less nanoparticles density on the sensing region, due to the reasons mentioned earlier. Based on the conclusions drawn from the modeling on how this affects the sensitivity, the decision was made to choose 0.5 mM MUA prefunctionalized nanoparticles for the fabrication of the sensor and disregard the remaining concentrations. Using this concentration results in the adsorption of nanoparticles functionalized with carboxyl groups required for the bioconjugation, which is confirmed by the results obtained in Figure 44, while maintaining a high absorption signal. Consequently, this results in a better overall sensor performance compared to using nanoparticles pre-functionalized with higher MUA concentrations.

4.3 Experimental Setup

The experimental setup used to perform the remaining fabrication steps and testing is shown in Figure 46. It consists of a syringe pump that provides continuous flow of the medium

at a constant flowrate, the MUA pre-functionalized FOEW LSPR sensor enclosed in a PDMS microchannel and connected to the light source and spectrometer, an injection valve with a sample loop that allows for seamless injection of precise volumes of samples into the system, a waste collection container, and a laptop to record the optical response.

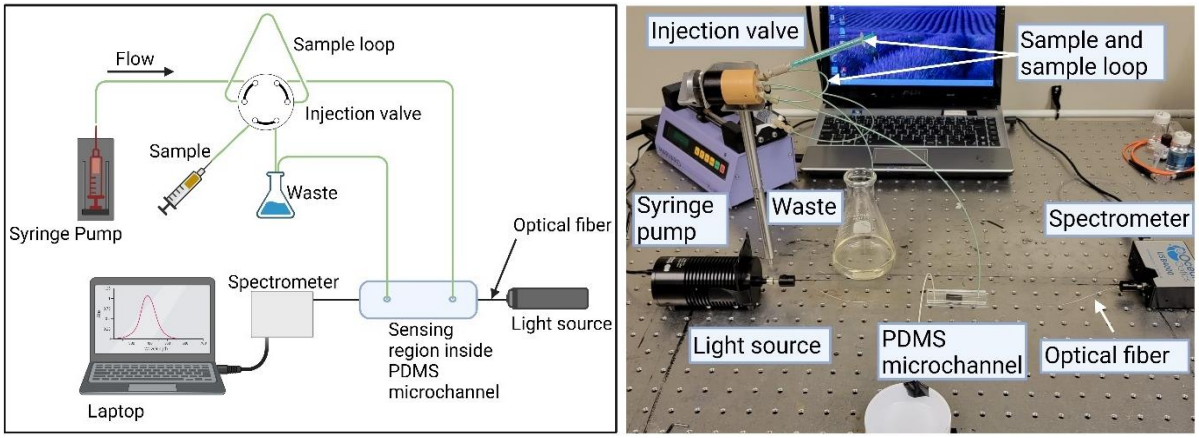


Figure 46 – (a) Experimental setup schematic (left) – (b) Actual experimental setup (right) – Created with BioRender.com

Phosphate buffered saline (PBS) with a concentration of 10 mM and pH of 7.4 was used as the medium from this point onwards in the experiment. It is a non-toxic solution that is widely used with biosensors and biological applications as its osmolality and ion concentration are analogous to the human body [158,159]. A 12 ml HENKE-JECT® syringe was filled with PBS solution and placed in the syringe pump. The flow rate was set to 22.7 $\mu l/min$ which results in a flow velocity of 1 mm/s inside the microchannel, like the flow velocity used in the modeling in section 2.5. The sample loop had a volume of 450 μl which would result in the sensor surface being exposed to the sample volume for 20 minutes. A 1 ml HENKE-JECT® syringe was used to inject different samples into the system using the injection valve. The setup was constructed on top of an optical table by NEWPORT®.

An aluminum mold for the PDMS microchannel was designed using SOLIDWORKS and made by CNC machining to replicate the dimensions of the microchannel shown in the model in section 2.5 (refer to Appendix B).

Sylgard 184 silicone elastomer and curing agent were mixed at a (10:1) w/w ratio thoroughly and placed in a vacuum desiccator until all the bubbles were extracted from the mixture, then poured in the aluminum mold and cured at 75° C for 2 hours. Rapid-core sampling puncher with a diameter of 1.2 mm was used to punch holes in the PDMS and create the inlet and outlet. The FOEW LSPR sensor was placed inside the microchannel and a glass slide was used to seal the channel. The aluminum mold and sealed PDMS microchannel with the FOEW LSPR sensor enclosed inside are shown in Figure 47.

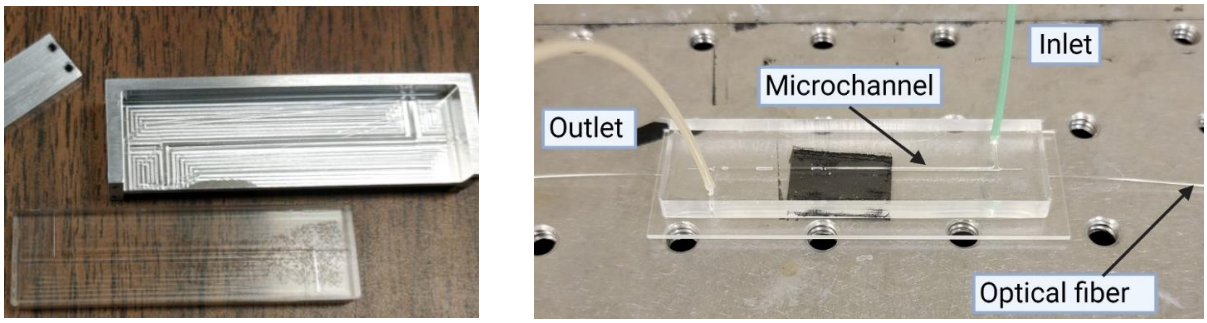


Figure 47 – (a) Aluminum mold used to create the PDMS micro channel (left) – (b) The final sealed channel with the FOEW LSPR sensor enclosed

4.3.1 Surface Activation and Antibody Conjugation Procedure

Once the system was primed with the PBS solution, a baseline LSPR signal was recorded. The concentration of EDC/NHS used in the literature varied tremendously. It depends on the application, concentration of nanoparticles, concentration of biological molecules, pH level, and buffer type [76]. Typical concentrations of 5-500 mM were used. Nevertheless, using excess concentrations of EDC/NHS during the bioconjugation procedure

is common since the unreacted molecules will always be washed away after the activation process is complete. In this work, a concentration of 200 mM EDC and 50 mM NHS was used. The concentrations were freshly prepared in PBS and injected into the system. The activation process can be observed from the initial shift in LSPR signal, and it is shown in Figure 48.

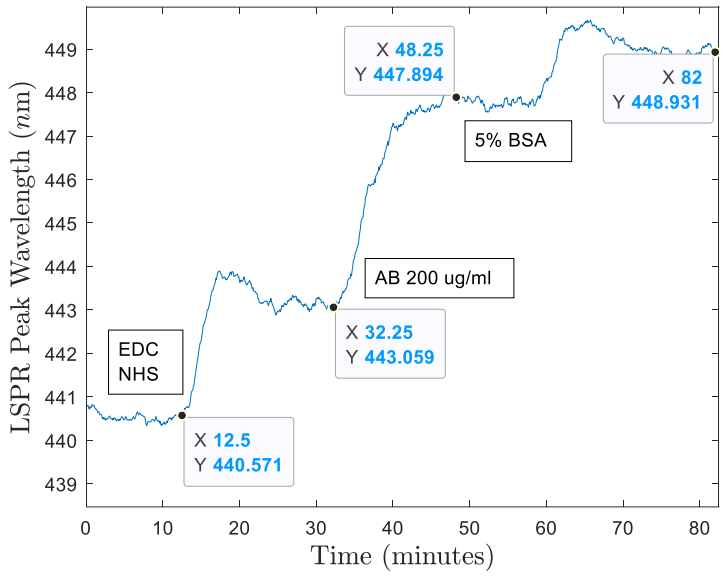


Figure 48 – LSPR peak shift due to EDC/NHS activation, antibody conjugation, and BSA blocking processes

In this figure, the LSPR peak during the EDC/NHS activation shifts from 440.571 nm to almost 444 nm, but then drops to 443.059 nm. This slight drop in the signal after the activation process is attributed to the excess EDC/NHS particles being washed away, confirming that the concentration of EDC/NHS used was sufficient for the activation process. The activation process took around 15 minutes to complete. A 200 $\mu g/ml$ of anticortisol antibodies in PBS was then injected into the system. The LSPR peak is observed to shift from 443.059 nm to 447.894 nm over 16 minutes confirming the bioconjugation step. Finally, 5% BSA was used to block the remaining sites, which caused a shift in the LSPR peak from

447.894 nm to 448.93 nm . The concentration of BSA is also used in excess to make sure all the sites are blocked. The remaining unreacted particles are washed away by the solution, which can be noticed by the slight drop in the LSPR peak signal after the blocking process. The full spectrum showing the LSPR peak wavelength shift after each process is presented in Figure 49 below.

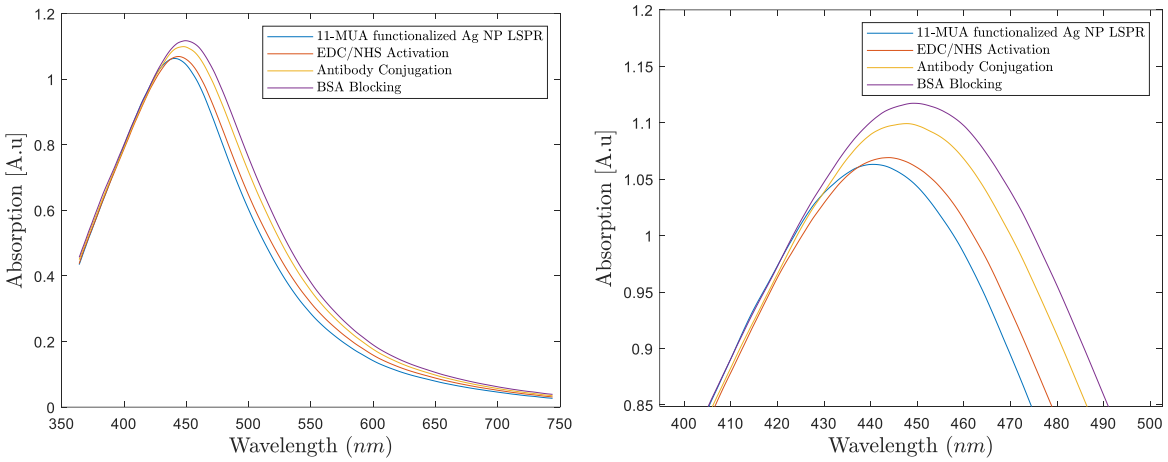


Figure 49 – (a) Full spectrum showing LSPR peak wavelength shift after each process (left) – (b) Zoomed in spectrum focusing on the peaks only (right)

Figure 49 highlights that the absorption magnitude is also affected by each process. This is expected since each process affects the local refractive index around the nanoparticle, which affects both the magnitude and wavelength of LSPR as mentioned in Chapter 2. It is also observed that the sensitivity of the LSPR peak absorption magnitude shift is higher than the LSPR peak wavelength shift, potentially resulting in a sensor with better performance characteristics when sensing based on absorption peak shift versus wavelength shift. However, during testing, it was noticed that light absorption is very sensitive to baseline drift, which occurs when the light source is operating for a long time. This phenomenon does not affect the

wavelength, making this sensing method more robust and reliable. In this work, as mentioned earlier, the wavelength shift is considered the basis of our sensing method.

Before performing the cortisol testing, the concentration of antibodies used was optimized. The same fabrication process mentioned earlier was repeated with different concentrations of antibodies. Multiple sensors were fabricated with 15, 20, 25, 30, 100, 150, 200, and 500 $\mu g/ml$ concentrations each and the results are presented in Figure 50.

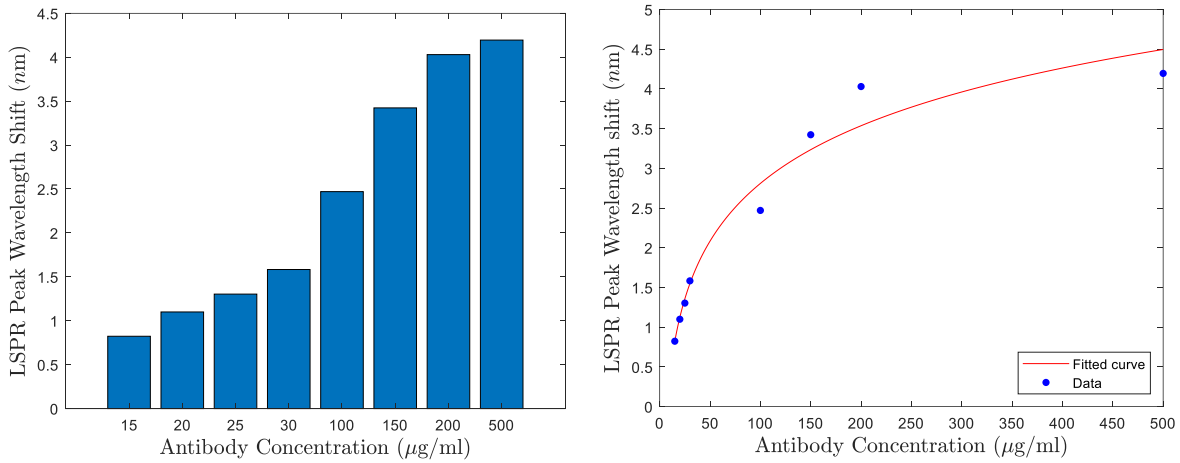


Figure 50 – (a) antibody concentration vs LSPR peak wavelength shift bar graph (left) – (b) logarithmic graph (right)

Figure 50 shows excellent correlation between the concentration of antibodies used and the shift in LSPR peak wavelength. The higher concentrations of antibodies result in a larger shift in LSPR wavelength, due to the higher yield of conjugation, which translates into a larger change in the local refractive index around the nanoparticle. The conjugation process was also noticed to take less time to complete using higher antibody concentrations. Based on the outcome of this test, the difference between the LSPR peak wavelength shift between when using 200 $\mu g/ml$ versus 500 $\mu g/ml$ is minimal. Which suggests that these higher

concentrations saturate the nanoparticles' surface. Thus, fabricating the sensor using 500 $\mu g/ml$ will result in the highest change in local refractive index during cortisol testing, since this translates to more active sites available for binding. For this reason, this concentration was used for the fabrication of this sensor.

Due to the high cost and low supply of the antibody solution, the excellent correlation presented in Figure 50, and the need to fabricate multiple more sensors for testing, this optimization process was done once only.

4.3.2 Cortisol Testing and Results

The cortisol testing was done by preparing 0.001, 0.01, 0.1, 1, 5, 10, 50, 100, 200, 500 and 1000 nM from pure hydrocortisone solution in PBS. This range of cortisol concentrations covers the salivary cortisol concentrations and is consistent with the modeling done in section 2.5. Actual saliva samples could not be tested due to university policies regarding biological samples. The implications of using actual saliva samples on the results of the sensor are discussed thoroughly in section 5.2.

A total of 17 sensors were fabricated and tested using the fabrication method described earlier. Unfortunately, there was no quantifiable response that could be recorded and analyzed. Most of the sensors did not react at all to the different cortisol concentrations. While some did react at higher concentrations (i.e., 1 mM), the reaction was minimal and could not be reproduced. Thus, more research was done into the fabrication method and the analyte-ligand interaction kinetics and conjugation procedures.

4.3.3 Potential reasons behind the unsuccessful experiment

Further analysis and research performed resulted in two potential reasons for the unsuccessful experiments. First, although MUA functionalization is widely used in LSPR/SPR biosensor functionalization in the literature, most of the work using this chemical included functionalizing gold nanoparticles. While few papers have used MUA with silver nanoparticles, the construction of these sensors allows for functionalization of the nanoparticles after the adsorption procedure. This prompted the research into the effect of MUA on silver nanoparticles, which resulted in the finding that the (OH-) groups found in ethanol affect the silver nanoparticles in a negative way. They were found to have a higher affinity to silver than the thiol groups present in MUA, binding with silver nanoparticles instead and forming aggregates [155], which reduce the activity of the nanoparticles and result in a sensor with inferior performance [141]. The (OH-) were also found to damage the nanoparticles surface and cause oxidization of the silver, resulting in a lower sensitivity [155].

The second potential reason for the unsuccessful experiment can be attributed to the orientation of the antibodies conjugated on the surface of the nanoparticle and the molecular weight of the analyte. Due to the chemical construction of the IgG antibodies, the amine groups which bond with the activated carboxyl groups are found on the sides of the antibody as shown in Figure 51 [160,161]. This means that the majority of the antibodies conjugated on the nanoparticles are either laying on their sides, or upside down blocking the available sites, which reduces the over sensitivity of the sensor [162].

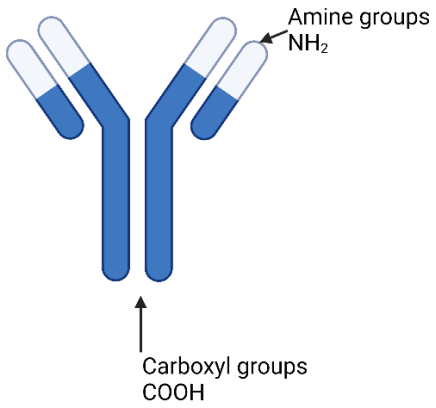


Figure 51 – Simple representation of the chemical structure of IgG antibodies – Created with BioRender.com

The aforementioned reasons for the unsuccessful experiment, combined with the results presented in section 2.5 showing how the miniscule size of the cortisol molecule compared to the antibody would barely affect the local refractive index around the nanoparticle, require the need to find another fabrication approach. The new approach should use a functionalization reagent that can be diluted in water to avoid the undesirable effects of ethanol on silver and allow for the functionalization of the nanoparticles surface after the adsorption process. Additionally, the conjugation process should be optimized to maximize the conjugation of end-on orientation of antibodies on the nanoparticles' surface. This would result in maximum available sites for analyte-ligand interactions, which should produce a working sensor, based on extremely high refractive index sensitivity found for the sensor presented in this work in section 3.4.1.

4.4 Cysteamine Functionalization

The chemical reagent Cysteamine Hydrochloride was found to satisfy the requirements needed for the new fabrication approach. Cysteamine Hydrochloride can be diluted in water, avoiding the need for ethanol, and was used successfully in the functionalization of metal surfaces in biosensors [163–165]. It consists of a thiol group from one end, which binds with high affinity the silver surface, and amine groups from the other end ready to bind with activated carboxyl groups. IgG antibodies can be activated with EDC/NHS prior to the conjugation process, allowing for a higher yield of end-on orientation of conjugated antibodies based on the location of the carboxyl groups in the antibody chemical structure, and subsequently better sensor performance due the more available binding sites. The schematic showing the new fabrication process of the FOEW LSPR cortisol biosensor based on Cysteamine is shown in Figure 52 below.

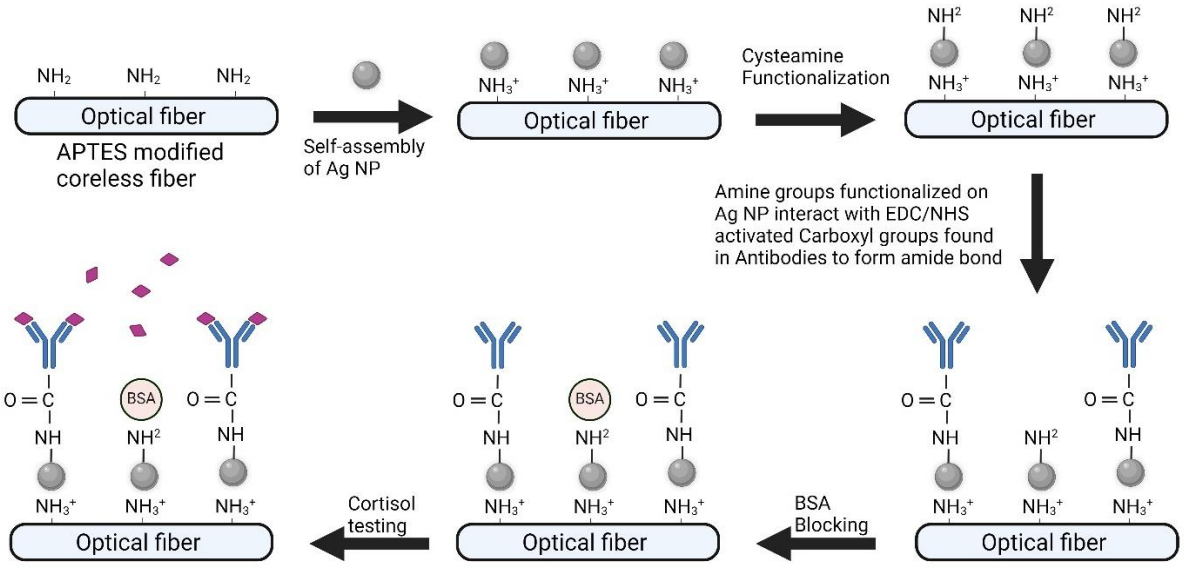


Figure 52 – Schematic showing the FOEW LSPR Cortisol biosensor fabrication process and testing based on Cysteamine functionalization – Created with BioRender.com

4.4.1 Surface functionalization and Antibody Conjugation Procedure

The same fabrication procedure mentioned in Chapter 3 was implemented. After the adsorption process was completed, the sensing region was immersed in 20 mM aqueous solution of Cysteamine hydrochloride over night, which is analogous to the procedure for similar biosensors [163–165].

Immediately after immersing the sensing region in the Cysteamine solution, the absorption signal started to drop. This drop verifies that the functionalization is taking place. Unlike the MUA, the functionalization using Cysteamine will result in amine groups on the surface of the nanoparticles, which has a positive charge, and will disrupt the ionic bond between the fiber surface and the nanoparticles causing the nanoparticles to detach from the surface. The concentration of Cysteamine used and the functionalization time were higher than required, as the next day the signal was completely lost. The sensors presented in the literature using cysteamine hydrochloride were SPR based, and the thin metal film was deposited on the surface of the sensor, unlike the case in our sensor where the nanoparticles were adsorbed on the surface, thus this effect was not observed.

To mitigate this issue, the concentration of Cysteamine was lowered to 5 mM, and the functionalization time was reduced to 2 hours. The absorption signal as well as LSPR wavelength were observed during the functionalization process and the results are displayed in Figure 53.

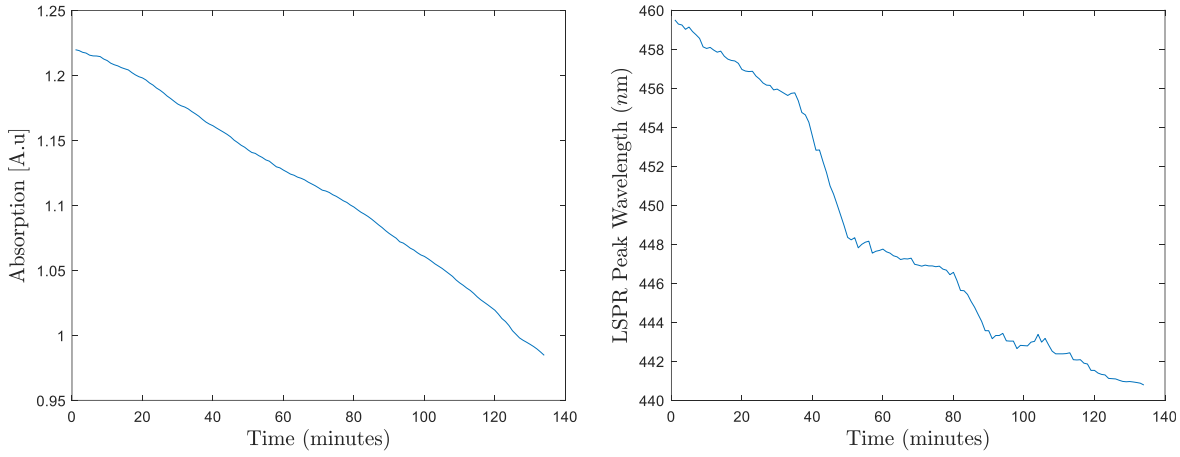


Figure 53 – (a) LSPR absorption peak during the Cysteamine functionalization process (left) – (b) LSPR wavelength during the Cysteamine functionalization process (right)

Figure 53 (a) shows the decreasing absorption signal due to the Cysteamine functionalization. However, Figure 53 (b) shows that the LSPR wavelength is also decreasing. This is also attributed to some of the nanoparticles detaching from the surface of the fiber. The detached particles are mostly agglomerated, which explains the drop in the LSPR wavelength. It was also noticed that some visible aggregation presented in the signal prior to the Cysteamine functionalization was significantly reduced, which is an added and unpredicted benefit of using Cysteamine for the functionalization process.

After the functionalization process was complete, the sensor was placed inside the PDMS microchannel in the same setup configuration mentioned in section 4.3. The carboxyl groups in the antibodies were activated by adding 500 μL of 200 mM EDC and 50 mM NHS (1:1) to 500 μL of 500 $\mu g/mL$ IgG anti-cortisol antibodies and allowed to react for 10 minutes. The antibodies were then injected into the system and the shift in LSPR wavelength signal was observed and plotted in Figure 54.

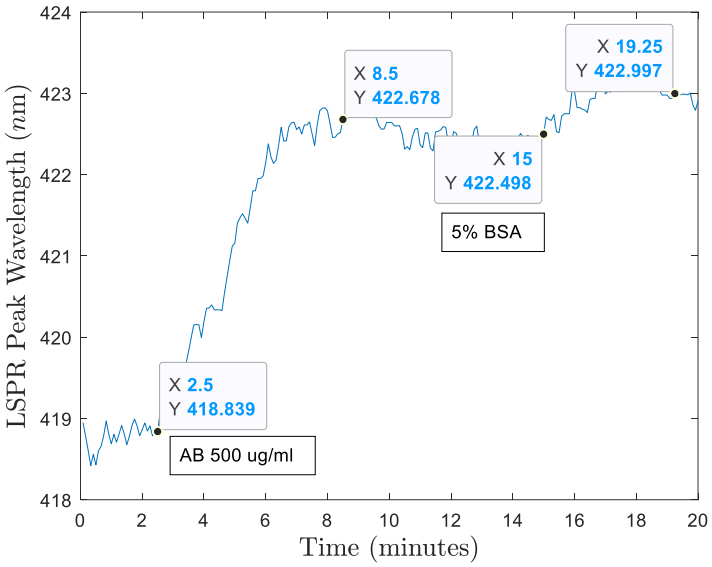


Figure 54 – LSPR peak shift due to pre-activated antibody conjugation, and BSA blocking processes

As shown in Figure 54, the LSPR peak increased from 418.839 nm to 422.678 nm confirming the conjugation process. The conjugation process happened at a faster rate compared to the results in Figure 50. This is attributed to the higher concentration of antibodies used, and the different fabrication process approach. However, the increase in LSPR peak wavelength based on the concentration of the antibodies used is consistent with the results found in Figure 50. After the conjugation process, the BSA blocking process was performed by injecting the BSA solution into the system and observing the LSPR peak wavelength increase, which indicates the successful blocking process. The sensor was then ready for cortisol testing.

4.4.2 Cortisol Testing and Results

The cortisol testing was done by preparing 0.001, 0.01, 0.1, 1, 5, 10, 50, 100, 200, 500 and 1000 nM in PBS as mentioned in section 4.3.2. The cortisol solutions were injected into

the system at random orders, each allowed to interact with the sensing region for 10 minutes before flushing the system with PBS to remove the bound cortisol and prepare the sensing region for another test. The changes in the signal due the different cortisol concentrations were observed. The sensor displayed high sensitivity to the cortisol solution and excellent response against different cortisol concentrations as shown in Figure 55.

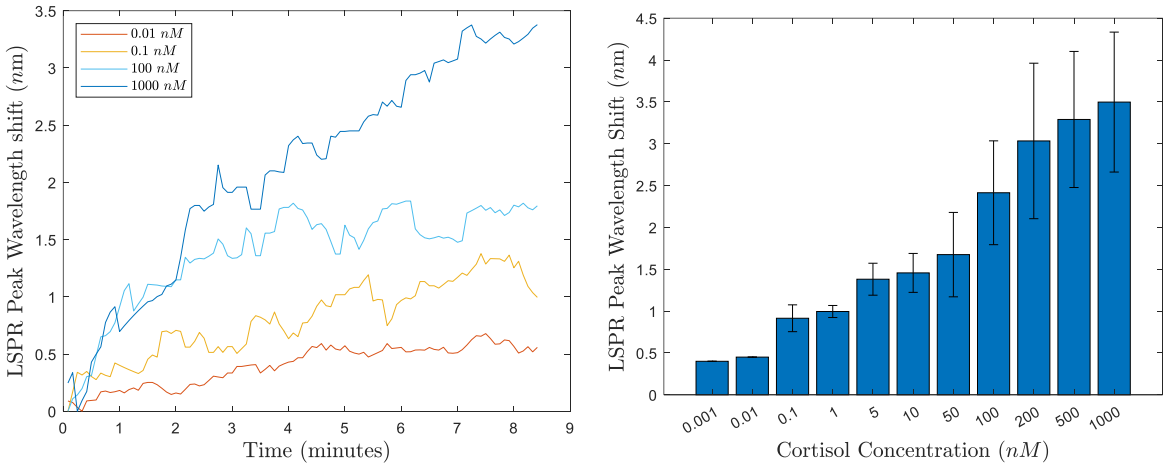


Figure 55 – (a) Sensor response due to different concentrations of cortisol (left) – (b) Average response of 5 sensors due to different cortisol concentrations (right)

Figure 55 (a) shows the response due to 4 concentrations (1000, 100, 0.1, and 0.01 nM). The remaining concentrations were omitted for clarity purposes. As shown in the figure, the highest cortisol concentration of 1000 nM resulted in the highest signal, while the 0.01 nM had the lowest. Five sensors were created following the same fabrication process. The sensors were tested with the same cortisol concentrations and the results are plotted in Figure 55 (b). Only one sensor was used to sense the lowest two concentration (0.001 and 0.01) nM. Based on the results obtained and presented in Figure 55 (b), the sensor displayed an excellent sensitivity of 0.0128 nm/nM. This provides a limit of detection of 0.1125 pM and a limit of

quantification of 0.3712 pM. The final resolution of the sensor was found to be 1.172 nM. Compared to similar sensors presented in Table 1, our sensor has improved sensitivity and limit of detection, due to the enhanced performance from coupling the evanescent wave and silver nanoparticles LSPR and optimizing the parameters contributing to the final characteristics.

After all concentrations were tested, the sensors were placed in PBS and put in a fridge at 4° overnight. Each sensor was tested the next day to study its shelf life, and the response was not ideal. The sensors reacted poorly to the first 2 concentrations tested (1000 nM, and 2500 nM), but then stopped reacting at all. This information suggests that the sensor has a short shelf life (<12 hours) and is most sensitive when used directly after fabrication. The reason for the short shelf life is still under investigation, however, preliminary research suggests that the effectiveness of the antibody in capturing the cortisol molecules degrades under prolonged testing in room temperature.

4.4.3 Model update and comparison

The Langmuir adsorption isotherm was updated based on an R_{max} value of 3.4973 nm and a K_D value of 51.3 nM found experimentally. The model obtained in section 3.5 was plotted against the experimental values in Figure 56. The results show a clear correlation between the model and experiment results. The higher discrepancies between the experimental results and the model at the lower concentrations can be attributed to human errors in pipetting the required volumes and performing the dilutions for the smaller concentrations in addition to the equipment noise. An offset of 0.4 nm was added to the model to account for the noise and the limit of quantification in our experiment. The experimental

results agree notably with the updated sensor response model presented in Figure 42. Adding to the validity of the modeling, fabrication, and testing approach presented in this thesis.

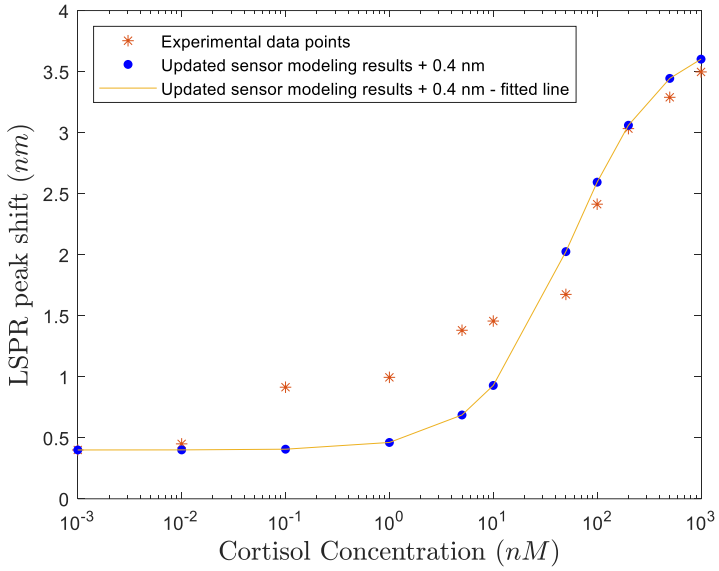


Figure 56 – Experimental results compared to updated sensor response model based on experimental refractive index sensitivity

Although the cortisol molecule size is remarkably smaller than the IgG antibody molecule size as mentioned in Chapter 2 which causes a minute change in the local refractive index around the nanoparticle, the enhanced performance of coupling FOEW sensing with silver nanoparticles LSPR proved to be sufficient for capturing this change, resulting in a sensitive cortisol biosensor with excellent characteristics capable of detecting cortisol concentrations found in saliva.

Chapter 5
Contributions, Future work, and Conclusions

5.1 Thesis Contributions

The main contributions of this thesis can be summarized as follows

1- **A new alternative approach for the analysis of FOEW-LSPR sensors that demonstrates that the main parameter affecting the sensor's performance is the absorption efficiency of the nanoparticles.** Studies in the literature that attempted to produce a model for this type of sensors considered the extinction coefficient of the nanoparticles [108], while other recent studies using evanescent wave based SPR sensors could not explain why their results show that only absorption is contributing to the signal [166]. Due to the nature of the evanescent wave, this electromagnetic wave which appears as if its propagating although it's not, can only be affected by an absorbing medium. An evanescent wave cannot be scattered, and the TIR of an uncladded fiber in a purely scattering medium is never attenuated.

2- **Proposed a new model that can predict the FOEW-LSPR based sensor signal based on nanoparticle absorption efficiency and adsorption process.** The current model can be extrapolated and used with different optical fibers geometry as well as nanoparticles of different materials, sizes, or shapes. This allows for the optimization of the optical fiber geometry and nanoparticles absorption for better sensor performance characteristics.

3- **Developed a novel pre-functionalization method of nanoparticles that allows for controlling the adsorption process using different MUA concentrations**. Experiments show a positive correlation between MUA concentration during the pre-functionalization step and the adsorption rate of nanoparticles. However, higher MUA concentrations result in a lower final surface density. This can be used to fine tune and control the adsorption process of the nanoparticles on glass surfaces, which can be important in many applications. Organic solvents like Dimethylsulfoxide (DMSO) can be used to avoid the side effects that OH^- groups, found in ethanol, have on silver.

4- **Designed, fabricated, and validated a new highly sensitive, accessible, cost-effective, and label-free salivary cortisol sensor using a coreless fiber as the sensing region.** The final sensor was sensitive enough to cover the range of cortisol concentration found in saliva, with a limit of detection and a resolution that can potentially transform non-invasive point-of-care cortisol monitoring. The fabrication method using a coreless fiber proved to be successful and simplifies the fabrication process significantly.

5.1.1 Manuscripts generated from this work

1- O. Awad, A. Ghannoum, P. Nieva, Tailoring Silver Nanoparticle Optical and Physical Parameters for Enhanced Fiber Optic Evanescent Wave Localized Surface Plasmon Resonance Sensor Performance. (Submitted April 2024, comments received June 2024)

2- O. Awad, P. Nieva, Controlling Nanoparticle Adsorption on Glass Surfaces through Pre-functionalization with Varying Concentrations of 11-Mercapto-undecanoic Acid (drafting stage)

3- O. Awad, P. Nieva, Design and Fabrication of a Fiber Optic Evanescent Wave LSPR Sensor for Salivary Cortisol: Optimization of Nanoparticle Size for higher Refractive Index Sensitivity (editing stage)

5.2 Future work

In this work, the size of the spherical silver nanoparticles used was optimized, but the shape was not considered. Further work includes the optimization of the nanoparticle shape for higher sensitivity as different shapes have shown significantly higher sensitivity compared to spherical [167]. Signal amplification can also be introduced through LSPR coupling methods. Although this will be a completely different sensing mechanism, it has shown to significantly enhance the sensitivity. Thus, it will be worth applying to the study of Cortisol sensing.

Factors affecting the functionalization and conjugation like pH level, temperature, and concentrations of chemicals used can also be optimized for higher conjugation yield, and higher quality SAMs. All these factors have been reported to have a significant effect on the final results, thus, more research and optimization experiments in this specific area will prove to be important. For instance, in this research, the buffer used had a 7.4 pH level, which is adequate for the functionalization, activation, and conjugation processes. However, it is not the ideal pH level for each one of these processes and in fact, EDC/NHS activation provides better results at pH levels closer to 6 pH.

Although the adsorption via self-assembly is an easy and scalable process, the sensors fabricated with this process can produce different results based on how they are handled afterwards. As mentioned, washing and drying the fiber would sometimes result in the aggregation of the particles and affects the signal. Finding ways to deposit the nanoparticles on the fiber surface in a precise manner or arrangement, optimize the direction of the deposition, or considering the use of lasers will increase the sensitivity of the sensor, the reliability, and the repeatability of the fabrication process.

Real saliva samples should be used for testing and signal correlation. However, saliva is a bodily fluid that can potentially contain harmful pathogens, and its use is restricted in our institution [168]. In addition, saliva is a complex biofluid that contains many biomarkers [169]. The success of this work in detecting pure cortisol in the salivary cortisol range do not imply that the sensor will work with real saliva samples. Testing with real saliva samples will impact the sensor's selectivity due to cross reactivity with other biomarkers. Selectivity issues can be addressed by enhancing the selectivity of the sensor using aptamers [10,170]. However, this topic is outside the scope of this work and will be addressed in future studies.

Finally, as the development of the salivary cortisol biosensor progresses toward potential commercialization, addressing the toxicity of silver nanoparticles will become a crucial consideration. Silver nanoparticles are known to exhibit toxic effects to cells primarily due to their ability to generate reactive oxygen species (ROS), which can induce oxidative stress, damage cellular membranes and DNA, and interfere with mitochondrial function. The exposure of saliva to silver nanoparticles could lead to the formation of a protein corona, where proteins adsorb onto the nanoparticle surface, potentially altering the sample's biochemical

composition [42]. This could compromise the accuracy of cortisol detection, either by masking the target analytes or inducing false positives/negatives, thus affecting the reliability of the biosensor. Human exposure, though unlikely during the use of this biosensor, could still present risks if nanoparticles leach from the device due to packaging defects. In addition, evaluating the environmental fate of silver nanoparticles, their degradation pathways, and potential bioaccumulation is essential for responsible commercialization.

5.3 Conclusions

In this work, an advanced analysis for enhancing the performance of a FOEW LSPR biosensors, fabricated via self-assembly of silver spherical nanoparticles and coreless fiber as a sensing region, was presented. Numerical and analytical models were used to optimize the fabrication and performance of the biosensor based on nanoparticles of different sizes. Using a combination of models including light-particle interaction, diffusion transport process, FOEW absorption, electromagnetic field decay, analyte-ligand interaction, and analyte refractive index, the sensor fabrication was optimized for higher LSPR absorption signal, higher refractive index sensitivity, shorter fabrication process time, higher surface density, and lower agglomeration.

Using a coreless fiber as a sensing region, UVO treatment for surface functionalization, and creating monolayers of silver nanoparticles through self-assembly are favorable fabrication approaches due to their simplicity and scalability. During the process of self-assembly, the smaller nanoparticles resulted in higher final surface density adsorbed on the sensing region for the same colloidal concentration. It was observed that smaller particles tend

to agglomerate less than larger particles after they adsorb on the surface. Higher surface density results in higher LSPR absorption signal, due to the evanescent field interacting with more nanoparticles. However, when the sensing region is fully covered, it was shown that the FOEW LSPR sensors fabricated using the nanoparticles with the highest absorption efficiency have the highest light absorption signal and refractive index sensitivity.

Experimental findings agreed well with the results obtained from the models and it was concluded that the main parameter affecting the performance of the FOEW LSPR sensor is the size of the nanoparticles, as it determines the absorption efficiency, the adsorption rate, the final surface density on the sensing region, and the refractive index sensitivity.

FOEW LSPR sensors fabricated via the process of self-assembly using 30 nm silver nanoparticles resulted in higher LSPR signal absorption and refractive index sensitivity, compared to other sizes. The models presented here can be easily modified to be used with different plasmonic materials, such as for example gold or copper, where it will be important to find the nanoparticle size that results in the highest LSPR absorption efficiency.

Functionalizing the silver nanoparticles surface for ligand conjugation employing the widely used MUA was not successful, due to the negative side effects that (OH^-) groups, which are found in ethanol, have on the silver. These groups have a higher affinity to silver than thiol groups, which affect the conjugation yield of the ligands on the nanoparticles surface. Due to the chemical structure of the IgG antibodies, using MUA also affects the orientation of the conjugated antibodies, resulting in less active sites for the analyte interaction. Additionally, the (OH^-) groups were reported to damage the silver surface due to oxidization which significantly affects the final sensor's sensitivity.

Cysteamine Hydrochloride was found to be a better functionalization reagent for ligand conjugation for the sensor presented in this work, as it can be diluted in water instead of ethanol, mitigating the negative effects of the (OH^-) groups on the silver nanoparticles. Functionalizing the silver surface with Cysteamine Hydrochloride results in a working sensor, which is also attributed to the higher conjugation yield of end-on orientation for the antibodies, resulting in more available active sites for the analyte.

The final sensor fabricated using Cysteamine Hydrochloride as a conjugation reagent displayed a sensitivity of 0.0128 nm/nM, with a limit of detection of 0.1125 pM, a resolution of 1.172 nM, and a quantification limit of 0.3712 pM. Although the shelf life was found to be short (<12 hours), the sensor's characteristics displayed were promising. Potentially allowing for the development of a highly accessible, inexpensive, sensitive, and non-invasive point-of-care salivary cortisol sensor that can be used in medical institutions, or at home by individuals monitoring their stress levels.

References

[1] L. Thau, J. Gandhi, and S. Sharma, “Physiology, Cortisol,” in *StatPearls*, Treasure Island (FL): StatPearls Publishing, 2023. Accessed: Jun. 09, 2023. [Online]. Available: http://www.ncbi.nlm.nih.gov/books/NBK538239/

[2] H. M. Burke, M. C. Davis, C. Otte, and D. C. Mohr, “Depression and cortisol responses to psychological stress: A meta-analysis,” *Psychoneuroendocrinology*, vol. 30, no. 9, Art. no. 9, Oct. 2005, doi: 10.1016/j.psyneuen.2005.02.010.

[3] E. Dziurkowska and M. Wesolowski, “Cortisol as a Biomarker of Mental Disorder Severity,” *J. Clin. Med.*, vol. 10, no. 21, p. 5204, Nov. 2021, doi: 10.3390/jcm10215204.

[4] L. D. Dorn, J. F. Lucke, T. L. Loucks, and S. L. Berga, “Salivary cortisol reflects serum cortisol: analysis of circadian profiles,” *Ann. Clin. Biochem.*, vol. 44, no. 3, Art. no. 3, May 2007, doi: 10.1258/000456307780480954.

[5] S. M. Smith and W. W. Vale, “The role of the hypothalamic-pituitary-adrenal axis in neuroendocrine responses to stress,” *Dialogues Clin. Neurosci.*, vol. 8, no. 4, pp. 383–395, Dec. 2006.

[6] T. Nagy, “Psychophysiological Responses to Distress and Eustress,” Eötvös Loránd Tudományegyetem, 2016. doi: 10.15476/ELTE.2015.120.

[7] N. El-Farhan, D. A. Rees, and C. Evans, “Measuring cortisol in serum, urine and saliva – are our assays good enough?,” *Ann. Clin. Biochem.*, vol. 54, no. 3, Art. no. 3, May 2017, doi: 10.1177/0004563216687335.

[8] J. G. Lewis and P. A. Elder, “An enzyme-linked immunosorbent assay (ELISA) for plasma cortisol,” *J. Steroid Biochem.*, vol. 22, no. 5, pp. 673–676, May 1985, doi: 10.1016/0022-4731(85)90222-5.

[9] “Cortisol Test: MedlinePlus Medical Test.” Accessed: Oct. 08, 2021. [Online]. Available: https://medlineplus.gov/lab-tests/cortisol-test/

[10] S. Jo *et al.*, “Localized surface plasmon resonance aptasensor for the highly sensitive direct detection of cortisol in human saliva,” *Sens. Actuators B Chem.*, vol. 304, p. 127424, Feb. 2020, doi: 10.1016/j.snb.2019.127424.

[11] “The Importance of Accurate Cortisol Testing to Understand Stress Levels,” Bingham Memorial Hospital. Accessed: Oct. 08, 2021. [Online]. Available: https://www.binghammemorial.org/health-news/importance-of-accurate-cortisol

[12] N. Ljubijankić, R. Popović-Javorić, S. Šćeta, A. Šapčanin, I. Tahirović, and E. Sofić, “DAILY FLUCTUATION OF CORTISOL IN THE SALIVA AND SERUM OF HEALTHY PERSONS,” *Bosn. J. Basic Med. Sci.*, vol. 8, no. 2, Art. no. 2, May 2008.

[13] C. W. le Roux, G. A. Chapman, W. M. Kong, W. S. Dhillo, J. Jones, and J. Alaghband-Zadeh, “Free Cortisol Index Is Better Than Serum Total Cortisol in Determining Hypothalamic-Pituitary-Adrenal Status in Patients Undergoing Surgery,” *J. Clin. Endocrinol. Metab.*, vol. 88, no. 5, Art. no. 5, May 2003, doi: 10.1210/jc.2002-021532.

[14] Q. Zhang, J. Dou, W. Gu, G. Yang, and J. Lu, “Reassessing the reliability of the salivary cortisol assay for the diagnosis of Cushing syndrome,” *J. Int. Med. Res.*, vol. 41, no. 5, Art. no. 5, Oct. 2013, doi: 10.1177/0300060513498017.

[15] R. A. Dressendörfer, C. Kirschbaum, W. Rohde, F. Stahl, and C. J. Strasburger, “Synthesis of a cortisol-biotin conjugate and evaluation as a tracer in an immunoassay for salivary cortisol measurement,” *J. Steroid Biochem. Mol. Biol.*, vol. 43, no. 7, pp. 683–692, Dec. 1992, doi: 10.1016/0960-0760(92)90294-S.

[16] M. Zangheri *et al.*, “A simple and compact smartphone accessory for quantitative chemiluminescence-based lateral flow immunoassay for salivary cortisol detection,” *Biosens. Bioelectron.*, vol. 64, pp. 63–68, Feb. 2015, doi: 10.1016/j.bios.2014.08.048.

[17] B. Sun *et al.*, “Investigate electrochemical immunosensor of cortisol based on gold nanoparticles/magnetic functionalized reduced graphene oxide,” *Biosens. Bioelectron.*, vol. 88, pp. 55–62, Feb. 2017, doi: 10.1016/j.bios.2016.07.047.

[18] Y.-H. Kim *et al.*, “Direct immune-detection of cortisol by chemiresistor graphene oxide sensor,” *Biosens. Bioelectron.*, vol. 98, pp. 473–477, Dec. 2017, doi: 10.1016/j.bios.2017.07.017.

[19] Kh. M. Sallam, “Preparation and development of solid phase radioimmunoassay system for determination of cortisol,” *J. Immunoassay Immunochem.*, vol. 38, no. 5, pp. 471–486, Sep. 2017, doi: 10.1080/15321819.2017.1331169.

[20] K. Gracie, S. Pang, G. M. Jones, K. Faulds, J. Braybrook, and D. Graham, “Detection of cortisol in serum using quantitative resonance Raman spectroscopy,” *Anal. Methods*, vol. 9, no. 10, pp. 1589–1594, Mar. 2017, doi: 10.1039/C6AY03296F.

[21] D. Y. Lee, E. Kim, and M. H. Choi, “Technical and clinical aspects of cortisol as a biochemical marker of chronic stress,” *BMB Rep.*, vol. 48, no. 4, pp. 209–216, Apr. 2015, doi: 10.5483/BMBRep.2015.48.4.275.

[22] J. E. L. Villa, I. Garcia, D. Jimenez de Aberasturi, V. Pavlov, M. D. P. T. Sotomayor, and L. M. Liz-Marzán, “SERS-based immunoassay for monitoring cortisol-related disorders,” *Biosens. Bioelectron.*, vol. 165, p. 112418, Oct. 2020, doi: 10.1016/j.bios.2020.112418.

[23] P. A. Kusov, Y. V. Kotelevtsev, and V. P. Drachev, “Cortisol Monitoring Devices toward Implementation for Clinically Relevant Biosensing In Vivo,” *Molecules*, vol. 28, no. 5, p. 2353, Mar. 2023, doi: 10.3390/molecules28052353.

[24] D. H. Hellhammer, S. Wüst, and B. M. Kudielka, “Salivary cortisol as a biomarker in stress research,” *Psychoneuroendocrinology*, vol. 34, no. 2, Art. no. 2, Feb. 2009, doi: 10.1016/j.psyneuen.2008.10.026.

[25] “Definition of biomarker - NCI Dictionary of Cancer Terms - NCI.” Accessed: Jul. 13, 2023. [Online]. Available: https://www.cancer.gov/publications/dictionaries/cancer-terms/def/biomarker

[26] L. Nicu and T. Leïchlé, “Biosensors and tools for surface functionalization from the macro- to the nanoscale: The way forward,” *J. Appl. Phys.*, vol. 104, no. 11, p. 111101, Dec. 2008, doi: 10.1063/1.2973147.

[27] V. R. Samuel and K. J. Rao, “A review on label free biosensors,” *Biosens. Bioelectron. X*, vol. 11, p. 100216, Sep. 2022, doi: 10.1016/j.biosx.2022.100216.

[28] R. Denomme, “A Label-Free Biosensor for Heat Shock Protein 70 Using Localized Surface Plasmon Resonance,” p. 102.

[29] J. S. Daniels and N. Pourmand, “Label-Free Impedance Biosensors: Opportunities and Challenges,” *Electroanalysis*, vol. 19, no. 12, pp. 1239–1257, Jun. 2007, doi: 10.1002/elan.200603855.

[30] M. A. Cooper, *Label-free biosensors: techniques and applications*. Cambridge; New York: Cambridge University Press, 2009. Accessed: Jun. 15, 2022. [Online]. Available: https://doi.org/10.1017/CBO9780511626531

[31] J. L. Hammond, N. Bhalla, S. D. Rafiee, and P. Estrela, “Localized Surface Plasmon Resonance as a Biosensing Platform for Developing Countries,” *Biosensors*, vol. 4, no. 2, Art. no. 2, Jun. 2014, doi: 10.3390/bios4020172.

[32] M. Quinten, *Optical Properties of Nanoparticle Systems: Mie and beyond*, 1st ed. Wiley, 2011. doi: 10.1002/9783527633135.

[33] K. Takemura, “Surface Plasmon Resonance (SPR)- and Localized SPR (LSPR)-Based Virus Sensing Systems: Optical Vibration of Nano- and Micro-Metallic Materials for the Development of Next-Generation Virus Detection Technology,” *Biosensors*, vol. 11, no. 8, p. 250, Jul. 2021, doi: 10.3390/bios11080250.

[34] J. M. Brockman, B. P. Nelson, and R. M. Corn, “Surface Plasmon Resonance Imaging Measurements of Ultrathin Organic Films,” *Annu. Rev. Phys. Chem.*, vol. 51, no. 1, pp. 41–63, Oct. 2000, doi: 10.1146/annurev.physchem.51.1.41.

[35] A. J. Haes and R. P. V. Duyne, “Nanoscale optical biosensors based on localized surface plasmon resonance spectroscopy,” in *Plasmonics: Metallic Nanostructures and Their Optical Properties*, SPIE, Oct. 2003, pp. 47–58. doi: 10.1117/12.508308.

[36] K. M. Mayer and J. H. Hafner, “Localized Surface Plasmon Resonance Sensors,” *Chem. Rev.*, vol. 111, no. 6, pp. 3828–3857, Jun. 2011, doi: 10.1021/cr100313v.

[37] P. Singh, “SPR Biosensors: Historical Perspectives and Current Challenges,” *Sens. Actuators B Chem.*, vol. 229, pp. 110–130, Jun. 2016, doi: 10.1016/j.snb.2016.01.118.

[38] “LSPR vs. SPR - Nicoya - Improving Human Life by Helping Scientists Succeed.” Accessed: Jun. 04, 2021. [Online]. Available: https://nicoyalife.com/nicoya-surface-plasmon-resonance-resources/what-is-spr/lspr-vs-spr-2/

[39] “What is the Difference Between SPR and LSPR,” Compare the Difference Between Similar Terms. Accessed: May 12, 2022. [Online]. Available: https://www.differencebetween.com/what-is-the-difference-between-spr-and-lspr/

[40] Y. Li, Q. Liao, W. Hou, and L. Qin, “Silver-Based Surface Plasmon Sensors: Fabrication and Applications,” *Int. J. Mol. Sci.*, vol. 24, no. 4, p. 4142, Feb. 2023, doi: 10.3390/ijms24044142.

[41] A. Loiseau, V. Asila, G. Boitel-Aullen, M. Lam, M. Salmain, and S. Boujday, “Silver-Based Plasmonic Nanoparticles for and Their Use in Biosensing,” *Biosensors*, vol. 9, no. 2, p. 78, Jun. 2019, doi: 10.3390/bios9020078.

[42] M. Noga, J. Milan, A. Frydrych, and K. Jurowski, “Toxicological Aspects, Safety Assessment, and Green Toxicology of Silver Nanoparticles (AgNPs)—Critical Review: State of the Art,” *Int. J. Mol. Sci.*, vol. 24, no. 6, p. 5133, Mar. 2023, doi: 10.3390/ijms24065133.

[43] A. K. Sharma, J. Gupta, and I. Sharma, “Fiber optic evanescent wave absorption-based sensors: A detailed review of advancements in the last decade (2007–18),” *Optik*, vol. 183, pp. 1008–1025, Apr. 2019, doi: 10.1016/j.ijleo.2019.02.104.

[44] A. Messica, A. Greenstein, and A. Katzir, “Theory of fiber-optic, evanescent-wave spectroscopy and sensors,” *Appl. Opt.*, vol. 35, no. 13, pp. 2274–2284, May 1996, doi: 10.1364/AO.35.002274.

[45] G. P. Anderson and C. R. Taitt, “Chapter 2 - EVANESCENT WAVE FIBER OPTIC BIOSENSORS,” in *Optical Biosensors (Second Edition)*, F. S. Ligler and C. R. Taitt, Eds., Amsterdam: Elsevier, 2008, pp. 83–138. doi: 10.1016/B978-044453125-4.50004-8.

[46] M. H. Weik, “Snell’s law,” in *Computer Science and Communications Dictionary*, M. H. Weik, Ed., Boston, MA: Springer US, 2001, pp. 1607–1607. doi: 10.1007/1-4020-0613-6_17633.

[47] F. de Fornel, *Evanescent Waves: From Newtonian Optics to Atomic Optics*. Springer Science & Business Media, 2001.

[48] M. Bertolotti, C. Sibilia, and A. M. Guzman, *Evanescent Waves in Optics: An Introduction to Plasmonics*, vol. 206. in Springer Series in Optical Sciences, vol. 206. Cham: Springer International Publishing, 2017. doi: 10.1007/978-3-319-61261-4.

[49] M. Milosevic, “On the Nature of the Evanescent Wave,” *Appl. Spectrosc.*, vol. 67, no. 2, Art. no. 2, Feb. 2013, doi: 10.1366/12-06707.

[50] P. S. Kumar, C. P. G. Vallabhan, V. P. N. Nampoori, V. N. S. Pillai, and P. Radhakrishnan, “A fibre optic evanescent wave sensor used for the detection of trace nitrites in water,” *J. Opt. Pure Appl. Opt.*, vol. 4, no. 3, p. 247, Mar. 2002, doi: 10.1088/1464-4258/4/3/305.

[51] P. Wang, G. Brambilla, M. Ding, Y. Semenova, Q. Wu, and G. Farrell, “High-sensitivity, evanescent field refractometric sensor based on a tapered, multimode fiber interference,” *Opt. Lett.*, vol. 36, no. 12, pp. 2233–2235, Jun. 2011, doi: 10.1364/OL.36.002233.

[52] S. K. Khijwania and B. D. Gupta, “Fiber optic evanescent field absorption sensor with high sensitivity and linear dynamic range,” *Opt. Commun.*, vol. 152, no. 4, pp. 259–262, Jul. 1998, doi: 10.1016/S0030-4018(98)00168-0.

[53] J. Satija, N. S. Punjabi, V. V. R. Sai, and S. Mukherji, “Optimal Design for U-bent Fiber-optic LSPR Sensor Probes,” *Plasmonics*, vol. 9, no. 2, pp. 251–260, Apr. 2014, doi: 10.1007/s11468-013-9618-7.

[54] A. Ghannoum, P. Nieva, A. Yu, and A. Khajepour, “Development of Embedded Fiber-Optic Evanescent Wave Sensors for Optical Characterization of Graphite Anodes in Lithium-Ion Batteries,” *ACS Appl. Mater. Interfaces*, vol. 9, no. 47, Art. no. 47, Nov. 2017, doi: 10.1021/acsami.7b13464.

[55] X. Xin, N. Zhong, Q. Liao, Y. Cen, R. Wu, and Z. Wang, “High-sensitivity four-layer polymer fiber-optic evanescent wave sensor,” *Biosens. Bioelectron.*, vol. 91, pp. 623–628, May 2017, doi: 10.1016/j.bios.2017.01.019.

[56] N. Zhong *et al.*, “A high-sensitivity fiber-optic evanescent wave sensor with a three-layer structure composed of Canada balsam doped with GeO2,” *Biosens. Bioelectron.*, vol. 85, pp. 876–882, Nov. 2016, doi: 10.1016/j.bios.2016.06.002.

[57] A. N. Chryssis, S. M. Lee, S. B. Lee, S. S. Saini, and M. Dagenais, "High sensitivity evanescent field fiber Bragg grating sensor," *IEEE Photonics Technol. Lett.*, vol. 17, no. 6, pp. 1253–1255, Jun. 2005, doi: 10.1109/LPT.2005.846953.

[58] D. Michel, F. Xiao, and K. Alameh, "A compact, flexible fiber-optic Surface Plasmon Resonance sensor with changeable sensor chips," *Sens. Actuators B Chem.*, vol. 246, pp. 258–261, Jul. 2017, doi: 10.1016/j.snb.2017.02.064.

[59] B. Miranda, I. Rea, P. Dardano, L. De Stefano, and C. Forestiere, "Recent Advances in the Fabrication and Functionalization of Flexible Optical Biosensors: Toward Smart Life-Sciences Applications," *Biosensors*, vol. 11, no. 4, p. 107, Apr. 2021, doi: 10.3390/bios11040107.

[60] J. G. Ortega-Mendoza, A. Padilla-Vivanco, C. Toxqui-Quitl, P. Zaca-Morán, D. Villegas-Hernández, and F. Chávez, "Optical Fiber Sensor Based on Localized Surface Plasmon Resonance Using Silver Nanoparticles Photodeposited on the Optical Fiber End," *Sensors*, vol. 14, no. 10, Art. no. 10, Oct. 2014, doi: 10.3390/s141018701.

[61] W. Putzbach and N. J. Ronkainen, "Immobilization Techniques in the Fabrication of Nanomaterial-Based Electrochemical Biosensors: A Review," *Sensors*, vol. 13, no. 4, pp. 4811–4840, Apr. 2013, doi: 10.3390/s130404811.

[62] M. E. Khosroshahi, R. Chabok, N. Chung, and Y. Patel, "Optimization of immersion direction and time of covalently self-assembled monolayer gold nanourchins on glass as SERS substrate," *J. Nanoparticle Res.*, vol. 25, no. 5, p. 97, May 2023, doi: 10.1007/s11051-023-05741-2.

[63] M. Oćwieja, Z. Adamczyk, M. Morga, and K. Kubiak, "Silver particle monolayers — Formation, stability, applications," *Adv. Colloid Interface Sci.*, vol. 222, pp. 530–563, Aug. 2015, doi: 10.1016/j.cis.2014.07.001.

[64] C. V. Restrepo and C. C. Villa, "Synthesis of silver nanoparticles, influence of capping agents, and dependence on size and shape: A review," *Environ. Nanotechnol. Monit. Manag.*, vol. 15, p. 100428, May 2021, doi: 10.1016/j.enmm.2021.100428.

[65] S. Paul, B. B. Chakraborty, S. Anwar, S. B. Paul, and S. Choudhury, "Self-assembly of silver nanoparticles through functionalization with coumarin-thiazole fused-ring thiol," *Heliyon*, vol. 6, no. 4, Art. no. 4, Apr. 2020, doi: 10.1016/j.heliyon.2020.e03674.

[66] A. Zarinwall, T. Waniek, R. Saadat, U. Braun, H. Sturm, and G. Garnweitner, "Comprehensive Characterization of APTES Surface Modifications of Hydrous Boehmite Nanoparticles," *Langmuir*, vol. 37, no. 1, pp. 171–179, Jan. 2021, doi: 10.1021/acs.langmuir.0c02682.

[67] J. A. Howarter and J. P. Youngblood, "Optimization of Silica Silanization by 3-Aminopropyltriethoxysilane," *Langmuir*, vol. 22, no. 26, pp. 11142–11147, Dec. 2006, doi: 10.1021/la061240g.

[68] R. Cao-Milán and L. M. Liz-Marzán, "Gold nanoparticle conjugates: recent advances toward clinical applications," *Expert Opin. Drug Deliv.*, vol. 11, no. 5, pp. 741–752, May 2014, doi: 10.1517/17425247.2014.891582.

[69] M. H. Jazayeri, H. Amani, A. A. Pourfatollah, H. Pazoki-Toroudi, and B. Sedighimoghaddam, "Various methods of gold nanoparticles (GNPs) conjugation to antibodies," *Sens. Bio-Sens. Res.*, vol. 9, pp. 17–22, Jul. 2016, doi: 10.1016/j.sbsr.2016.04.002.

[70] I. H. El-Sayed, X. Huang, and M. A. El-Sayed, “Surface Plasmon Resonance Scattering and Absorption of anti-EGFR Antibody Conjugated Gold Nanoparticles in Cancer Diagnostics: Applications in Oral Cancer,” *Nano Lett.*, vol. 5, no. 5, Art. no. 5, May 2005, doi: 10.1021/nl050074e.

[71] K. Sokolov *et al.*, “Real-Time Vital Optical Imaging of Precancer Using Anti-Epidermal Growth Factor Receptor Antibodies Conjugated to Gold Nanoparticles,” *Cancer Res.*, vol. 63, no. 9, Art. no. 9, May 2003.

[72] X. Huang, I. H. El-Sayed, W. Qian, and M. A. El-Sayed, “Cancer Cell Imaging and Photothermal Therapy in the Near-Infrared Region by Using Gold Nanorods,” *J. Am. Chem. Soc.*, vol. 128, no. 6, pp. 2115–2120, Feb. 2006, doi: 10.1021/ja057254a.

[73] Z.-P. Chen *et al.*, “A sensitive immunosensor using colloidal gold as electrochemical label,” *Talanta*, vol. 72, no. 5, pp. 1800–1804, Jul. 2007, doi: 10.1016/j.talanta.2007.02.020.

[74] Z. Grabarek and J. Gergely, “Zero-length crosslinking procedure with the use of active esters,” *Anal. Biochem.*, vol. 185, no. 1, pp. 131–135, Feb. 1990, doi: 10.1016/0003-2697(90)90267-D.

[75] C. Y. Lim *et al.*, “Succinimidyl Ester Surface Chemistry: Implications of the Competition between Aminolysis and Hydrolysis on Covalent Protein Immobilization,” *Langmuir*, vol. 30, no. 43, pp. 12868–12878, Nov. 2014, doi: 10.1021/la503439g.

[76] G. T. Hermanson, “Chapter 4 - Zero-Length Crosslinkers,” in *Bioconjugate Techniques (Third Edition)*, G. T. Hermanson, Ed., Boston: Academic Press, 2013, pp. 259–273. doi: 10.1016/B978-0-12-382239-0.00004-2.

[77] S. K. Srivastava, V. Arora, S. Sapra, and B. D. Gupta, “Localized Surface Plasmon Resonance-Based Fiber Optic U-Shaped Biosensor for the Detection of Blood Glucose,” *Plasmonics*, vol. 7, no. 2, Art. no. 2, Jun. 2012, doi: 10.1007/s11468-011-9302-8.

[78] J. Cao, M. H. Tu, T. Sun, and K. T. V. Grattan, “Wavelength-based localized surface plasmon resonance optical fiber biosensor,” *Sens. Actuators B Chem.*, vol. 181, pp. 611–619, May 2013, doi: 10.1016/j.snb.2013.02.052.

[79] S. Kumar, R. Singh, B. K. Kaushik, N. Chen, Q. S. Yang, and X. Zhang, “LSPR-Based Cholesterol Biosensor Using Hollow Core Fiber Structure,” *IEEE Sens. J.*, vol. 19, no. 17, pp. 7399–7406, Sep. 2019, doi: 10.1109/JSEN.2019.2916818.

[80] Y. Shao, S. Xu, X. Zheng, Y. Wang, and W. Xu, “Optical Fiber LSPR Biosensor Prepared by Gold Nanoparticle Assembly on Polyelectrolyte Multilayer,” *Sensors*, vol. 10, no. 4, Art. no. 4, Apr. 2010, doi: 10.3390/s100403585.

[81] S. Kumar *et al.*, “LSPR-based cholesterol biosensor using a tapered optical fiber structure,” *Biomed. Opt. Express*, vol. 10, no. 5, p. 2150, May 2019, doi: 10.1364/BOE.10.002150.

[82] P. Sharma, V. Semwal, and B. D. Gupta, “A highly selective LSPR biosensor for the detection of taurine realized on optical fiber substrate and gold nanoparticles,” *Opt. Fiber Technol.*, vol. 52, p. 101962, Nov. 2019, doi: 10.1016/j.yofte.2019.101962.

[83] P. Sharma, V. Semwal, and B. D. Gupta, “Highly sensitive and selective localized surface plasmon resonance biosensor for detecting glutamate realized on optical fiber substrate using gold nanoparticles,” *Photonics Nanostructures - Fundam. Appl.*, vol. 37, p. 100730, Dec. 2019, doi: 10.1016/j.photonics.2019.100730.

[84] D. Rithesh Raj, S. Prasanth, and C. Sudarsanakumar, “Development of LSPR-Based Optical Fiber Dopamine Sensor Using L-Tyrosine-Capped Silver Nanoparticles and Its Nonlinear Optical Properties,” *Plasmonics*, vol. 12, no. 4, pp. 1227–1234, Aug. 2017, doi: 10.1007/s11468-016-0380-5.

[85] D. Rithesh Raj, S. Prasanth, T. V. Vineeshkumar, and C. Sudarsanakumar, “Surface plasmon resonance based fiber optic dopamine sensor using green synthesized silver nanoparticles,” *Sens. Actuators B Chem.*, vol. 224, pp. 600–606, Mar. 2016, doi: 10.1016/j.snb.2015.10.106.

[86] W. Wang *et al.*, “A label-free fiber optic SPR biosensor for specific detection of C-reactive protein,” *Sci. Rep.*, vol. 7, no. 1, Art. no. 1, Dec. 2017, doi: 10.1038/s41598-017-17276-3.

[87] Y. Chen, Y. Yu, X. Li, H. Zhou, X. Hong, and Y. Geng, “Fiber-optic urine specific gravity sensor based on surface plasmon resonance,” *Sens. Actuators B Chem.*, vol. 226, pp. 412–418, Apr. 2016, doi: 10.1016/j.snb.2015.09.056.

[88] S. K. Srivastava, R. Verma, and B. D. Gupta, “Surface plasmon resonance based fiber optic glucose biosensor,” presented at the Asia Pacific Optical Sensors Conference, J. Canning and G. Peng, Eds., Sydney, Australia, Jan. 2012, p. 83511Z. doi: 10.1117/12.915978.

[89] D. Rithesh Raj and C. Sudarsanakumar, “Surface plasmon resonance based fiber optic sensor for the detection of cysteine using diosmin capped silver nanoparticles,” *Sens. Actuators Phys.*, vol. 253, pp. 41–48, Jan. 2017, doi: 10.1016/j.sna.2016.11.019.

[90] M. Sanders, Y. Lin, J. Wei, T. Bono, and R. G. Lindquist, “An enhanced LSPR fiber-optic nanoprobe for ultrasensitive detection of protein biomarkers,” *Biosens. Bioelectron.*, vol. 61, pp. 95–101, Nov. 2014, doi: 10.1016/j.bios.2014.05.009.

[91] H.-H. Jeong, S.-K. Lee, J.-H. Park, N. Erdene, and D.-H. Jeong, “Fabrication of fiber-optic localized surface plasmon resonance sensor and its application to detect antibody-antigen reaction of interferon-gamma,” *Opt. Eng.*, vol. 50, no. 12, p. 124405, Dec. 2011, doi: 10.1117/1.3662418.

[92] Q. Yang *et al.*, “Highly sensitive and selective sensor probe using glucose oxidase/gold nanoparticles/graphene oxide functionalized tapered optical fiber structure for detection of glucose,” *Optik*, vol. 208, p. 164536, Apr. 2020, doi: 10.1016/j.ijleo.2020.164536.

[93] C.-Y. Chiang, M.-L. Hsieh, K.-W. Huang, L.-K. Chau, C.-M. Chang, and S.-R. Lyu, “Fiber-optic particle plasmon resonance sensor for detection of interleukin-1β in synovial fluids,” *Biosens. Bioelectron.*, vol. 26, no. 3, pp. 1036–1042, Nov. 2010, doi: 10.1016/j.bios.2010.08.047.

[94] K. Li, G. Liu, Y. Wu, P. Hao, W. Zhou, and Z. Zhang, “Gold nanoparticle amplified optical microfiber evanescent wave absorption biosensor for cancer biomarker detection in serum,” *Talanta*, vol. 120, pp. 419–424, Mar. 2014, doi: 10.1016/j.talanta.2013.11.085.

[95] N. Polley, S. Basak, R. Hass, and C. Pacholski, “Fiber optic plasmonic sensors: Providing sensitive biosensor platforms with minimal lab equipment,” *Biosens. Bioelectron.*, vol. 132, pp. 368–374, May 2019, doi: 10.1016/j.bios.2019.03.020.

[96] J. M. Gérardy and M. Ausloos, “Absorption spectrum of clusters of spheres from the general solution of Maxwell’s equations. II. Optical properties of aggregated metal spheres,” *Phys. Rev. B*, vol. 25, no. 6, pp. 4204–4229, Mar. 1982, doi: 10.1103/PhysRevB.25.4204.

[97] W.-T. Wu, C.-H. Chen, C.-Y. Chiang, and L.-K. Chau, “Effect of Surface Coverage of Gold Nanoparticles on the Refractive Index Sensitivity in Fiber-Optic Nanoplasmonic Sensing,” *Sensors*, vol. 18, no. 6, Art. no. 6, Jun. 2018, doi: 10.3390/s18061759.

[98] K. A. Willets and R. P. Van Duyne, “Localized Surface Plasmon Resonance Spectroscopy and Sensing,” *Annu. Rev. Phys. Chem.*, vol. 58, no. 1, Art. no. 1, May 2007, doi: 10.1146/annurev.physchem.58.032806.104607.

[99] C. F. Bohren and D. R. Huffman, *Absorption and Scattering of Light by Small Particles*, 1st ed. Wiley, 1998. doi: 10.1002/9783527618156.

[100] Y. Jiang, S. Pillai, and M. A. Green, “Realistic Silver Optical Constants for Plasmonics,” *Sci. Rep.*, vol. 6, no. 1, Art. no. 1, Jul. 2016, doi: 10.1038/srep30605.

[101] P. B. Johnson and R. W. Christy, “Optical Constants of the Noble Metals,” *Phys. Rev. B*, vol. 6, no. 12, Art. no. 12, Dec. 1972, doi: 10.1103/PhysRevB.6.4370.

[102] E. D. Palik, *Handbook of Optical Constants of Solids*. Academic Press, 1998.

[103] M. Oćwieja, Z. Adamczyk, and K. Kubiak, “Tuning properties of silver particle monolayers via controlled adsorption–desorption processes,” *J. Colloid Interface Sci.*, vol. 376, no. 1, Art. no. 1, Jun. 2012, doi: 10.1016/j.jcis.2012.02.017.

[104] D. S. dos Santos Jr., R. C. Sanfelice, R. Alvarez-Puebla, O. N. Oliveira Jr., and R. F. Aroca, “Optical Enhancing Properties in Layer-by-Layer Films of Dendrimer and Gold Nanoparticles,” *Macromol. Symp.*, vol. 245–246, no. 1, pp. 325–329, 2006, doi: 10.1002/masy.200651344.

[105] M. Morga, Z. Adamczyk, and M. Oćwieja, “Stability of silver nanoparticle monolayers determined by in situ streaming potential measurements,” *J. Nanoparticle Res.*, vol. 15, no. 11, Art. no. 11, Nov. 2013, doi: 10.1007/s11051-013-2076-5.

[106] V. Ruddy, B. D. MacCraith, and J. A. Murphy, “Evanescent wave absorption spectroscopy using multimode fibers,” *J. Appl. Phys.*, vol. 67, no. 10, Art. no. 10, May 1990, doi: 10.1063/1.346085.

[107] A. Mason, S. C. Mukhopadhyay, and K. P. Jayasundera, Eds., *Sensing Technology: Current Status and Future Trends III*, vol. 11. in Smart Sensors, Measurement and Instrumentation, vol. 11. Cham: Springer International Publishing, 2015. doi: 10.1007/978-3-319-10948-0.

[108] V. V. R. Sai, T. Kundu, and S. Mukherji, “Novel U-bent fiber optic probe for localized surface plasmon resonance based biosensor,” *Biosens. Bioelectron.*, vol. 24, no. 9, Art. no. 9, May 2009, doi: 10.1016/j.bios.2009.02.007.

[109] “Random sequential adsorption,” *J. Theor. Biol.*, vol. 87, no. 2, pp. 237–254, Nov. 1980, doi: 10.1016/0022-5193(80)90358-6.

[110] T. A. Roni, R. Hassan, and M. Faisal, “Dual-Side Polished SPR Biosensor with Wide Sensing Range,” in *2020 11th International Conference on Electrical and Computer Engineering (ICECE)*, Dec. 2020, pp. 487–490. doi: 10.1109/ICECE51571.2020.9393102.

[111] Md. S. Islam *et al.*, “Dual-polarized highly sensitive plasmonic sensor in the visible to near-IR spectrum,” *Opt. Express*, vol. 26, no. 23, p. 30347, Nov. 2018, doi: 10.1364/OE.26.030347.

[112] S. M. Tariq, M. A. Fakhri, E. T. Salim, U. Hashim, and F. H. Alsultany, “Design of an unclad single-mode fiber-optic biosensor based on localized surface plasmon resonance by using COMSOL Multiphysics 5.1 finite element method,” *Appl. Opt.*, vol. 61, no. 21, p. 6257, Jul. 2022, doi: 10.1364/AO.458175.

[113] J. W. Gooch, “Sellmeier Equation,” in *Encyclopedic Dictionary of Polymers*, J. W. Gooch, Ed., New York, NY: Springer, 2011, pp. 653–654. doi: 10.1007/978-1-4419-6247-8_10447.

[114] R. A. Kadhim, L. Yuan, H. Xu, J. Wu, and Z. Wang, “Highly Sensitive D-Shaped Optical Fiber Surface Plasmon Resonance Refractive Index Sensor Based on Ag-α-Fe2O3 Grating,” *IEEE Sens. J.*, vol. 20, no. 17, pp. 9816–9824, Sep. 2020, doi: 10.1109/JSEN.2020.2992854.

[115] B. Ung and Y. Sheng, “Interference of surface waves in a metallic nanoslit,” *Opt. Express*, vol. 15, no. 3, pp. 1182–1190, Feb. 2007, doi: 10.1364/OE.15.001182.

[116] “Bora Ung (2022). Drude-Lorentz and Debye-Lorentz models for the dielectric constant of metals and water (https://www.mathworks.com/matlabcentral/fileexchange/18040-drude-lorentz-and-debye-lorentz-models-for-the-dielectric-constant-of-metals-and-water), MATLAB Central File Exchange. Retrieved November 28, 2022.”

[117] “The Electromagnetic Waves, Frequency Domain Interface.” Accessed: Jan. 11, 2024. [Online]. Available: https://doc.comsol.com/5.5/doc/com.comsol.help.woptics/woptics_ug_optics.6.02.html

[118] A. Hassani and M. Skorobogatiy, “Design criteria for microstructured-optical-fiber-based surface-plasmon-resonance sensors,” *J. Opt. Soc. Am. B*, vol. 24, no. 6, p. 1423, Jun. 2007, doi: 10.1364/JOSAB.24.001423.

[119] M. Chauhan and V. Kumar Singh, “Review on recent experimental SPR/LSPR based fiber optic analyte sensors,” *Opt. Fiber Technol.*, vol. 64, p. 102580, Jul. 2021, doi: 10.1016/j.yofte.2021.102580.

[120] Y. H. Tan, M. Liu, B. Nolting, J. G. Go, J. Gervay-Hague, and G. Liu, “A Nanoengineering Approach for Investigation and Regulation of Protein Immobilization,” *ACS Nano*, vol. 2, no. 11, pp. 2374–2384, Nov. 2008, doi: 10.1021/nn800508f.

[121] V. R. Sarma, E. W. Silverton, D. R. Davies, and W. D. Terry, “The Three-Dimensional Structure at 6 A Resolution of a Human γG1 Immunoglobulin Molecule,” *J. Biol. Chem.*, vol. 246, no. 11, pp. 3753–3759, Jun. 1971, doi: 10.1016/S0021-9258(18)62192-1.

[122] J. Buijs, J. W. Th. Lichtenbelt, W. Norde, and J. Lyklema, “Adsorption of monoclonal IgGs and their F(ab′)2 fragments onto polymeric surfaces,” *Colloids Surf. B Biointerfaces*, vol. 5, no. 1–2, pp. 11–23, Sep. 1995, doi: 10.1016/0927-7765(95)98205-2.

[123] C. Zhou *et al.*, “Human Immunoglobulin Adsorption Investigated by Means of Quartz Crystal Microbalance Dissipation, Atomic Force Microscopy, Surface Acoustic Wave, and Surface Plasmon Resonance Techniques,” *Langmuir*, vol. 20, no. 14, pp. 5870–5878, Jul. 2004, doi: 10.1021/la036251d.

[124] N. Welch, J. Scoble, B. Muir, and P. Pigram, “Orientation and characterization of immobilized antibodies for improved immunoassays (Review),” *Biointerphases*, vol. 12, p. 02D301, Jun. 2017, doi: 10.1116/1.4978435.

[125] G. Ruiz, K. Tripathi, S. Okyem, and J. D. Driskell, “pH Impacts the Orientation of Antibody Adsorbed onto Gold Nanoparticles,” *Bioconjug. Chem.*, vol. 30, no. 4, pp. 1182–1191, Apr. 2019, doi: 10.1021/acs.bioconjchem.9b00123.

[126] M. E. Khosroshahi, R. Chabok, and N. Chung, “Glass-Based Nanobiosensor Immobilized with Oriented Antibody-Conjugated Gold Nanourchin for Targeted Detection of Breast Cancer

Biomarker in Serum Using FT-NIR and SERS," *Plasmonics*, vol. 18, no. 6, pp. 2155–2176, Dec. 2023, doi: 10.1007/s11468-023-01929-3.

[127] "Kinetic Analysis of Biosensor".

[128] C. Zhou *et al.*, "Human Immunoglobulin Adsorption Investigated by Means of Quartz Crystal Microbalance Dissipation, Atomic Force Microscopy, Surface Acoustic Wave, and Surface Plasmon Resonance Techniques," *Langmuir*, vol. 20, no. 14, pp. 5870–5878, Jul. 2004, doi: 10.1021/la036251d.

[129] "Evaluation of a Three-Dimensional Micromixer in a Surface-Based Biosensor | Langmuir." Accessed: May 14, 2024. [Online]. Available: https://pubs.acs.org/doi/10.1021/la0262250

[130] G. Hu, Y. Gao, and D. Li, "Modeling micropatterned antigen–antibody binding kinetics in a microfluidic chip," *Biosens. Bioelectron.*, vol. 22, no. 7, pp. 1403–1409, Feb. 2007, doi: 10.1016/j.bios.2006.06.017.

[131] M. Frasconi, M. Mazzarino, F. Botrè, and F. Mazzei, "Surface plasmon resonance immunosensor for cortisol and cortisone determination," *Anal. Bioanal. Chem.*, vol. 394, no. 8, pp. 2151–2159, Aug. 2009, doi: 10.1007/s00216-009-2914-6.

[132] N. Dhull, G. Kaur, V. Gupta, and M. Tomar, "Highly sensitive and non-invasive electrochemical immunosensor for salivary cortisol detection," *Sens. Actuators B Chem.*, vol. 293, pp. 281–288, Aug. 2019, doi: 10.1016/j.snb.2019.05.020.

[133] J. A. De Feijter, J. Benjamins, and F. A. Veer, "Ellipsometry as a tool to study the adsorption behavior of synthetic and biopolymers at the air–water interface," *Biopolymers*, vol. 17, no. 7, pp. 1759–1772, Jul. 1978, doi: 10.1002/bip.1978.360170711.

[134] Z. Fan *et al.*, "UV/Ozone-Assisted Rapid Formation of High-Quality Tribological Self-Assembled Monolayer," *Coatings*, vol. 9, no. 11, Art. no. 11, Nov. 2019, doi: 10.3390/coatings9110762.

[135] H. Lü, W. Yan, Z. Liu, and J. Li, "[Hydrophilic Surface Modification of Polydimethylsiloxane with UV/Ozone Treatment]," *Guang Pu Xue Yu Guang Pu Fen Xi Guang Pu*, vol. 36, no. 4, pp. 1033–1037, Apr. 2016.

[136] H. Wang, B. Yu, S. Jiang, L. Jiang, and L. Qian, "UV/ozone-assisted tribochemistry-induced nanofabrication on Si(100) surfaces," *RSC Adv.*, vol. 7, no. 63, pp. 39651–39656, Aug. 2017, doi: 10.1039/C7RA07198A.

[137] "2. UV-Ozone Cleaning for Removal of Surface Contaminants - Knovel." Accessed: Jul. 07, 2021. [Online]. Available: https://app-knovel-com.proxy.lib.uwaterloo.ca/web/view/khtml/show.v/rcid:kpDSCCVCT1/cid:kt00U9CIE1/viewerType:khtml//root_slug:2-uv-ozone-cleaning-for-removal-of-surface-contaminants/url_slug:uv-ozone-cleaning-removal?kpromoter=federation&b-toc-cid=kpDSCCVCT1&b-toc-root-slug=&b-toc-url-slug=uv-ozone-cleaning-removal&b-toc-title=Developments%20in%20Surface%20Contamination%20and%20Cleaning%2C%20Volume%208%20-%20Cleaning%20Techniques&page=1&view=collapsed&zoom=1

[138] P. J. Rivero, J. Goicoechea, and F. J. Arregui, "Localized Surface Plasmon Resonance for Optical Fiber-Sensing Applications," in *Nanoplasmonics - Fundamentals and Applications*, G. Barbillon, Ed., InTech, 2017. doi: 10.5772/67544.

[139] M. Sypabekova, A. Hagemann, D. Rho, and S. Kim, “Review: 3-Aminopropyltriethoxysilane (APTES) Deposition Methods on Oxide Surfaces in Solution and Vapor Phases for Biosensing Applications,” *Biosensors*, vol. 13, no. 1, Art. no. 1, Jan. 2023, doi: 10.3390/bios13010036.

[140] R. Bochert, “Contribution to comprehension of image formation in confocal microscopy of cornea with Rostock cornea module,” *Br. J. Ophthalmol.*, vol. 89, no. 10, pp. 1351–1355, Oct. 2005, doi: 10.1136/bjo.2004.063743.

[141] J. Chen *et al.*, “Optimization and Application of Reflective LSPR Optical Fiber Biosensors Based on Silver Nanoparticles,” *Sensors*, vol. 15, no. 6, Art. no. 6, Jun. 2015, doi: 10.3390/s150612205.

[142] Q. Zhao, R. Duan, J. Yuan, Y. Quan, H. Yang, and M. Xi, “A reusable localized surface plasmon resonance biosensor for quantitative detection of serum squamous cell carcinoma antigen in cervical cancer patients based on silver nanoparticles array,” *Int. J. Nanomedicine*, vol. 9, pp. 1097–1104, Feb. 2014, doi: 10.2147/IJN.S58499.

[143] G. I. Sakellari, N. Hondow, and P. H. E. Gardiner, “Factors Influencing the Surface Functionalization of Citrate Stabilized Gold Nanoparticles with Cysteamine, 3-Mercaptopropionic Acid or l-Selenocystine for Sensor Applications,” *Chemosensors*, vol. 8, no. 3, Art. no. 3, Sep. 2020, doi: 10.3390/chemosensors8030080.

[144] T. Kamra, S. Chaudhary, C. Xu, L. Montelius, J. Schnadt, and L. Ye, “Covalent immobilization of molecularly imprinted polymer nanoparticles on a gold surface using carbodiimide coupling for chemical sensing,” *J. Colloid Interface Sci.*, vol. 461, pp. 1–8, Jan. 2016, doi: 10.1016/j.jcis.2015.09.009.

[145] H.-M. Kim, M. Uh, D. H. Jeong, H.-Y. Lee, J.-H. Park, and S.-K. Lee, “Localized surface plasmon resonance biosensor using nanopatterned gold particles on the surface of an optical fiber,” *Sens. Actuators B Chem.*, vol. 280, pp. 183–191, Feb. 2019, doi: 10.1016/j.snb.2018.10.059.

[146] J. W. Lee, S. J. Sim, S. M. Cho, and J. Lee, “Characterization of a self-assembled monolayer of thiol on a gold surface and the fabrication of a biosensor chip based on surface plasmon resonance for detecting anti-GAD antibody,” *Biosens. Bioelectron.*, vol. 20, no. 7, pp. 1422–1427, Jan. 2005, doi: 10.1016/j.bios.2004.04.017.

[147] E. C. A. Stigter, G. J. de Jong, and W. P. van Bennekom, “An improved coating for the isolation and quantitation of interferon-gamma in spiked plasma using surface plasmon resonance (SPR),” *Biosens. Bioelectron.*, vol. 21, no. 3, pp. 474–482, Sep. 2005, doi: 10.1016/j.bios.2004.11.008.

[148] K. L. Brogan and M. H. Schoenfisch, “Influence of antibody immobilization strategy on molecular recognition force microscopy measurements,” *Langmuir ACS J. Surf. Colloids*, vol. 21, no. 7, pp. 3054–3060, Mar. 2005, doi: 10.1021/la047922q.

[149] N. Patel *et al.*, “Immobilization of Protein Molecules onto Homogeneous and Mixed Carboxylate-Terminated Self-Assembled Monolayers,” *Langmuir*, vol. 13, no. 24, pp. 6485–6490, Nov. 1997, doi: 10.1021/la970933h.

[150] J. W. Chung, R. Bernhardt, and J. C. Pyun, “Sequential analysis of multiple analytes using a surface plasmon resonance (SPR) biosensor,” *J. Immunol. Methods*, vol. 311, no. 1–2, pp. 178–188, Apr. 2006, doi: 10.1016/j.jim.2006.02.003.

[151] M.-G. Kim, Y.-B. Shin, J.-M. Jung, H.-S. Ro, and B. H. Chung, “Enhanced sensitivity of surface plasmon resonance (SPR) immunoassays using a peroxidase-catalyzed precipitation reaction and its application to a protein microarray,” *J. Immunol. Methods*, vol. 297, no. 1–2, pp. 125–132, Feb. 2005, doi: 10.1016/j.jim.2004.12.007.

[152] H. J. Lee, D. Nedelkov, and R. M. Corn, “Surface plasmon resonance imaging measurements of antibody arrays for the multiplexed detection of low molecular weight protein biomarkers,” *Anal. Chem.*, vol. 78, no. 18, pp. 6504–6510, Sep. 2006, doi: 10.1021/ac060881d.

[153] A. Kausaite *et al.*, “Surface plasmon resonance label-free monitoring of antibody antigen interactions in real time,” *Biochem. Mol. Biol. Educ. Bimon. Publ. Int. Union Biochem. Mol. Biol.*, vol. 35, no. 1, pp. 57–63, Jan. 2007, doi: 10.1002/bmb.22.

[154] F. C. Marques, G. P. Oliveira, R. A. R. Teixeira, R. M. S. Justo, T. B. V. Neves, and G. F. S. Andrade, “Characterization of 11-mercaptoundecanoic and 3-mercaptopropionic acids adsorbed on silver by surface-enhanced Raman scattering,” *Vib. Spectrosc.*, vol. 98, pp. 139–144, Sep. 2018, doi: 10.1016/j.vibspec.2018.07.015.

[155] A. Karabchevsky, L. Tsapovsky, R. S. Marks, and I. Abdulhalim, “Study of Immobilization Procedure on Silver Nanolayers and Detection of Estrone with Diverged Beam Surface Plasmon Resonance (SPR) Imaging,” *Biosensors*, vol. 3, no. 1, Art. no. 1, Mar. 2013, doi: 10.3390/bios3010157.

[156] B.-K. Oh, Y.-K. Kim, W. Lee, Y. M. Bae, W. H. Lee, and J.-W. Choi, “Immunosensor for detection of Legionella pneumophila using surface plasmon resonance,” *Biosens. Bioelectron.*, vol. 18, no. 5–6, pp. 605–611, May 2003, doi: 10.1016/S0956-5663(03)00032-0.

[157] B.-K. Oh, Y.-K. Kim, K. W. Park, W. H. Lee, and J.-W. Choi, “Surface plasmon resonance immunosensor for the detection of Salmonella typhimurium,” *Biosens. Bioelectron.*, vol. 19, no. 11, pp. 1497–1504, Jun. 2004, doi: 10.1016/j.bios.2003.12.009.

[158] N. C. Martin *et al.*, “The use of phosphate buffered saline for the recovery of cells and spermatozoa from swabs,” *Sci. Justice J. Forensic Sci. Soc.*, vol. 46, no. 3, pp. 179–184, 2006, doi: 10.1016/S1355-0306(06)71591-X.

[159] M. N. Noorhashimah, K. A. Razak, and Z. Lockman, “Effect of Concentration and pH of PBS to the Electrocatalytic Performance of Enzymatic Glucose Biosensor,” *Solid State Phenom.*, vol. 290, pp. 193–198, 2019, doi: 10.4028/www.scientific.net/SSP.290.193.

[160] C. Menti, J. A. Henriques, F. Missell, and M. Roesch-Ely, “Antibody-based magneto-elastic biosensors: potential devices for detection of pathogens and associated toxins,” *Appl. Microbiol. Biotechnol.*, vol. 100, Jul. 2016, doi: 10.1007/s00253-016-7624-3.

[161] J. Charles A Janeway, P. Travers, M. Walport, and M. J. Shlomchik, “The structure of a typical antibody molecule,” in *Immunobiology: The Immune System in Health and Disease. 5th edition*, Garland Science, 2001. Accessed: May 28, 2024. [Online]. Available: https://www.ncbi.nlm.nih.gov/books/NBK27144/

[162] B. Saha, T. H. Evers, and M. W. J. Prins, “How Antibody Surface Coverage on Nanoparticles Determines the Activity and Kinetics of Antigen Capturing for Biosensing,” *Anal. Chem.*, vol. 86, no. 16, pp. 8158–8166, Aug. 2014, doi: 10.1021/ac501536z.

[163] M. S. Soares *et al.*, “Immunosensing Based on Optical Fiber Technology: Recent Advances,” *Biosensors*, vol. 11, no. 9, p. 305, Aug. 2021, doi: 10.3390/bios11090305.

[164] C. Leitão *et al.*, “Cortisol In-Fiber Ultrasensitive Plasmonic Immunosensing,” *IEEE Sens. J.*, vol. 21, no. 3, pp. 3028–3034, Feb. 2021, doi: 10.1109/JSEN.2020.3025456.

[165] C. Leitão *et al.*, “Cortisol AuPd plasmonic unclad POF biosensor,” *Biotechnol. Rep.*, vol. 29, p. e00587, Mar. 2021, doi: 10.1016/j.btre.2021.e00587.

[166] M. Habibi Masheli, S. Eyvazi, M. Aghdaee, and J. M. Amjad, “LSPR of Nanoparticles Inside Strong Absorbent Medium,” *J. Phys. Chem. C*, vol. 127, no. 49, pp. 23696–23705, Dec. 2023, doi: 10.1021/acs.jpcc.3c04682.

[167] “Time-resolved spectroscopic and SERS characterization of plasmonic optical fiber sensor using glutathione-capped gold nanourchins for detection of lead in water,” CoLab. Accessed: Aug. 27, 2024. [Online]. Available: https://colab.ws/articles/10.1007%2Fs13404-024-00350-w

[168] “Biosafety | Safety Office.” Accessed: Aug. 29, 2024. [Online]. Available: https://uwaterloo.ca/safety-office/laboratory-safety/biosafety

[169] L. Trevisan França de Lima, J. Müller Bark, M. Rasheduzzaman, C. Ekanayake Weeramange, and C. Punyadeera, “Chapter 10 - Saliva as a matrix for measurement of cancer biomarkers,” in *Cancer Biomarkers*, L. V. Ramanathan, M. Fleisher, and M. J. Duffy, Eds., in Clinical Aspects and Laboratory Determination. , Elsevier, 2022, pp. 297–351. doi: 10.1016/B978-0-12-824302-2.00008-4.

[170] Y. Liu, H. Yu, O. Alkhamis, J. Moliver, and Y. Xiao, “Tuning Biosensor Cross-Reactivity Using Aptamer Mixtures,” *Anal. Chem.*, vol. 92, no. 7, pp. 5041–5047, Apr. 2020, doi: 10.1021/acs.analchem.9b05339.

Appendix A

Table 11 – COMSOL MULTIPHYSICS FOEW LSPR modeling parameters

Parameter	Expression	Value	Description
$coreless_r$	$62.5[\mu m]$	$6.25E-5\ m$	Radius of coreless fiber
ag_d	$30[nm]$	$3E-8\ m$	Silver Nanoparticle Diameter
$a1_{clad}$	0.6961663	0.69617	Sellmeier equation variable
$a2_{clad}$	0.4079426	0.40794	Sellmeier equation variable
$a3_{clad}$	0.8974794	0.89748	Sellmeier equation variable
$b1_{clad}$	$0.0684043[\mu m]$	$6.8404E-8\ m$	Sellmeier equation variable
$b2_{clad}$	$0.1162414[\mu m]$	$1.1624E-7\ m$	Sellmeier equation variable
$b3_{clad}$	$9.896161[\mu m]$	$9.8962E-6\ m$	Sellmeier equation variable
$ehbar$	$e_const/hbar_const$	$1.5193E15\ s^2 \cdot A/(kg \cdot m^2)$	planks constant in rad/ev.s
$omegap$	$9.01[(kg*m\text{^}2)/(s\text{^}3*A)]*ehbar$	$1.3689E16\ 1/s$	plasma frequency in rad/s
$f1$	0.845	0.845	Oscillators' strength term
$f2$	0.065	0.065	Oscillators' strength term
$f3$	0.124	0.124	Oscillators' strength term
$f4$	0.011	0.011	Oscillators' strength term
$f5$	0.840	0.84	Oscillators' strength term
$f6$	5.646	5.646	Oscillators' strength term
$g1$	$0.048[(kg*m\text{^}2)/(s\text{^}3*A)]*ehbar$	$7.2925E13\ 1/s$	Damping frequency of each oscillator
$g2$	$3.886[(kg*m\text{^}2)/(s\text{^}3*A)]*ehbar$	$5.9039E15\ 1/s$	Damping frequency of each oscillator
$g3$	$0.452[(kg*m\text{^}2)/(s\text{^}3*A)]*ehbar$	$6.8671E14\ 1/s$	Damping frequency of each oscillator
$g4$	$0.065[(kg*m\text{^}2)/(s\text{^}3*A)]*ehbar$	$9.8752E13\ 1/s$	Damping frequency of each oscillator
$g5$	$0.916[(kg*m\text{^}2)/(s\text{^}3*A)]*ehbar$	$1.3916E15\ 1/s$	Damping frequency of each oscillator
$g6$	$2.419[(kg*m\text{^}2)/(s\text{^}3*A)]*ehbar$	$3.6751E15\ 1/s$	Damping frequency of each oscillator
$omega1$	$0.000[(kg*m\text{^}2)/(s\text{^}3*A)]*ehbar$	$0\ 1/s$	Resonance frequency of each oscillator
$omega2$	$0.816[(kg*m\text{^}2)/(s\text{^}3*A)]*ehbar$	$1.2397E15\ 1/s$	Resonance frequency of each oscillator
$omega3$	$4.481[(kg*m\text{^}2)/(s\text{^}3*A)]*ehbar$	$6.8078E15\ 1/s$	Resonance frequency of each oscillator
$omega4$	$8.185[(kg*m\text{^}2)/(s\text{^}3*A)]*ehbar$	$1.2435E16\ 1/s$	Resonance frequency of each oscillator
$omega5$	$9.083[(kg*m\text{^}2)/(s\text{^}3*A)]*ehbar$	$1.38E16\ 1/s$	Resonance frequency of each oscillator
$omega6$	$20.29[(kg*m\text{^}2)/(s\text{^}3*A)]*ehbar$	$3.0826E16\ 1/s$	Resonance frequency of each oscillator

Table 12 – COMSOL MULTIPHYSICS FOEW LSPR modeling variables

Parameter	Expression	Description
$omegalight$	$((2 * pi * c_const)/wl)$	frequency of light
e_{ag}	$1 - ((f1 * omegap\text{^}2) * (omegalight\text{^}2 + i * g1 * omegalight)\text{^}(-1)) + (f2 * omegap\text{^}2) * (((omega2\text{^}2) - omegalight\text{^}2) - i * g2 * omegalight)\text{^}(-1) + (f3 * omegap\text{^}2) * (((omega3\text{^}2) - omegalight\text{^}2) - i * g3 * omegalight)\text{^}(-1) + (f4 * omegap\text{^}2) * (((omega4\text{^}2) - omegalight\text{^}2) - i * g4 * omegalight)\text{^}(-1) + (f5 * omegap\text{^}2) * (((omega5\text{^}2) - omegalight\text{^}2) - i * g5 * omegalight)\text{^}(-1) + (f6 * omegap\text{^}2) * (((omega6\text{^}2) - omegalight\text{^}2) - i * g6 * omegalight)\text{^}(-1)$	Drude-Lorentz model for silver
$e1$	$real(e_ag)$	Silver dielectric constant (real part)
$e2$	$imag(e_ag)$	Silver dielectric constant (imaginary part)
n_{ag}	$sqrt((e1/2) + 0.5 * sqrt(e1\text{^}2 + e2\text{^}2))$	Silver refractive index (real part)
k_{ag}	$e2/(2 * n_ag)$	Silver refractive index (imaginary part)
n_{clad}	$sqrt(1 + (a1_clad * wl\text{^}2)/(wl\text{^}2 - b1_clad\text{^}2) + (a2_clad * wl\text{^}2)/(wl\text{^}2 - b2_clad\text{^}2) + (a3_clad * wl\text{^}2)/(wl\text{^}2 - b3_clad\text{^}2))$	Sellmeier equation for cladding refractive index

Appendix B

